Universitetet
i Stavanger

FACULTY OF SCIENCE AND TECHNOLOGY

MASTER'S THESIS

Study program/specialization: Petroleum Engineering - Master of Science Degree Program/Reservoir Technology	Spring semester, 2019 Open
Author: Anna Maija Nørstebø Flaata	………………………………………… (signature of author)

Program coordinator: Professor Ingebret Fjelde

Supervisor(s): Professor Ingebret Fjelde

Title of master's thesis:

The Impact of Permeability on Density-Driven Convection During CO_2 Storage in Underground Reservoirs

Credits: 30

Keywords: Density-driven convection Hele-Shaw cell Porous Media Permeability Heterogeneity	Number of pages: 90 + supplemental material/other: 0 Stavanger, 14.06.2019 date/year

Title page for Master's Thesis
Faculty of Science and Technology

Abstract

Within the context of global warming, CO_2 storage in geological reservoirs is seen as one of many strategies to reduce greenhouse gas emissions over the next few decades. In CO_2 storage, the water density increases upon dissolution of CO_2, leading to a density-driven convective flow regime, which accelerates the CO_2 dissolution beyond that of molecular diffusion only. The aim of this thesis has been to visualize CO_2 dissolution in water-saturated, water-wet porous media on an experimental scale, by varying the permeability conditions. This is to improve the understanding of the permeability impact on the CO_2 dissolution on a reservoir scale.

This M.Sc. thesis is twofold; The literature part outlines how CO_2 can be stored in reservoirs and the work that has previously been carried out on CO_2 dissolution in the water phase in a reservoir, focusing on density-driven convection upon CO_2 dissolution in water. The experimental part presents a set of Hele-Shaw experiments, conducted at 10 bars pressure and room temperature, in which CO_2 dissolves in the water phase. The pH indicator method was used to visualize CO_2 dissolution and a camera was used for documentation. Images and time-series data of finger lengths are presented. The experiments were repeated with various permeabilities to vary the characteristic Rayleigh number and variations in homogeneous and heterogeneous permeabilities.

Density-driven convection occurred in homogeneous permeability experiments with bulk water and high-permeable porous media. Experiments with homogeneous low-permeable porous media were, however, dominated by pure diffusion. In heterogeneous permeability experiments, a horizontal low-permeable layer in between high-permeable layers attenuated the density-driven convection, while density-driven convection occurred in a vertical high-permeable layer rather than in the low-permeable layers surrounding it.

As a continuation of the experimental work performed in the present study, I will suggest performing experiments with porous media of heterogeneous permeability; To vary the location, thickness and inclination of the different layers, to perform experiments at more realistic reservoir temperature and pressure conditions, and to perform experiments in oil-saturated porous media for increased relevance to storage in hydrocarbon reservoirs.

Acknowledgment

The thesis "The Impact of Permeability on Density-Driven Convection During CO_2 Storage in Underground Reservoirs" was written during the spring semester 2019, in connection with the graduation from an M.Sc. degree within Petroleum Engineering, with reservoir technology as a specialist field.

I wish to thank the University Centre in Svalbard (UNIS), at which I attended a summer course in 2018 and was introduced to carbon dioxide capture and storage. Furthermore, I would like to thank the University in Stavanger (UiS) and the Norwegian Research Centre (NORCE) for allowing me to write my M.Sc. thesis on this relevant topic. An extra thank you must, of course, be directed to the UiS for five exciting years as a student.

I would like to express my sincere gratefulness to my supervisor, Professor Ingebret Fjelde, for his very valuable help and guidance through the work on this thesis. Widuramina Amarasinghe also deserves a big thank you for outstanding laboratory help. A thank you must also be directed to the rest of the staff at NORCE, for having welcomed me and helped me during my stay.

Furthermore, I want to thank my boyfriend for his invaluable mental support and ability to brighten up everyday life. My family has, as usual, been outstanding. You all know what you mean to me. I wish to thank my friends for all good conversations over a cup of coffee while sharing writing tips and tricks with each other.

Table of Contents

List of Figures

List of Graphs

List of Tables

Abbreviations

2D	Two Dimensional
3D	Three Dimensional
µm	Micrometer
BG	Bromocresol Green
BP	Bromocresol Purple
BTB	Bromothymol Blue
CCS	Carbon dioxide Capture and Storage
CO_2	Carbon dioxide
CO_3^{2-}	Carbonate ion
D	Darcy
EOR	Enhanced Oil Recovery
g	Gram
GHG	Greenhouse Gas
H^+	Hydrogen ion
H_2CO_3	Carbonic acid
HC	Hydrocarbon
HCO_3^-	Bicarbonate ion
M	Molar
mD	Millidarcy
mL	Millilitre
n. d.	No date
NaOH	Sodium hydroxide
N_2	Nitrogen
P&ID	Piping and Instrumentation Diagram
PMMA	Polymethyl Methacrylate
POM	Polyoxymethylene
PSD	Particle Size Distribution
PVT	Pressure, Volume, and Temperature
wt%	Weight Percent

Nomenclature

β	Coefficient of density increase of water with respect to CO_2 concentration
γ	Permeability anisotropy ratio
ϕ_a	Absolute porosity
ϕ_e	Effective porosity
$\Delta\rho$	Density difference between CO_2-saturated and unsaturated water
ρ_0	Density of the unsaturated water with respect to CO_2
ρ_f	Local, time-dependent denity of CO_2-saturated water
μ	Constant water viscosity
b	Spacing between the sight discs in a Hele-Shaw cell
C_0	Initial equilibrium CO_2 concentration in the water near the CO_2-water interface
c_1	Numerical constant
C	Local, time-dependent CO_2 concentration in water
D	Effective diffusion coefficient of CO_2 into water
g	Gravity acceleration
H	Thickness of porous medium
k	Absolute permeability
k_{eff}	Effective permeability
k_h	Horizontal permeability
k_v	Vertical permeability
P	Pressure
Ra	Rayleigh number
Ra_c	Critical Rayleigh number
t_c	Critical time for onset of convection
u	Darcy velocity
V_b	Bulk rock volume
$V_{p,i}$	Interconnected pore volume
$V_{p,t}$	Total pore volume
z	Vertical coordinate

1 Introduction

1.1 Background

Ever since the industrial revolution initiated, the world's energy demand has increased (Singh, 2013). Today, most industries depend upon the exploitation of fossil fuels to meet their energy demand. Fossil fuels like coal, oil and natural gas are all hydrocarbons (HCs). Combustion of such fuels causes emission of greenhouse gases (GHGs), among them carbon dioxide (CO_2), to the atmosphere. The excessive GHG emissions cause a rise in Earth's temperatures. This process is known as global warming and may have a highly injurious impact on life on Earth.

Many researchers agree that global warming is most likely caused by an increase in man-made GHG emissions (Metz, 2005). To alleviate global warming, there is broad consensus that a significant reduction in atmospheric GHG concentrations must occur. This can be achieved by drastically reducing GHG emissions over the next few decades (van Bergen, Gale, Damen & Wildenborg, 2004). Such reductions can probably only be achieved with a broad strategy, encompassing: (1) a reduction of World's energy demand due to energy-efficient enhancements, (2) a transition to less carbon concentrated fuels, (3) an increase in the use of nuclear power and renewable energy sources, (4) an increase in the amount of biological carbon sinks and (5) a reduction of emission of other GHGs than CO_2 (Metz., 2005).

The strategy should also encompass "cleaner" use of existing fossil fuel reserves (Ennis-King & Paterson, 2005; Singh, 2013). A possible solution to the latter alternative is the utilization of CO_2 capture and storage (CCS). According to Metz (2005), "CCS is a process consisting of the separation of CO_2 from industrial and energy-related sources, transport to a storage location and long-term isolation from the atmosphere." Hence, CCS allows utilization of fossil fuels, without large CO_2 emissions to the atmosphere. The complete CCS process thus includes three subprocesses: Capture, transport, and storage of CO_2 (Singh, 2013). Capture and transport will not be covered by the scope of this thesis, while CO_2 storage will. A basic mechanism that enables storage will be particularly emphasized.

As evaluations of CCS initiated in the early 1990s (Leonenko & Keith, 2008), it was suggested to implement geological CO_2 storage by injection into HC reservoirs, deep saline aquifers, unmineable coal beds (Hassanzadeh, Pooladi-Darvish & Keith, 2006, 2009; Mojtaba, Behzad, Rasoul & Mohammad, 2014; van Bergen et al., 2004; Yang & Gu, 2006) and basalt formations (Metz, 2005; Singh, 2013). These options can be subdivided into storage without and with energy benefits (Singh, 2013; van Bergen et al., 2004); Storage in basalt formations and deep saline aquifers belong to the former group, while storage in unmineable coal seams and HC reservoirs belong to the latter. Thus, notwithstanding that deep aquifers are believed to have the largest storage capacity and be much more widespread than the other options (Metz, 2005) HC reservoirs have attracted much attention (Leonenko & Keith, 2008).

Ennis-King & Paterson (2005) claims that enhanced oil recovery (EOR) projects, in which CO_2 is injected both to increase the recovery and to provide storage, are the most economically attractive forms of underground storage in the short term. As a matter of fact, CO_2-EOR has already been used by the petroleum industry for decades due to its cost-effectiveness (van Bergen et al., 2004). Moreover, HC reservoirs are considered more secure with respect to CO_2 storage than deep aquifers (Leonenko & Keith, 2008); One reason for this is that financial interests cause HC reservoirs to be far more surveyed than deep aquifers. Another reason is that the cap rocks of HC reservoirs have proven to retain buoyant fluids for geological timescales. Moreover, if significant infrastructures are already in place, the total costs of CCS can be reduced (Metz, 2005). Thus, this thesis will mainly focus on CO_2 storage in reservoirs. Understanding the role of CO_2 dissolution in formation water, which affects the performance of CO_2 storage, is extremely important and will be highlighted, which further leads to the aim and objectives of this thesis:

1.2 Aim and Objectives

The aim of the present study is to visualize CO_2 dissolution in water-saturated, water-wet porous media on an experimental scale by varying the permeability conditions. This is to improve the understanding of the impact of permeability on the CO_2 dissolution process on reservoir scale. The objectives for the above aim are:

1) To conduct a literature study that will provide a theoretical background for the understanding of the experimental part of the thesis
2) To perform CO_2 dissolution experiments in a Hele-Shaw cell of homogeneous permeability conditions, using the pH indicator method. These experiments include:
    a) To visualize CO_2 dissolution in bulk water (In absence of porous medium)

    b) To visually investigate the effect of permeability on CO_2 dissolution in water-saturated, water-wet porous media

3) To perform CO2 dissolution experiments in a Hele-Shaw cell of heterogeneous permeability conditions, using the pH indicator method. These experiments include:
    a) To visually investigate the effect of horizontally alternating permeability on CO_2 dissolution in water-saturated, water-wet porous media
    b) To visually investigate the effects of vertically alternating permeability on CO_2 dissolution in water-saturated, water-wet porous media
4) To interpret and compare the results of points 2 and 3 with previous work performed on CO_2 dissolution (Both stability analyses, simulations, and experiments)

1.3 Structure of the Thesis

The thesis is organised as follows: First, a literature study is presented in Section 2, which summarises how CO_2 can be stored in reservoirs and the work that has previously been performed on CO_2 dissolution in the water phase of a reservoir. Following the literature study, Section 3 gives a description of the experimental setup and the protocol followed to perform the experiments. Section 4 presents the experimental results. These are compared with existing knowledge and previous work on CO_2 dissolution in water in the discussion in Section 5. Finally, the conclusions are given in Section 6.

2 Literature Study

2.1 Storage of CO_2

Although CO_2-EOR projects have led the petroleum industry to focus on short-term processes occurring during the lifetime of a field, CO_2 storage projects should consider long-term containment of CO_2 in the underground (Ennis-King & Paterson, 2005). Naturally occurring underground accumulations of CO_2 is a widespread geological phenomenon and thus a good indicator of the possibility for long-term geological storage of CO_2 (Metz, 2005). Moreover, knowledge and experience achieved from various existing CO_2 storage projects, such as the Sleipner project offshore Norway, also strongly indicate that CO_2 storage in underground reservoirs is possible to implement.

According to Metz (2005), storage site selection is crucial for successful geological CO_2 storage. In fact, many of the same elements that make up a traditional HC system are needed for successful CO_2 storage in a reservoir (Bjørlykke, 2015); These elements along with their properties will be described in the following sections.

2.1.1 Trap

Like most HCs, CO_2 often has a lower density than water and therefore tends to migrate upwards in the direction of lower pressure (Bjørlykke, 2015; Metz, 2005). This migration continues until it escapes to the atmosphere unless it accumulates in a trap. A trap is, according to Metz (2005), a geological structure that physically retains buoyant fluids. Thus, traps must form structures that collect these fluids. Geologists often distinguish between structural and stratigraphic traps (Bjørlykke, 2015; Zolotukhin & Ursin, 2000). Structural deformation of rocks, such as folding, doming, or faulting forms structural traps, whereas stratigraphic traps are related to primary features in the sedimentary sequences. Traps consist of reservoir rocks, overlain by low-permeable cap rocks which do not allow buoyant fluids to pass.

2.1.2 Cap Rock

The reservoir should be overlain by extensive rock formations of low porosity and permeability, and structural simplicity, usually called a cap rock (Metz, 2005). According to Metz (2005), "a cap rock is a rock of very low permeability that acts as an upper seal to prevent fluid flow out of the reservoir". Examples of cap rocks can be claystone and shale, which have very low permeabilities and can be almost completely impermeable (Bjørlykke, 2015). Shale permeabilities as low as $1 \cdot 10^{-11}$ Darcy have been measured in laboratories. At the beginning of site selection evaluations, geology characterization is performed to determine whether the overlaying flow barrier acts as an effective seal (Metz, 2005).

2.1.3 Reservoir

According to Bjørlykke (2015), a reservoir rock can be any rock with sufficiently high porosity and permeability, provided that it is part of a trap with a low-permeable flow barrier at top, so that buoyant fluids accumulate in it, rather than migrating through it. Reservoirs are made up of sedimentary rocks (Zolotukhin & Ursin, 2000). Thick units of sedimentary rocks can result from deposition of sedimentary particles into basin-like structures, called sedimentary basins (Fossen, 2008). These can be found both onshore and offshore and can be more than 200 meters thick and extend laterally over several kilometres (Emami-Meybodi, Hassanzadeh, Green & Ennis-King, 2015; Metz, 2005). Clastic and biochemical are the two main types of sedimentary rocks (Fossen, 2008): Clastic sedimentary rocks are dominated by silica minerals and are composed of mineral grains and rock fragments from older rocks (Zolotukhin & Ursin, 2000). Biochemical sedimentary rocks are dominated by carbonate minerals and are composed of shell or skeletal residue from organisms or are directly precipitated from water (Fossen, 2008). Approximately 50 to 60 % of the worldwide reservoirs are sandstones, while carbonates account for almost 40 % (Bjørlykke, 2015).

In a reservoir, the most important properties are porosity and permeability, as the storage and fluid transport capacities, respectively, are determined by these (Bjørlykke, 2015; Zolotukhin & Ursin, 2000).

2.1.3.1 Porosity

Geological formations are composed of rock grains and fluids, which is mostly water (Bjørlykke, 2015; Fossen, 2008). In addition, fractures and cavities are filled with fluids (Fossen, 2008). The porosity is an expression of the volumetric fraction or percentage of fluids relative to the bulk rock (Bjørlykke, 2015). Porosity is thus dimensionless.

One distinguishes between two types of porosity (Zolotukhin & Ursin, 2000): Absolute and effective porosity, which differ by their ability to allow fluids accessing the pore space. The absolute porosity, ϕ_a, is defined as the ratio between the part of the bulk rock volume which is not occupied by rock grains, that is, the total pore volume, $V_{p,t}$, and the bulk rock volume, V_b:

$$\phi_a = \frac{V_{p,t}}{V_b}$$

The effective porosity, ϕ_e, is defined as the ratio between the volume of interconnected pores, $V_{p,i}$, and the bulk rock volume, V_b:

$$\phi_e = \frac{V_{p,i}}{V_b}$$

A reservoir rock should have a significant porosity to store fluids, usually 10 to 30 % (Fossen, 2008).

2.1.3.2 Permeability

Permeability is associated with the ability of a rock to transport fluids through a system of interconnected pores (Zolotukhin & Ursin, 2000). The unit for permeability is Darcy [D], or millidarcy [mD] (Fossen, 2008). The latter will be used throughout the present study. Permeability requires porosity but will also depend on the connection of the pores and the sizes of the pore throats. Moreover, thin cracks in the rock will contribute significantly to increased permeability (Bjørlykke, 2015).

One distinguishes between two types of permeability (Zolotukhin & Ursin, 2000): Absolute and effective permeability. When one single fluid phase is present and flows through permeable rock, the absolute permeability, k, is defined as the rock's ability to transport the fluid (Schlumberger Oilfield Glossary, n. d., a). When several fluid phases flow simultaneously through permeable rock, each fluid phase counteracts the flow of the other phases (Zolotukhin & Ursin, 2000). Thus, each phase will experience a reduced phase permeability relative to the absolute permeability, called effective permeability, k_{eff}.

Permeability values between 100 and 1000 mD are considered extremely good reservoir rocks (Bjørlykke, 2015). There are, however, examples of reservoir rocks with permeabilities of 10 000 to 40 000 mD, such as the Johan Sverdrup field offshore Norway (Jørstad, 2012). There are also examples of rocks with very low permeabilities, like the Ekofisk field, where the generally low permeability of the chalk matrix is improved due to fractures, which increase the overall permeability (Bjørlykke, 2015). However, reservoirs exhibit both directional and spatial variations in their medium properties, such as permeability (Xu, Chen & Zhang, 2006). These variations are referred to as permeability anisotropy and heterogeneity, respectively.

Permeability Anisotropy

Permeability is often considered a scalar in practice (Zolotukhin & Ursin, 2000). However, this is only valid for isotropic porous media, that is, porous media that possess equal permeabilities in all directions. In the great majority of rocks however, the permeability differs according to the flow direction (Bjørlykke, 2015). Permeability is, in fact, one of the most common anisotropic properties (Schlumberger Oilfield Glossary, n. d., b). A common feature of sedimentary reservoir rocks is much higher permeability parallel to the bedding than normal to bedding. In other words, that the horizontal permeability, k_h, is higher than the vertical permeability, k_v (Lindeberg & Wessel-Berg, 1997; Xu et al., 2006). According to Schlumberger Oilfield Glossary (n.d., c), this feature can be referred to as vertical to horizontal permeability anisotropy. Since the flow capacity will vary depending on the flow direction in an anisotropic geologic formation, it is more correct to consider permeability as a tensor (Zolotukhin & Ursin, 2000).

The extent of permeability anisotropy within a porous and permeable medium can be expressed by anisotropy ratio, γ, which is the ratio of vertical permeability to horizontal permeability (Ennis-King & Paterson, 2005):

$$\gamma = \frac{k_v}{k_h}$$

Permeability Heterogeneity

Most reservoirs are far from homogeneous (Bjørlykke, 2015). They exhibit a complex structure and significant variations in the sizes and the packing of the rock grains (Zolotukhin & Ursin, 2000). This results in spatial variations of important reservoir properties, such as porosity and permeability, which are often associated with the heterogeneity of porous media. Spatial variations in any reservoir property can affect flow efficiency, but spatial variations in permeability, which can vary by several orders of magnitude, appear to have a particularly great influence (Jensen & Lake, 1988). This is referred to as permeability heterogeneity.

2.2 Properties of CO_2

2.2.1 Physical Properties

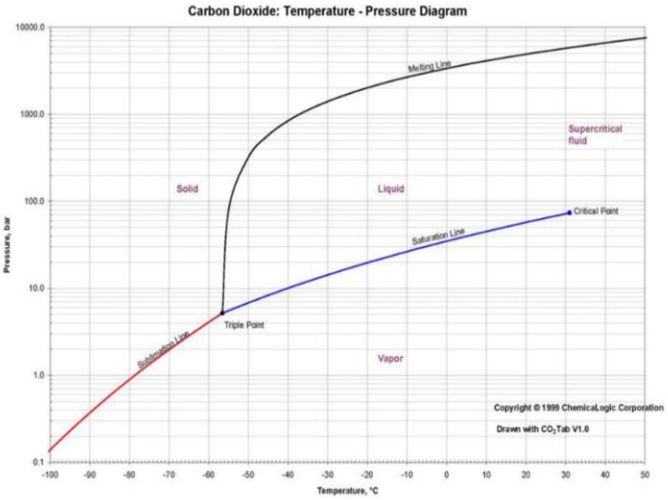

Figure 2.1: Phase diagram for CO_2, showing the different states of CO_2 for different pressure and temperature conditions (Johnsen et al., 2009).

The physical state of CO_2 varies with pressure and temperature, as shown in the phase diagram in Figure 2.1 (Johnsen, Holt, Helle, & Sollie, 2009). It can exist in its gas, liquid or solid phase and properties, such as density and viscosity, vary significantly between these phases. At normal conditions (T = 20 °C and P = 1 atm), CO_2 is gaseous, and its density is approximately 2.0 kg/m^3 (Emami-Meybodi et al., 2015). At such low temperatures, an increase in pressure can lead to a phase transition from gas to liquid, corresponding to a large density increase (Bjørlykke, 2015). CO_2 becomes supercritical at temperatures and pressures higher than approximately 31.1 °C and 73.8 bars. In the supercritical region, distinct liquid and gas phases do not exist, and an increase in pressure leads to a steady density increase (Johnsen et al., 2009). In the supercritical region, the CO_2 viscosity is like that of a gas, while the density is closer to that of a liquid (Metz, 2005).

Expected storage depths for CO_2 in reservoirs are usually between 800 m and 3 000 m (Emami-Meybodi et al., 2015). The pressure and temperature conditions associated with these storage depths will normally result in CO_2 occurring in its liquid phase or as a supercritical fluid. The physical fluid properties of both CO_2 and water, such as density and viscosity, are depending on temperatures, pressures, and salinity (Emami-Meybodi et al., 2015). Water is nearly incompressible and has a quite narrow density range, roughly between 945 and 1 230 kg/m^3, even at reservoir conditions. As opposed to water, CO_2 is compressible. At target depths, it will have a liquid-like density ranging between approximately 266 and 800 kg/m^3. However, at very high pressures CO_2 can be very dense, either approaching or exceeding the water density (Metz, 2005). The CO_2 density range is close to the density range of some crude oils at reservoir conditions and higher than for natural gas (Metz, 2005).

2.2.2 Chemical Properties

CO_2 can dissolve in water both from its gaseous and supercritical state, as expressed by equilibrium (1) below (Hassanzadeh et al., 2009; Thomas, Lemaigre, Zalts, D'Onofrio & De Wit., 2015). Upon dissolution of CO_2 in the water, CO_2 and water react chemically to form carbonic acid, H_2CO_3, until a new equilibrium (2) is reached (Mojtaba et al., 2014; Thomas et al., 2015). H_2CO_3 is a weak acid which, in accordance to equilibrium (3) and (4) dissociates instantaneously into bicarbonate, HCO_3^-, and carbonate, CO_3^{2-}, ions (Thomas et al., 2015). The release of hydrogen ions, H^+, expressed by equilibria (3) and (4) below, lowers the pH of the water. The pH decrease can be of several pH units, and pH drops to three or even lower can occur (Bjørlykke, 2015).

$$CO_2\ (g) \leftrightarrow CO_2\ (aq) \qquad (1)$$

$$CO_2\ (aq) + H_2O \leftrightarrow H_2CO_3\ (aq) \qquad (2)$$

$$H_2CO_3\ (aq) \leftrightarrow H^+\ (aq) + HCO_3^-\ (aq) \qquad (3)$$

$$HCO_3^-\ (aq) \leftrightarrow H^+\ (aq) + CO_3^{2-}\ (aq) \qquad (4)$$

2.3 Sleipner Project – The First CO_2 Storage Project for Climate Reasons

Research on the area of CO_2 dissolution in water is to successfully implement CO_2 storage in underground formations, such as reservoirs. However, several CO_2 storage projects are already up and running (Metz, 2005). One such project is the Sleipner project in the North Sea offshore Norway.

The Sleipner field consists of gas and condensate reservoirs located approximately 3 500 m below the seabed (Kongsjorden, Kårstad & Torp, 1998). The natural gas produced from parts of the reservoirs contains 9 to 9.5 % CO_2, whereas the maximum allowed content of CO_2 in gas for sale is 2.5% (Bjørlykke, 2015; Kongsjorden et al., 1998). Therefore, most of the CO_2 is removed from the natural gas stream during production (Bjørlykke, 2015). Previous practice was to release the extracted CO_2 to the atmosphere, but in 1991 Norway started taxing CO_2 emissions (Bjørlykke, 2015; Kongsjorden et al., 1998). Therefore, it was decided to inject the extracted CO_2 into the Utsira formation through a separate injection well. Injection commenced in 1996 and has continued successfully at a rate of approximately 1 million tonnes of CO_2 each year (Bjørlykke, 2015; Kongsjorden, 1998). This was the first time that storage of CO_2 for climate reasons took place (Kongsjorden, 1998).

The Sleipner project was feasible because the Utsira formation is located close to the Sleipner field and has good reservoir properties (Bjørlykke, 2015). It is made up of weakly compacted sandstone with a high porosity between 30 and 40 %. The reservoir is very extensive and forms an open system so that the CO_2 can easily migrate laterally below the cap rock, which consists of 250 m thick clay-rich sequences (Bjørlykke, 2015; Hassanzadeh et al., 2006). The Utsira formation is located approximately 1 000 m below the seabed (Kongsjorden et al., 1998). At 800 m below the seabed, the corresponding temperatures and pressures are approximately 37 ˚C and 100 bars, which causes CO_2 to be supercritical in the reservoir (Bjørlykke, 2015).

2.4 Trapping Mechanisms

Storage of CO_2 in a suitable reservoir is accomplished by injecting CO_2 into the storage zone (Metz, 2005). To avoid two-phase conditions in the injection well, this should be performed at supercritical CO_2 conditions (Garcia, 2001). The well is opened towards the reservoir by perforation or screening in the storage zone (Metz, 2005). When the well pressure is higher than the pore pressure, CO_2 migrates laterally away from the injector due to pressure gradients. Throughout this process, at least four different physical and geochemical mechanisms contribute to entrapment of CO_2 (Hassanzadeh et al., 2009; Kneafsey & Pruess, 2010, 2011; Metz, 2005; Newell, Carey, Backhaus & Lichtner, 2018). An overview of these processes is shown in Figure 2.2.

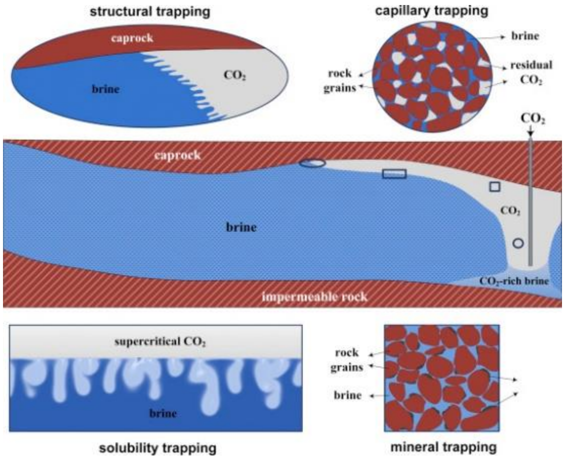

Figure 2.2: Overview of the main physical and geochemical CO_2 trapping mechanisms (Emami-Meybodi et al., 2015).

2.4.1 Physical Trapping Mechanisms

As mentioned in Section 2.2.1, supercritical CO_2 is usually less dense than formation water (Emami-Meybodi et al., 2015). Due to buoyancy caused by this density difference, upwards CO_2 migration occurs. In a reservoir suitable for storage, the CO_2 will eventually reach the cap rock. Consequently, a plume of CO_2 is physically trapped between the overlying seal and the underlying formation water. The plume will tend to spread out under the seal and at some distance away from the injection well there will be a nearly horizontal CO_2-water interface (Kneafsey & Pruess, 2010). Properties of the porous medium will affect the geometric details of the interface, but at this point in the explanation, it can be assumed relatively flat.

CO_2 contained inside a trap is still mobile and might leak off if the cap rock is not completely sealed (Emami-Meybodi et al. 2015). Leakage can take place through natural or artificial pathways, like fractures, faults and abandoned wells (Emami-Meybodi et al., 2015; Hassanzadeh et al., 2009). A reduction in the amount of mobile CO_2 corresponds to an increase in the long-term safety of CO_2 storage (Ennis-King & Paterson, 2005). Such a reduction can be achieved through various geochemical trapping mechanisms (Emami-Meybodi et al., 2015).

2.4.2 Geochemical Trapping Mechanisms

During the injection phase of a geological storage project, mobile CO_2 migrates through the reservoir. CO_2 is typically the non-wetting phase, as opposed to the in-situ formation water (Hesse, Orr Jr. & Tchelepi, 2009). Drainage of the formation water from the smallest pores are prevented due to the capillary entry pressure. Thus, the displacement of formation water by CO_2 is incomplete. Some of the CO_2 dissolves in the residual formation water and is immobilized (Ennis-King & Paterson, 2005). This amount depends on the relative permeability curves and the residual water saturation. As the CO_2 migrates further into the reservoir, formation water re-imbibes the pore system (Hesse et al., 2009). However, a small fraction of the CO_2 is left behind as residual droplets within the pores, immobilized by capillary forces and thus trapped within the pore system. This process is called capillary trapping or residual phase trapping.

Another geochemical trapping mechanism that can contribute to the immobilization of CO_2 is a process referred to as solubility trapping (Ennis-King & Paterson, 2005). According to Metz (2005), solubility trapping is “a process in which fluids are retained by dissolution in liquids naturally present”. As mentioned in Section 2.2.2, CO_2 can dissolve in formation water both in its gaseous and supercritical state (Hassanzadeh et al., 2009), but the dissolution increases with increasing pressure (Yang & Gu, 2006). Thus, at a constant temperature, supercritical CO_2 possesses better solvent properties than gaseous CO_2. Dissolution of CO_2 in the formation water occurs from the injection phase through the post-injection phase (Emami-Meybodi et al., 2015). An important sub-process to the solubility trapping process, called density-driven convection, is the process of interest in this thesis. A detailed explanation is entirely devoted to Section 2.5.

As stated in Section 2.2.2, dissolution of CO_2 in the formation water forms the weak acid H_2CO_3 which further dissociates into HCO_3^-- and CO_3^{2-} ions and lower the pH of the formation water (Thomas et al., 2015). Changed ionic composition and lowered pH of the formation water can cause chemical reactions to alter the reservoir mineralogy of the host minerals over time (Emami-Meybodi et al., 2015). In favourable mineralogy, such as calcium- and magnesium containing formations, HCO_3^-- and CO_3^{2-} ions can react to form solid minerals (Ennis-King & Paterson, 2005). This process is known as mineral trapping and can occur over relatively short geological time scales. Mineral trapping is believed to be less pronounced in pure sandstones, as precipitation of a significant amount of CO_2 can take hundreds to thousands of years.

Initially, most of the injected CO_2 will be mobile (Kneafsey & Pruess, 2010). Thus, physical trapping dominates in the early stages. Over time, the geochemical storage mechanisms become increasingly important, as shown in Figure 2.3. The storage security increases along this pathway from physical trapping to mineral trapping (Kneafsey & Pruess, 2011).

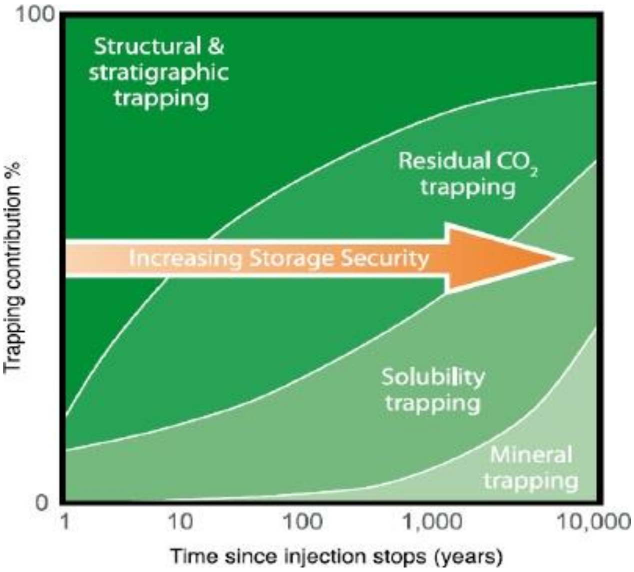

Figure 2.3: Illustration of when the different mechanisms contribute to trapping of CO_2. The figure also illustrates that the storage security generally increases with time (Metz, 2005).

2.5 The Process of CO_2 Dissolution in Liquids

2.5.1 CO_2-Water System

Most papers theoretically describing solubility trapping of CO_2, seem relatively unanimous in how CO_2 dissolves in formation water (Emami-Meybodi et al., 2015; Ennis-King & Paterson, 2005; Farajzadeh, Barati, Delil, Bruining & Zitha, 2007; Hassanzadeh et al., 2006; Lindeberg & Wessel-Berg, 1997); When a CO_2 plume settles above the formation water after the upwards migration described in Section 2.4.1, CO_2 starts dissolving in the underlying formation water by molecular diffusion (Hassanzadeh et al., 2006). The result is CO_2-saturation of a thin layer in the top of the formation water (Lindeberg & Wessel-Berg, 1997). In contrast to most other gases, an unusual feature of CO_2 is that the water density increases linearly with the concentration of dissolved CO_2 (Ennis-King & Paterson, 2005; Yang & Gu, 2006). Garcia (2001) reported a density increase in on the order of 0.1 to 1% relative to pure water, depending on pressure, temperature, and salinity of the water.

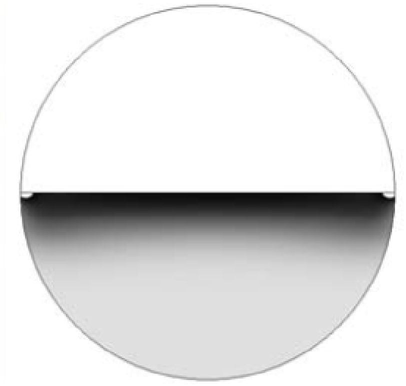

Figure 2.4: *Density gradient profile. The darker colours denote higher density. The figure is modified from Khosrokhavar et al., (2011).*

Consequently, a vertical density gradient grows in the top of the formation water column (Lindeberg & Wessel-Berg, 1997). Its density is highest in the top of the CO_2-saturated water layer and gradually decreases downwards, as shown in Figure 2.4 (Khosrokhavar, Elsinga, Mojaddam, Farajzadeh & Bruining, 2011). When the diffusion layer becomes sufficiently thick, a gravitational instability evolves (Emami-Meybodi et al., 2015). Eventually, the combination of gravitational instability and perturbations within the system can initiate a process referred to as density-driven convection (Hassanzadeh et al., 2006). In real porous media, such perturbations can originate from unsymmetrical plume development, and the presence of heterogeneities, that is, local variations in porosity and permeability (Emami-Meybodi et al., 2015; Lindeberg & Wessel-Berg, 2011).

During density-driven convection, fingers of dense CO_2-saturated formation water migrate vertically downwards (Pau, Bell, Pruess, Almgren, Lijewski & Zhang, 2010). Fingering is "a condition whereby the interface of two fluids bypasses sections of a reservoir as it moves along, creating an uneven, or fingered, profile" (Schlumberger, n. d., d). Consequently, less dense unsaturated formation water migrates upwards to the CO_2-water interface at the top of the formation water column, where it contacts the CO_2 plume and dissolves more CO_2, before migrating downwards again (Pau et al. 2010). Density-driven convection appears as cellular motion, and an ideal case illustration is shown in Figure 2.5 (Lindeberg & Wessel-Berg, 1997).

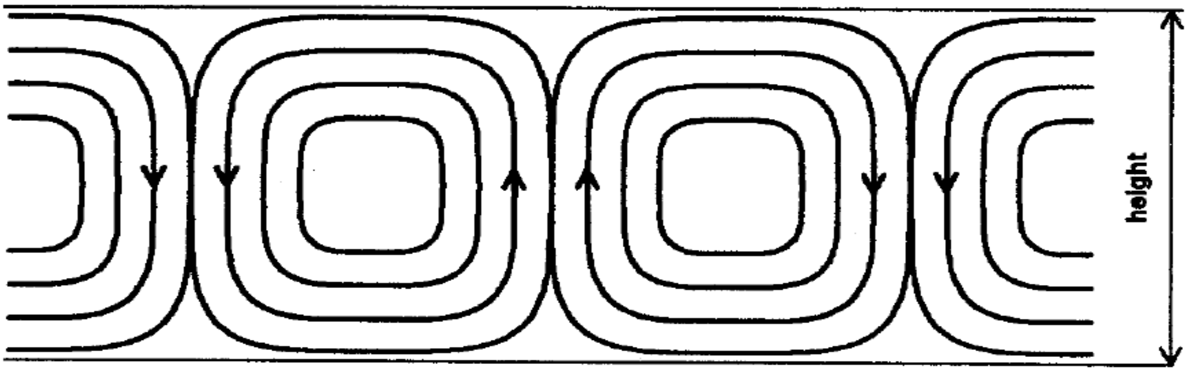

Figure 2.5: Ideal case illustration of the density-driven convection pattern. (Lindeberg & Wessel-Berg, 1997).

Among the first to mention the density-driven convection phenomenon for CO_2 dissolution in formation water was Weir, White & Kissling (1995, 1996) and Lindeberg & Wessel-Berg (1997). Lindeberg & Wessel-Berg (1997) stated that the onset of density-driven convection is only conditional and will depend on several properties of the porous medium and the fluid. If density-driven convection does not occur, only the upper part of the water column will be contacted by CO_2 and the CO_2 dissolution will be limited to molecular diffusion. However, if density-driven convection occurs, water in the depth, which is unsaturated with respect to CO_2, will be transported up to the CO_2-water interface where it can be saturated with respect to CO_2. Thus, the process is of practical interest for CO_2 storage because it accelerates the CO_2 dissolution beyond what would occur with pure molecular diffusion and it is therefore believed to play a key role in significantly increasing the storage capacity of reservoirs (Ennis-King & Paterson, 2005; Faisal, Chevalier, Bernabe, Juanes & Sassi, 2015; Kneafsey & Pruess, 2010). Understanding the factors that drive density-driven convection in water is therefore of major importance for the evaluation of geological CO_2 storage sites (Hassanzadeh et al., 2006). When CO_2 is completely dissolved in the formation water, leakage of mobile CO_2 can be excluded from risk assessments, due to the very slow natural migration of formation water within the reservoir. Therefore, density-driven convection decreases the time scale over which CO_2 is mobile and leakage is possible.

2.5.2 CO_2-Oil System

The density-driven convection process is not exclusive to the CO_2-water system and may also occur in CO_2-oil systems (Emami-Meybodi et al., 2015); Farajzadeh et al. (2007) found the dissolution of CO_2 in oil (n-decane) to increase the oil density. This was followed by a density-driven convective flow regime, which enhanced the mass transfer of CO_2 into oil, beyond what would occur with pure molecular diffusion. Similar results were obtained by Khosrokhavar et al. (2011, 2014), who found the density-driven convection currents to be stronger in oil (n-decane) than in pure water. Therefore, CO_2 dissolution by density-driven convection is believed to play an important role in CO_2-EOR, as it can increase the miscibility between CO_2 and oil and consequently accelerate the oil production (Farajzadeh et al., 2007; Khosrokhavar et al., 2011). The time required for the initiation of the density-driven convection plays a crucial role in the success of the CO_2-EOR project (Khosrokhavar et al., 2011). Therefore, understanding the interactions within the CO_2-oil system is of great interest to the petroleum industry.

2.6 Previous Work on CO_2 Dissolution in Water

The main questions that should be answered about CO_2 dissolution in water concern the time evolution of the process (Emami-Meybodi et al., 2015); What factors mainly affect the critical time for onset of convection? What factors influence the dissolution rate? What factors influence the time for a complete dissolution of the injected CO_2? Previous work on CO_2 dissolution in water that has attempted to answer these questions include stability analyses, simulations and laboratory work. Each of these has its own strengths and drawbacks and thus a combination of these is probably necessary in order to understand the CO_2 dissolution process in its entirety.

2.6.1 Linear Stability Analyses

CO_2 dissolution in a water-saturated porous medium has been the objective for several linear stability analyses (Ennis-King & Paterson, 2005; Hassanzadeh et al., 2006; Lindeberg & Wessel-Berg, 1997; Xu et al., 2006). Most of these studies have investigated the dissolution process by considering a two dimensional (2D) horizontal layer of an idealized medium, with porous, permeable, and homogeneous properties, saturated with initially stagnant formation water (Hassanzadeh et al., 2006). The lateral extensiveness is usually infinite or limited by impermeable boundaries (Emami-Meybodi et al., 2015; Lindeberg & Wessel-Berg, 1997). The vertical extensiveness, H, is delimited by an impermeable boundary at the bottom (Ennis-King & Paterson, 2005; Hassanzadeh et al., 2006). Even though real CO_2-water systems concern two-phase flow, the focus of stability analyses has mainly been on single-phase flow (Emami-Meybodi et al., 2015). Therefore, to simplify the problem as one of single-phase flow, instead of introducing a two-phase flow problem by treating the gas and liquid phases separately, the CO_2-water interface at the top is expressed as a boundary of constant CO_2 concentration, C_0 (Ennis-King & Paterson, 2005; Hassanzadeh et al., 2006).

2.6.1.1 Governing Equations

To study the stability condition of a CO_2-water system, the basic equations describing flow and fluid properties must be analysed (Lindeberg & Wessel-Berg, 1997). These are Darcy's law for single-phase fluid flow and the convective diffusion equation for the transport of dissolved CO_2 (Ennis-King & Paterson, 2005). In the aforementioned order, these can be presented as follows:

$$u = -\frac{k}{\mu}(\nabla P - \rho_f g \nabla z)$$

$$\phi \frac{\partial C}{\partial t} + u \cdot \nabla C = \phi D \partial^2 C$$

Here, u is the Darcy velocity (Xu et al., 2006). The fluid is assumed incompressible, meaning that $\nabla \cdot u = 0$. k is the absolute permeability tensor and ϕ is the porosity of the medium. In stability analyses, these are assumed spatially constant, but k is not necessarily isotropic. ρ_f is the local, time-dependent density of the CO_2-saturated water, which is approximated as linear, and μ is the constant water viscosity (Hassanzadeh et al., 2006; Xu et al., 2006). P is the pressure. g is the gravity acceleration and z the vertical coordinate, which is positive in the downwards direction. D is the effective diffusivity of CO_2 into the water, and C is the local, time-dependent concentration of dissolved CO_2 in the water-saturated porous medium (Ennis-King & Paterson, 2005; Hassanzadeh et al., 2006). t is time.

The link between the two equations above comes from the following effect of CO_2 dissolution on the saturated water density (Ennis-King & Paterson, 2005):

$$\rho_f = \rho_0(1 + \beta C)$$

Here, ρ_0 is the density of the CO_2-unsaturated water and β is the coefficient of density increase of the CO_2-saturated water with respect to CO_2 concentration (Hassanzadeh et al., 2006).

Rayleigh Number

The dimensionless Rayleigh number, Ra, for a porous medium gives the stability of such a system as described at the beginning of Section 2.6.1 (Hassanzadeh et al., 2006). It is mentioned in a vast number of papers (Emami-Meybodi et al., 2015; Ennis-King & Paterson, 2005; Hassanzadeh et al., 2006; Kneafsey & Pruess, 2010, 2011; Khosrokhavar et al., 2014; Lindeberg & Wessel-Berg, 1997; Mojtaba et al., 2014; Xu et al., 2006). The Rayleigh number provides an indication of whether density-driven convection will take place under given properties and conditions (Kneafsey & Pruess, 2010). Low Rayleigh numbers correspond to pure molecular diffusion because perturbations within the system are observed to decay. When the Rayleigh number exceeds a critical value, $Ra_c = 4\pi^2$, perturbations are observed to grow, and density-driven convection occurs (Hassanzadeh et al., 2006; Kneafsey & Pruess, 2011; Khosrokhavar et al., 2014; Lindeberg & Wessel-Berg, 1997; Xu et al., 2006).

Moreover, the effect of density-driven convection increases with increasing Rayleigh number (Farajzadeh, Ranganathan, Zitha & Bruining, 2011). Rayleigh number depends on properties of the fluid and the porous medium:

$$Ra = \frac{kC_0\beta\rho_0 gH}{\phi\mu D}$$

Here, H is the thickness of the porous medium (Ennis-King & Paterson, 2005; Hassanzadeh et al., 2006; Khosrokhavar et al., 2014; Xu et al., 2006). C_0 is the initial equilibrium concentration of CO_2 in the water at the CO_2-water interface (boundary condition). The constant C_0 is determined by the CO_2 solubility in formation water.

Critical Time

Whereas the Rayleigh number serves as a criterion for under what conditions and properties density-driven convection will occur, it does not express at what time density-driven convection initiates. Therefore, the onset time is another important parameter (Ennis-King & Paterson, 2005).

The linear stability analyses are based on the amplification of infinitesimal perturbations to the reference state of the system (Ennis-King & Paterson, 2005; Lindeberg & Wessel-Berg, 1997; Xu et al., 2006). The approximated linearized equations for the system are used to find the state where these infinitesimal perturbations just start to grow. This method produces the critical time, t_c, at which the density-driven convection initiates:

$$t_c = c_1 (\frac{\phi\mu\sqrt{D}}{k\Delta\rho g})^2$$

The new variables are c_1 which is a numerical constant and $\Delta\rho = C_0\,\beta\,\rho_0$, which is the density difference between CO_2-saturated and unsaturated water.

Linear stability analyses have at least one serious shortcoming (Ennis-King & Paterson, 2005; Xu et al., 2006): Since the linear stability analyses depend on linearization of the governing equations, the perturbation is always proportional to the perturbation in the initial conditions. This leads to an imprecise definition of the critical time for onset to initiate.

2.6.1.2 Analytical Results

Hassanzadeh et al. (2006) performed a linear stability analysis for homogeneous, isotropic porous media, in which the Rayleigh numbers for 24 CO_2 injection sites were calculated. 14 out of 24 calculated Rayleigh numbers were greater than Ra_c indicating that density-driven convection was likely to occur in 14 of the injection sites. For the calculated Rayleigh numbers, they found the lower critical time boundary for the onset of convection to vary from less than a year to an upper boundary of approximately 40 years. Hassanzadeh et al. (2006) also found that, at large Rayleigh numbers, the critical time for the onset of convection to be independent of the thickness of the porous medium.

Lindeberg & Wessel-Berg (1997) calculated Rayleigh numbers for four high-permeable reservoirs at typical Norwegian continental shelf conditions, assuming homogeneous porous media. They found the Rayleigh numbers to be two to three orders of magnitude larger than Ra_c, indicating that density-driven convection typically occurs in high-permeable aquifers. They also pointed out that they expected the presence of horizontal low-permeability layers to further decrease the possibility of density-driven convection.

As most stability analyses had studied the critical time for the onset of convection in isotropic permeability cases, Ennis-King & Paterson (2005) performed a stability analysis concerning anisotropic permeability. The anisotropy effect can be included in the Rayleigh number by letting the absolute permeability represent the characteristic permeability, that is, either the horizontal or the vertical permeability (Emami-Meybodi et al., 2015). By restricting the horizontal permeability and allowing the vertical permeability to vary, Ennis-King & Paterson (2005) suggested that an increase in the anisotropy ratio (corresponding to an increase in vertical permeability and/or a decrease in horizontal permeability) corresponds to a decrease in the critical time for instability to begin. Thus, an increase in the anisotropy ratio might destabilize the system and initiate density-driven convection. Furthermore, Ennis-King & Paterson (2005) indicated the likely range for critical times for instability to begin to be from less than a year up to several hundred years, depending on the permeability.

Relatively similar results were obtained by Xu et al. (2006), but they found the stability of the system to depend on the vertical and horizontal permeability, not only on the anisotropy ratio. In other words, Xu et al. (2006) suggested that an increase in either the vertical or the horizontal permeability corresponds to a decrease in the critical time for instability to begin. However, they concluded that an increase in vertical permeability has a stronger impact on CO_2 dissolution than a corresponding increase in the horizontal permeability.

2.6.2 Simulations

Most stability analyses concerning CO_2 dissolution in water assume homogeneous porous media and thus form the basis for understanding the CO_2 dissolution in terms of density-driven convection (Lin, Ni, Lee & Li, 2016). Although permeability anisotropy has been successfully implemented in stability analyses, implementation of permeability heterogeneity is beyond their capability (Ennis-King & Paterson, 2005; Xu et al., 2006). Heterogeneity is expected to play an important role in controlling the time of onset of instability and the subsequent density-driven convection because system heterogeneity leads to a varying concentration distribution (Xu et al., 2006). Therefore, simulations are of practical importance yielding density-driven convection, especially concerning heterogeneity.

In general, the physical model used for simulations is like that presented at the beginning of Section 2.6.1. There are, however, some differences between stability analyses and simulations; As opposed to stability analyses, the CO_2 dissolution process can be simulated using three dimensional (3D) models of a medium (Pau et al., 2010). However, fine-scale 3D models require a high number of grid blocks, which is associated to time consuming computational work (Pau et al., 2010) and most simulations are consequently performed using 2D models (Green, Ennis-King & Pruess, 2009; Farajzadeh et al., 2011; Lin et al., 2016; Lindeberg & Wessel-Berg, 2011). Like for stability analyses, a few simulation studies have used single-phase flow, by expressing the CO_2-water interface at the top as a boundary of constant CO_2 concentration (Farajzadeh et al., 2011; Pau et al., 2010). Most simulations are, however, performed using a multiphase flow code in which the gas and water phases are treated separately (Green et al., 2009; Lin et al., 2016; Lindeberg & Wessel-Berg, 2011).

In simulations, instability in the diffusive layer can be introduced in at least two ways; Either by numerical round-off errors in the computational work of the simulator (Lindeberg & Wessel-Berg, 2011), or as sinusoidal wavy perturbations to disturb the CO_2-water interface (Farajzadeh et al., 2011; Lin et al., 2016).

One drawback concerning simulations is that the predictions made on time scales relevant for CO_2 storage projects are obviously difficult to validate since only a small amount of the relevant period of time can be history matched (Ennis-King & Paterson, 2005).

2.6.2.1 Numerical Simulation Results

In their simulations, Green et al. (2009) compared an anisotropic homogeneous model with anisotropic heterogeneous models. The effective vertical permeability was 50 mD, whereas the effective horizontal permeability was 100 mD for all models. Two heterogeneous models were made from random distributions of horizontal impermeable barriers in an otherwise homogeneous porous medium. The onset of convection was observed earlier for the heterogeneous models, which were very similar, compared to the homogeneous model. Green et al. (2009) explained this by a larger average vertical distance between the horizontal impermeable barriers than the length scale at which fingers develop, leaving the fingers to experience a higher effective vertical permeability locally than globally. In the homogeneous model, the effective vertical permeability was constant at all scales, and thus lower than the local effective vertical permeability in between the impermeable horizontal layers in the heterogeneous models. At later times, however, when the fingers were longer than the average vertical distance between the horizontal impermeable barriers, the rate of CO_2 dissolution was similar for the heterogeneous and the homogeneous models. This indicated that the convection depends on the global effective vertical permeability, rather than the local effective vertical permeability at late times.

Farajzadeh et al. (2011) performed simulations in porous media of homogeneous and various degree of heterogeneous character. Heterogeneity was introduced by a random permeability distribution, keeping the effective permeabilities equal in vertical and horizontal directions constant. For the homogeneous cases, the onset time for density-driven convection was observed to decrease with increasing Rayleigh numbers, and the CO_2 dissolution rate was observed to increase with increasing Rayleigh number, in these cases caused by higher permeabilities. Similar results were found in simulations performed by Pau et al. (2010), who found the long-term behaviour of the CO_2 dissolution process to be dominated by convection and only depending on the mean value of the permeability. In the simulations performed by Farajzadeh et al. (2011), the dissolution rate was on average observed to be higher for the heterogeneous cases compared to the homogeneous ones. At a low degree of heterogeneity, the fingers were observed to develop independently of the permeability structure. At a moderate degree of heterogeneity, the fingers were seen to correlate strongly with the permeability distribution, that is, fingers developed faster in the high permeability regions.

Lindeberg & Wessel-Berg (2011) performed simulations in both homogeneous and heterogeneous models of porous media. Two different types of horizontal barrier geometries provided a reduction in the effective vertical permeability of an otherwise homogeneous isotropic model with background permeability of 1 800 mD; A regular barrier geometry provided a homogeneous anisotropic model with an effective vertical permeability of 365 mD. An irregular barrier geometry provided a heterogeneous model with an effective vertical permeability of 100 mD. The anisotrpic and heterogeneous models simulated by Lindeberg & Wessel-Berg (2011) can be seen in Figure 2.6. The predicted CO_2 dissolution rate was found to be higher for the heterogeneous model than for the homogeneous anisotropic model, in which the rate of density-driven convection was quite equal to the homogeneous isotropic model. In the heterogeneous model, the fingers were concluded to develop in the background porous medium, while they were impeded by the low vertical permeability in the homogeneous anisotropic model.

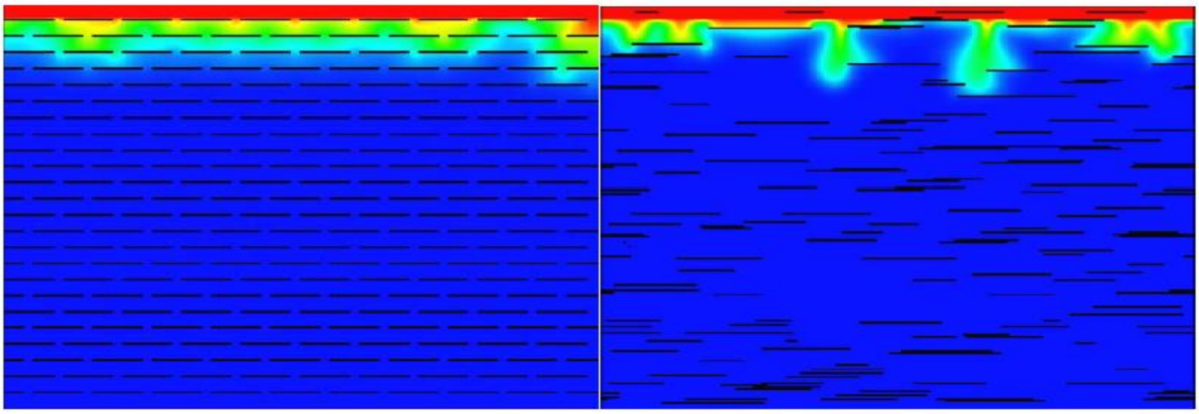

Figure 2.6: A regular barrier geometry provided a homogeneous anisotropic model (left) and an irregular barrier geometry provided a heterogeneous model (right) (Lindeberg & Wessel-Berg, 2011).

Lin et al. (2016) also performed simulations in homogeneous and heterogeneous porous media. Small scale heterogeneity was obtained by generating a random permeability field. It was found that relatively high local permeability values just below the CO_2-water interface triggered instabilities in the diffusive boundary layer and influenced the number of fingers developing initially. Also, an increased degree of heterogeneity caused increased CO_2 convection, compared to the homogeneous case, and the permeability below the fingers and along their paths were observed to substantially control their development. All simulation cases had a mean effective permeability of 3 000 mD, except for the cases where Lin et al. (2016) looked at the effect of mean effective permeability of 300 mD and 30 000 mD on density-driven convection. For these cases, the mean effective permeability was found to dominate the overall density-driven convection and be more significant in the long CO_2 convection term.

2.6.3 Experimental Work

As the dynamics of CO_2 dissolution in water is difficult to analyse in-situ actual reservoirs, it is important to perform experiments which on a small scale in the laboratory mimics the processes occurring on a large scale in reservoirs (Thomas et al., 2015). Previous experimental work on CO_2 dissolution in water includes quantitative experiments conducted in pressure, volume and temperature (PVT) cells, in addition to visualization experiments mainly conducted in transparent, quasi-2D (Hele-Shaw) cells, applying different methods for visualization.

2.6.3.1 Quantitative Experiments

In PVT cell experiments, CO_2 and water are brought in contact with each other in a closed, cylindrical PVT cell at a specified pressure and temperature (Farajzadeh et al., 2007). The mass transfer rate of CO_2 into the water can be determined quantitatively in at least two ways: One of them is to monitor the pressure of the CO_2 gas phase inside the cell, assuming gas pressure decay is due solely to CO_2 molecules transferred into the liquid phase (Farajzadeh, Zitha & Bruining, 2009; Yang & Gu, 2006). The other way is to meter the pump rate of CO_2 required to maintain constant pressure in the cell (Karimaie & Lindeberg, 2017; Newell et al., 2018). Then both water swelling due to CO_2 dissolution and water evaporation, that is, the water vapor contribution to the gas pressure, are disregarded (Farajzadeh et al., 2007, 2009). It is also possible to implement porous media in PVT cell experiments (Karimaie & Lindeberg, 2017; Newell et al., 2018).

Results of PVT-cell Experiments

Yang & Gu (2006) conducted PVT cell experiments at two temperatures: 27 and 58 ˚C and in a pressure range of 26 to 75 bars. The water density was found to increase with increasing CO_2 concentration. Furthermore, the effective diffusion coefficient, which accounts for the overall effect of molecular diffusion and density-driven convection on the mass transfer of CO_2 into the water, was found to be almost two orders of magnitude larger than for pure molecular diffusion. Thus, Yang & Gu (2006) quantitatively showed that density-driven convection accelerates the mass transfer of CO_2 into water. While molecular diffusion is almost independent of pressure in the system, their experimental results also showed that the rate of convection increases linearly with pressure. This effect is attributed to higher interface concentration of CO_2 at higher pressure, leading to a higher mass transfer rate of CO_2 into the water, followed by a higher CO_2 concentration in water causing a larger density gradient in the mixture between the two, and a thus higher rate of convection.

PVT cell experiments were also performed by Farajzadeh et al. (2007) at a temperature of 30 ˚C and a pressure range of 10 to 50 bars. At early stages, the effective diffusion coefficient was found to be one order of magnitude larger than for pure molecular diffusion of CO_2 into water. In similarity to Yang & Gu (2006), this high mass transfer rate of CO_2 into the water was interpreted as density-driven convection. Similar results were also obtained by Karimaie & Lindeberg (2017), who found the CO_2 dissolution rate during convection to be one to two orders of magnitude faster than for pure molecular diffusion.

Furthermore, Farajzadeh et al. (2007) found the effective diffusion coefficient to decrease with time and become closer in magnitude to that expected from pure molecular diffusion at later stages, an effect that was attributed to a decrease in the driving force for natural convection over time, namely the density gradient; As time elapsed, the difference between the lowest and largest concentrations of CO_2 and the density gradient decreased, meaning that the CO_2 distribution became more uniform in the liquid. At a certain time, the density gradient was not large enough to sustain convection in the system. The experimental findings of Mojtaba et al. (2014) were in accordance with the above results, concluding that convection is more active at early stages and that its power decreases with time and eventually reaches zero, corresponding to pure molecular diffusion.

The observation made by Yang & Gu (2006) of a linear increase in the mass transfer rate of CO_2 into water with increasing pressure, was also supported by the experimental results of Farajzadeh et al. (2007, 2009), in which the authors concluded that even at slightly high pressures, the solubility of CO_2 into water is a strong function of the initial pressure, i.e., the initial concentration of CO_2 in the system. However, regardless of the initial pressure of the system, diffusion became the dominant mechanism for the mass transfer of CO_2 into the water at a certain time (Farajzadeh et al., 2007, 2009).

2.6.3.2 Visualization Experiments

Even through PVT cell experiments allow for high temperature and pressure conditions and a 3D development of the CO_2 dissolution pattern, one of the main drawbacks is that most of them do not allow visualization of the CO_2 dissolution process (Newell et al., 2018). Visualization experiments can be performed in Hele-Shaw cells, composed of two flat discs, of which at least one is transparent to allow visualization of the process (Thomas, Dehaeck, & De Wit, 2018). The sight discs are oriented parallel to each other so that fluid flows in the narrow gap between them. They are sealed on the edges but allow injection and release of CO_2 to maintain a pre-set constant pressure inside the cell (Faisal et al., 2015; Thomas et al., 2015). Common for Hele-Shaw cells used for visualization of the CO_2 dissolution process, is that they are partially filled with liquid and optionally porous medium, and sub- or supercritical CO_2 is brought above it (Kneafsey & Pruess, 2011; Thomas et al., 2015).

The geometry can differ from one cell to another; The transparent discs can be either circular (Amarasinghe, Fjelde, Rydland, Chauhan, & Guo, 2018; Khosrokhavar et al., 2014) or rectangular (Faisal, Chevalier & Sassi, 2013, 2015; Kneafsey & Pruess, 2010, 2011; Mojtaba et al., 2014; Thomas et al., 2018) and of different proportions. A general drawback considering experiments conducted in Hele-Shaw cells is that the width of the system remains limited, such that only a few fingers can be followed in time (Thomas et al., 2018). The gravity influence can be varied by tilting the cell (Kneafsey & Pruess, 2010). Liquid properties, such as density and viscosity, can be varied by means of varying the liquid content (Kneafsey & Pruess, 2011): For instance, water and its salinity or oil. Porous media properties, such as porosity and permeability can be varied through varying the cell content; In case of bulk liquid, the porosity is equal to one and the permeability can be varied by means of disc spacing (Faisal et al., 2013, 2015). In the case of porous media, the porosity and permeability can be varied by means of different grain sizes (Amarasinghe et al., 2018; Kneafsey & Pruess, 2011). All these variations are reflected in different Rayleigh numbers (Faisal et al., 2013, 2015; Kneafsey & Pruess, 2010, 2011).

When the cell content is bulk liquid, the flow occurring between the two discs is mathematically analogue to Darcy flow in porous media (Faisal et al., 2015; Kneafsey & Pruess, 2010, 2011; Mojtaba et al., 2014). For a Hele-Shaw cell with parallel discs of spacing b, the intrinsic absolute permeability, k, of the cell is given by (Faisal et al., 2013, 2015; Kneafsey & Pruess, 2010; Thomas et al., 2015):

$$k = \frac{b^2}{12}$$

As there is a direct relation between absolute permeability and Rayleigh number, it follows that the corresponding Rayleigh number is given by (Faisal et al., 2015):

$$Ra = \frac{\Delta\rho g b^3}{12\phi\mu D}$$

Homogeneous permeability fields in bulk liquid experiments are obtained by making the inside of the parallel discs from smooth flat glass (Faisal et al., 2015; Kneafsey & Pruess, 2010). Most experiments conducted in Hele-Shaw cells so far was intended to be performed with homogeneous permeability fields. However, most of these papers (Faisal et. al., 2015) report on naturally occurring variations in the spacing between the parallel discs, which involves somewhat larger spacing near the centre of the cell than near the edges. This corresponds to unintended heterogeneous permeability fields, in which the permeability is higher near the centre of the cells than near the edges. Intended heterogeneous permeability fields are obtained by sandblasting the inside of the parallel discs (Kneafsey & Pruess, 2011).

As mentioned, the contextual relationship between cell spacing and absolute permeability make flow behaviour in Hele-Shaw cells relevant to flow behaviour in porous media (Kneafsey & Pruess, 2011; Mojtaba et al., 2014). However, porous media can also be implemented in the experiments. Amarasinghe et al. (2018) obtained a homogeneous permeability field by filling the cell with homogeneous porous media.

Schlieren Method

The Schlieren method is an optical method applied to visualize density changes of the liquid content of the cell and relies on the fact that CO_2 dissolution increases the water density, which is the driving force of density-driven convection (Khosrokhavar et al., 2014; Thomas et al. 2015, 2018). The Schlieren setup is sensitive to refractive index gradients, which is the closest measurable quantity to density (Thomas et al., 2015). As illustrated in Figure 2.7, a light source is located behind the cell, and beams are sent through it via two achromatic lenses towards the camera (Khosrokhavar, Elsinga, Farajzadeh & Bruining, 2014). Initially, before bringing CO_2 into the system, the refractive index is constant, meaning that the beam is not deflected. The refractive index is lower for liquids in which CO_2 is dissolved, deflecting the beam. Thus, the Schlieren method has shown to be a useful tool in visualizing density-driven convection without interfering with the reactive system.

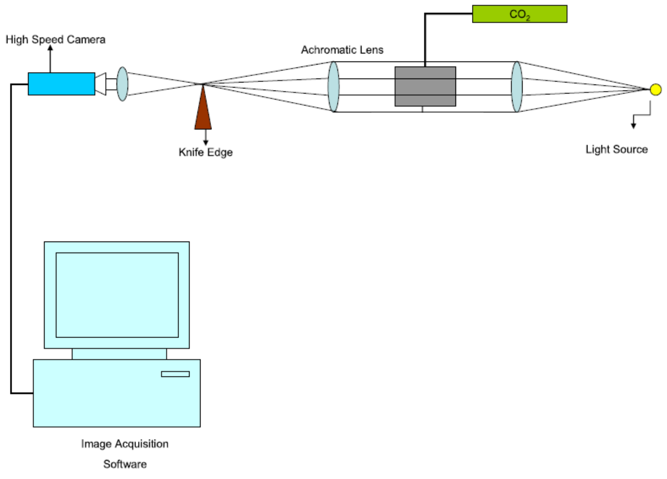

Figure 2.7: An illustration of the Schlieren setup. The figure is slightly modified from Khosrokhavar et al. (2014).

There are two main drawbacks concerning the Schlieren method: The first is that density-driven convection is difficult to visualize in pure water due to small density contrasts between the CO_2-saturated and unsaturated water (Khosrokhavar et al., 2014; Thomas et al., 2015). Thus, the setup must be very sensitive to detect density-driven convection in pure water. NaOH solutions can be used as an alternative to pure water, as chemical reactions between the base and the weak acid created by CO_2 dissolution, produce a product which is much denser than the reactants. Although this allows visualization of density-driven convection, it is at the expense of not interfering with the reactive system. The second drawback is that the Schlieren method can only be applied in the absence of porous media (Khosrokhavar et al., 2014). However, Khosrokhavar et al. (2014) claim that the same processes that take place in bulk liquid also take place in porous media, but the effect may be more pronounced for bulk flow.

Results of Schlieren Experiments

Visual experiments applying the Schlieren method were carried out by Khosrokhavar et al. (2014) at a constant temperature of 39 ˚C and at two pressures, 64 and 84 bars, to visualize density-driven convection at sub- and supercritical conditions, respectively. The spacing between the sight discs was 11.6 mm. Some experiments were performed by bringing subcritical CO_2 above various liquid phases, including pure water, highly saline water and oil. Fingers were observed within the first minute in all liquid phases, but density-driven convection was strongest in oil, followed by pure water, and weakest in highly saline water. This is attributed to the higher and lower density contrasts which are further reflected in higher and lower Rayleigh numbers, respectively. An experiment was also performed by bringing supercritical CO_2 above pure water. Fingers were observed to initiate immediately upon contact between supercritical CO_2 and water.

Thomas et al. (2018) also performed experiments using the Schlieren method. These were carried out in a large Hele-Shaw cell at room temperature and atmospheric pressure. The spacing between the sight discs was 1 mm. The experiments were performed by bringing CO_2 above various liquid phases, from pure water to water with 5 M salt concentration. In agreement with the results of Khosrokhavar et al., (2014), Thomas et al. (2018) found that an increased salt concentration hinders instability development and thus delays the onset of convection and decreases the rate of convection as well as the interactions between the fingers.

pH Indicator Method

An alternative to the Schlieren method is the optical pH indicator method, which allows the use of porous media in the cell (Amarasinghe et al., 2018). CO_2 dissolution in water forms a weak acid which decreases its pH (Faisal et al., 2013; Kneafsey & Pruess, 2011; Mojtaba et al., 2014; Thomas et al., 2015). Thus, the areas where the pH decreases below the specific transition range of a pH-sensitive indicator are highlighted by a change in colour. The chemistry forming the basis for this method was presented in Section 2.2.2.

A pH indicator is a salt composed of a metal ion and its corresponding base, which exists as a natural dye through its acid-base properties (Thomas et al., 2015). It appears as one colour in its protonated form and another colour in its deprotonated form. Initially, before bringing CO_2 into the system, the H^+ concentration of the water is constant and the dominant form of the pH indicator should appear in the colour of its deprotonated form. The pH indicator concentration should be as low as possible, presuming that the colour of the solution is clearly observable. This is because the pH indicator itself is a weak acid, and therefore decreases the pH of the water when added to it so that it turns into its protonated form if the concentration is too high.

Water in equilibrium with air has a pH of approximately 5.6, while water in equilibrium with CO_2 has a pH of approximately 3.9 at atmospheric pressure (Kneafsey & Pruess, 2011). Only a few pH indicators have a transition range corresponding to this pH decrease (Thomas et al., 2015). Among these, the pH indicator appearing to be most extensively used in visualization experiments is bromocresol green (BG) (Kneafsey & Pruess, 2010, 2011; Faisal et al., 2013). BG has a transition range from blue at pH values above 5.4 to yellow at pH values below 3.8 (Kneafsey & Pruess, 2010). Another pH indicator that can be used in visualization experiments, is Bromocresol Purple (BP) (Thomas et al., 2015). BP has a transition range from purple at pH values above 6.8 to yellow at pH values below 5.2. Slightly different transitions ranges characterize these two indicators. BP changes colour at larger pH values than BG, indicating that BP should be more sensitive to CO_2 dissolution of than BG. A third pH indicator with a transition range at slightly higher pH values than BP is Bromothymol Blue (BTB) (Amarasinghe et al., 2018). Its colour changes from blue at pH values above 7.6 to yellow at pH values below 6.0. This transition range indicates that BTB should be even more sensitive to CO_2 dissolution than BP. Based on this reasoning and available equipment, BTB is the chosen pH indicator for the experiments presented in Section 4 of this thesis. However, BTB requires the addition of a base to the water to appear in the colour of its deprotonated form before introducing CO_2 to the system (Amarasinghe et al., 2018).

There are some underlying assumptions when using pH indicators for visualization purposes (Thomas et al., 2015): The first assumption is that the effect of the pH indicator itself is negligible (Thomas et al., 2015). However, Thomas et al. (2015) did not find the presence of a pH indicator in water to substantially impact the development of the convective pattern. The second assumption is that the pattern shown by the pH indicator is equal to the pattern that develops when the water density increases by CO_2 dissolution. Thomas et al. (2015) showed through their experiments that the shape and properties of the pattern appearing, strongly depend on the pH indicator in use. This is explained by the existence of iso-pH curves inside a finger. The pH gradually decreases from the edge of the finger to its centre, where the concentration of dissolved CO_2 is highest. Thus, a given pH indicator will only highlight areas within the iso-pH curve corresponding to its specific transition range. Thus, the finger of denser water may have a larger extent than that detected by the pH indicator.

Despite these possible disadvantages, the simplicity of the pH indicator method is sufficient for the present study to build upon the pH indicator method in the implementation of Hele-Shaw cell visualization experiments.

Results of pH Indicator Experiments

By use of the pH-indicator method, Faisal et al. (2013, 2015) performed Hele-Shaw cell experiments with homogeneous permeability fields created by bulk water at room temperature and atmospheric pressure. The Rayleigh number was varied by means of varying the spacing between the sight discs from 0.3 to 1 mm. The study reported on an earlier onset and stronger convection with increasing Rayleigh number. For the experiment with 1 mm spacing, observations of fingers were done within the first minute of the experiment. Faisal et al. (2013, 2015) also reported on coalesce of fingers into fewer and thicker ones.

Other experimental work conducted in Hele-Shaw cells has reported similar findings. Kneafsey & Pruess (2010) performed homogeneous permeability experiments with bulk water and 0.7 mm spacing between the sight discs at ambient conditions. By use of the pH-indicator method, they reported on the occurrence of a diffusive layer within 1 minute, which further developed into fingers at 3 minutes. As time progressed, Kneafsey & Pruess (2010) also reported on coalesce of fingers into fewer and thicker ones. Cell scale convection was also observed to affect the convective pattern.

Kneafsey & Pruess (2011) also conducted experiments with bulk water in the cell and a heterogeneous permeability field. The observations here was that fingers formed more rapidly with a heterogeneous permeability field than with a homogeneous permeability field. The fingers also appeared to be influenced by the heterogeneity of the cell; They tended to form at specific locations, and some tended to stay in the same location over time.

Only a few experiments have been conducted with porous media in the Hele-Shaw cell and water as pore fluid (Amarasinghe et al., 2018; Mojtaba et al., 2014). Amarasinghe et al. (2018) carried out such experiments with a homogeneous permeability field at 22 ˚C temperature and 10 bars pressure. The study reported that density-driven convection was visible in high-permeable porous media but not in low-permeable porous media, in which a uniform CO_2 dissolution process was observed. Furthermore, the rate of CO_2 dissolution was found to increase with increased permeability.

To the best of my knowledge, there have so far not been performed experiments with porous media with heterogeneous permeability fields whose main purpose has been visualization of CO_2 dissolution by pH indicator. Based on this reasoning and available equipment, porous media of both homogeneous and heterogeneous permeability fields are implemented in most of the experiments that will be presented in Section 4 of the present study.

3 Experimental Methods

3.1 Apparatus

3.1.1 The Hele-Shaw Cell

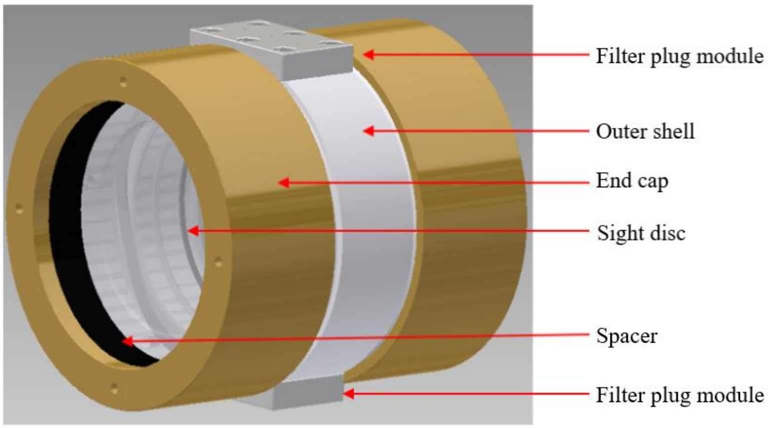

Figure 3.1: A 3D illustration of the Hele-Shaw cell used in the experiments, including its constituent parts (modified from Amarasinghe et al., 2018).

In the experiments, the process of CO_2 dissolution takes place inside an experimental cell of type Hele-Shaw. Accordingly, the main component of the apparatus is the Hele-Shaw cell itself. Figure 3.1 shows the different constituents of the cell, which has working conditions at pressures and temperatures of approximately 10 bars and room temperature. The experimental environment of the cell is enclosed by an outer shell and two parallel transparent sight discs, which are held in position by spacers and end caps on both sides (Figure 3.1). Both the outer shell, the spacers, and the end caps are made from Polyoxymethylene (POM) material, while the sight discs are made from Polymethyl Methacrylate (PMMA) material, also known as plexiglass.

The sight discs allow visualization of the patterns resulting from CO_2 dissolution in the liquid phase. The lateral surface of the two sight discs has two recesses for O-rings, to provide a closed experimental environment. As stated in Section 2.5, the density-driven convection process occurs due to density differences and the process of interest is, therefore, gravity-influenced. Consequently, the sight discs are oriented in the vertical plane. Each of the sight discs has a diameter of 170 mm. They are separated by a small gap of 5 mm, providing a narrow, cylindrical experimental environment. The calculated volume of the experimental environment of the cell is approximately 113.5 ml (excluding volumes of filter plug modules, glass filter, and valves):

$$V_{test} = \pi \cdot \left(\frac{d}{2}\right)^2 \cdot l = \pi \cdot \left(\frac{170\ mm}{2}\right)^2 \cdot 5\ mm = 113490\ mm^3 \underline{\underline{\approx 113\ ml}}$$

The outer shell contains two removable filter plugs, one located at the top of the cell and the other at the bottom. These are also made from POM material and have several purposes; First and foremost, they provide access to the experimental environment of the cell, allowing filling and draining of liquid solution and optionally porous medium. Each of the filter plugs has three openings, allowing gas connection directly into, as well as out of the cell in case of pressure build-up. Each of them also has recesses for two O-rings, as well as a flat rubber gasket between the filter plug and the cell’s outer shell, to prevent leakages. The bottom filter plug has a glass filter mounted inside, with pore sizes of approximately 10 to 16 µm, to avoid glass beads escaping the experimental environment. The top filter plug does not have a glass filter because glass beads escaping the top of the cell have not proven to be a problem.

3.1.2 Piping and Instrumentation Diagram

A Piping and Instrumentation Diagram (P&ID) for the experimental setup is shown in Figure 3.2. The P&ID shows that electronic signals from a computer software control the pump, specifying a precise flow rate to be maintained. The pump, a Quizix QX, consists of two independently controlled motor-driven pistons, securing a pulse-free operation. Two piston cells are connected to the pump via a 3-way-2-stem manifold with manual gate valves, in which one of the valves (V_1) is connected to a piston cell containing nitrogen gas (N_2), while the other valve (V_2) is connected to a piston cell containing carbon dioxide gas. Via another 3-way-2-stem manifold with manual gate valves, N_2 or CO_2 gas from the piston cells is first allowed to access the experimental environment of the cell through opening the valves (V_3) or (V_4), respectively. The gas flows into the headspace of the cell through the centre opening of the top filter plug.

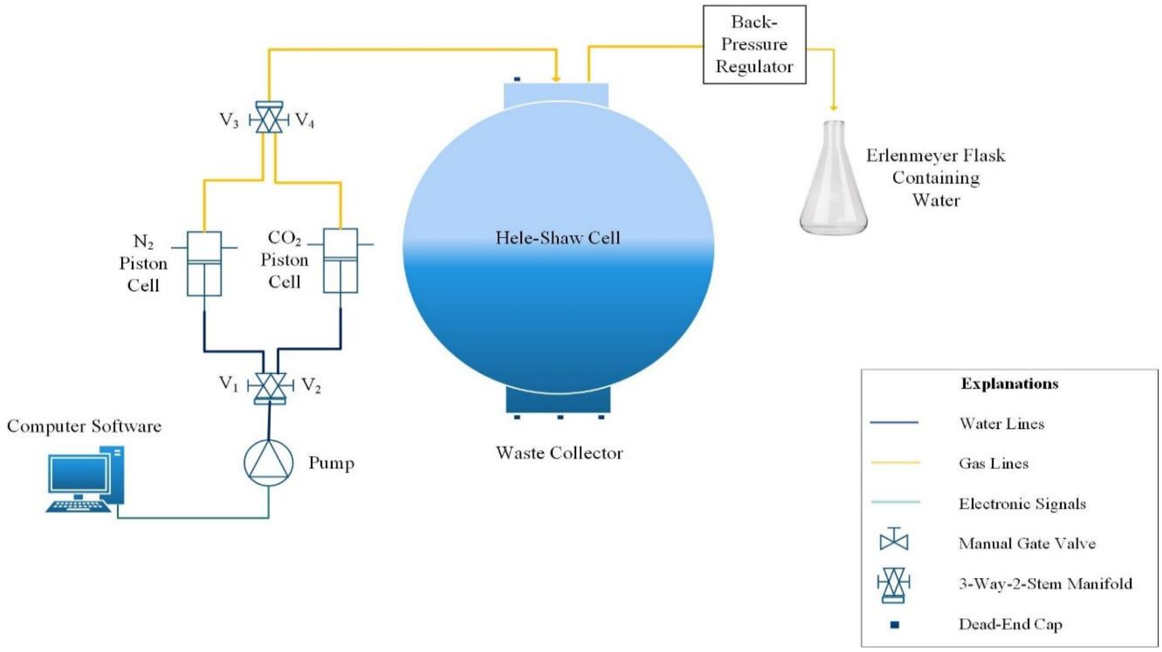

Figure 3.2: P&ID for the experimental setup. The figure is modified from Amarasinghe at al. (2018).

A back-pressure regulator is connected to the right opening of the top filter plug. The back-pressure regulator controls the pressure inside the cell, by releasing gas from the cell whenever the cell pressure exceeds a pre-set pressure, which in this setup is set at approximately 10 bars. Thus, the back-pressure regulator prevents sudden development of high pressure inside the cell and maintains the pressure approximately constant. Bubbles in the water inside the Erlenmeyer flask is an indicator of when the back-pressure regulator releases gas. The left opening of the top filter plug has a dead-end cap, which is used to release the pressure inside the cell after an experiment is completed.

3.2 Chemicals and Materials

3.2.1 pH Indicator Solution

Based on Section 2.6.3 and available equipment, an aqueous BTB pH indicator solution was used to visualize the CO_2 dissolution process by means of pH change. Preparation of a 0.004 weight percent (wt%) BTB solution was performed by dissolving 0.04 g of BTB salt ($C_{27}H_{27}Br_2O_5SNa$) into 16 mL of 0.01 M Sodium Hydroxide (NaOH) solution. The solution was further diluted with distilled water up to a total volume of 1 L before it was stirred on a magnetic stirrer for an hour. NaOH was added to make sure that the solution was in its deprotonated form before injection of CO_2 into the system. A pre-mixed BTB solution has a pH of approximately 9.5. Figure 3.3 shows the BTB solution in its deprotonated and protonated form, appearing blue and yellow, respectively. In the experiments, the BTB solution represents formation water, either as a bulk solution or as pore fluid. However, it will hereafter simply be referred to as “water”.

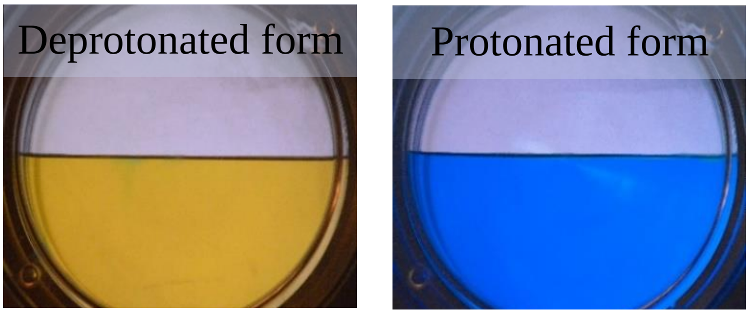

Figure 3.3: BTB solution appearing blue in its deprotonated form and yellow in its protonated form.

3.2.2 Porous Media

Water-wet glass beads were used to represent porous media. The glass beads used for these experiments can be separated into four different groups based on particle size distribution (PSD) and absolute permeability, as shown in Table 1. The beads range in PSD from 70 to 110 µm, to 400 to 600 µm. Pictures showing the sizes of the beads relative to each other are shown in Figure 3.4. They range in absolute permeabilities from approximately 4 000 to 76 000 mD. The permeabilities of the different bead packs were previously determined by waterflooding of tubes (Amarasinghe, Fjelde, Rydland & Guo, 2019).

Table 1: Shows particle size distribution (PSD) and absolute permeability of the four different types of glass beads used in the experiments.

Glass beads sizes (µm)	Approximated absolute permeability (mD)
400 – 600	76 000
300 – 400	52 000
100 – 200	16 000
70 – 110	4 000

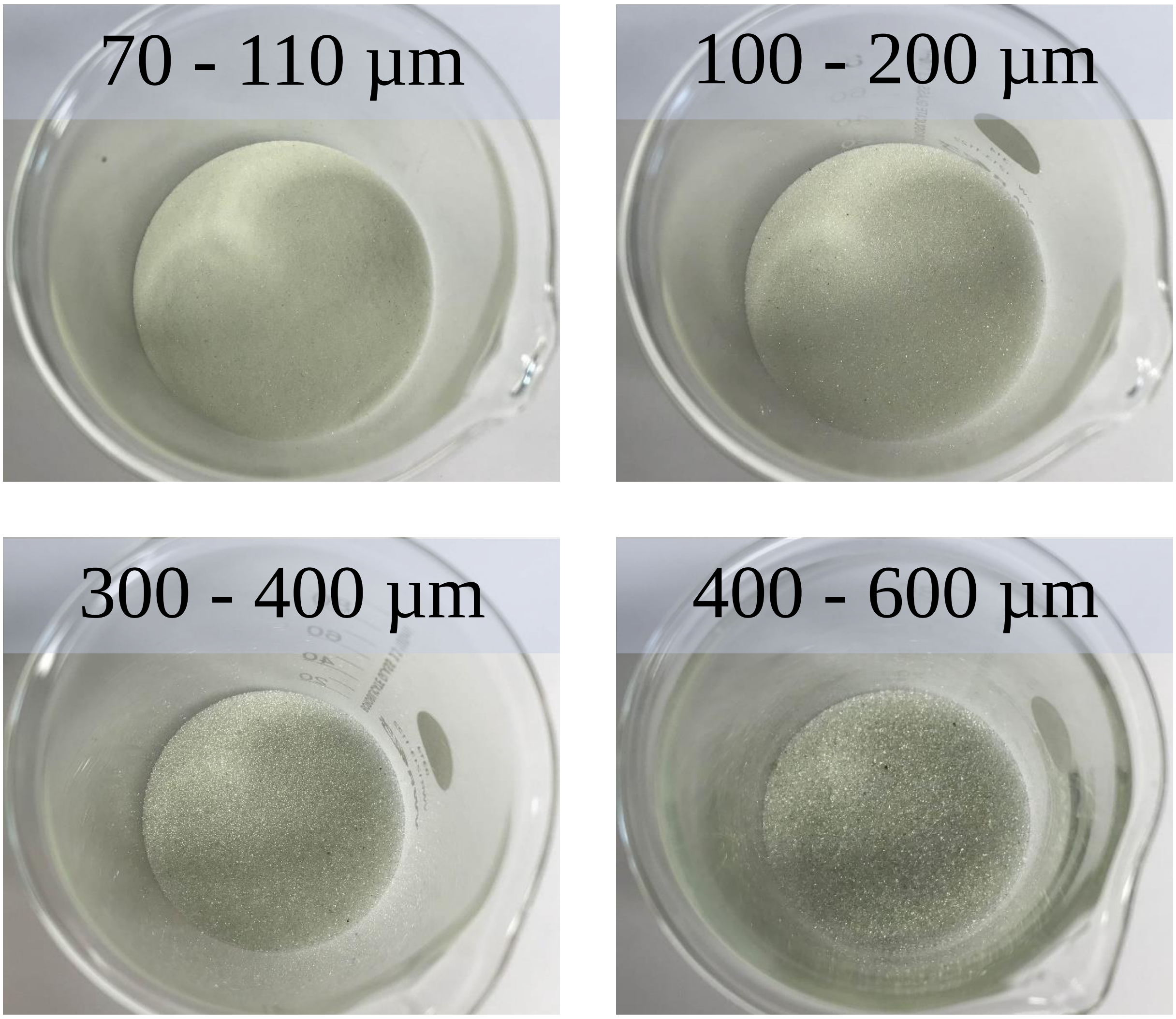

Figure 3.4: Pictures of the four different types of glass beads used in the experiments.

3.2.3 Injection Gases

3.2.3.1 Nitrogen Gas

N_2 was injected from the N_2 piston cell through the gas lines and into the headspace of the cell for two reasons; To detect possible leakages in the setup and to pressurize water and porous media within the cell before injecting CO_2. N_2 was preferred to other gases because it is inert and does not react with the water to cause a pH change.

3.2.3.2 Carbon Dioxide Gas

As stated in Section 2.2.1, the CO_2 density is approximately 2.0 kg/m^3 at normal conditions (Emami-Meybodi et al., 2015), and denser than air and N_2, which at normal conditions have densities of approximately 1.2 kg/m^3 (Faisal et al., 2013, 2015; Kneafsey & Pruess, 2010). Thus, CO_2 settled above the CO_2-water interface by replacing the air and N_2 through the back-pressure regulator opening in the top of the cell. As stated in Section 2.2.1, CO_2 becomes supercritical at temperatures and pressures above 31.1 °C and 73.9 bara. Since the working conditions of the cell are room temperature and 10 bars pressure, the conditions of the injected CO_2 were well below the supercritical conditions of CO_2. Thus, in these experiments, CO_2 was gaseous. CO_2 dissolves in the water according to the equilibria presented in Section 2.2.2.

3.3 Procedure

3.3.1 Preparing the Cell

Prior to each experiment, the Hele-Shaw cell and its constituent components were cleaned thoroughly, by alternately pouring methanol and distilled water through the cell from its top opening. A waste collector was kept below the bottom opening of the cell. Methanol was used for cleaning due to its miscibility with water. Careful cleaning of the cell was important to avoid contamination and was a means of achieving good results each time an experiment was run. All parts were left drying over the night, along with the open cell.

When preparing the cell for filling, the cell had to be oriented in such a way that the two openings where the filter plug modules can be mounted, were localized at the top and bottom of the cell. The bottom of the cell was closed by the filter plug when filling the cell, otherwise, leakage occurred. To prevent leakage, the easiest way was to mount the bottom filter plug module, with a glass filter, rubber gasket between it and the outer shell, as well as the dead-end caps, before installing the cell in the customized stand. The screw holes for mounting the filter plugs onto the cell’s outer shell are arranged in a rectangular 2x3 pattern.

The screws were tightened in a zigzag pattern to avoid skewed assembly and subsequent leakage. When the bottom filter plug was readily mounted, the cell itself was installed in a customized stand, that also provided space for emptying the cell through the bottom filter plug module when the experiments are completed.

3.3.2 General Procedure for Filling the Cell

The cell was filled with water and optionally glass beads, depending on the specific experiment to be conducted (See Section 3.3.3). Water was injected into the cell by lowering a syringe with a long needle from the top opening of the cell. The syringe tip was positioned so that it barely touched one of the sight discs inside the cell and allowed the water to flow along one of the sight discs, to avoid splashes and droplets that were stuck on the sight discs.

When the porous media was implemented in the experiment, it was filled manually into the cell after the water from the top opening using a beaker. The top opening is elongated, allowing movement of the beaker along with this opening while pouring the glass beads, for smooth filling of the cell. Excess water was removed using a syringe with a long needle extending into the cell. Remaining glass beads along the top opening were removed with wet wipers. Otherwise, leakage could occur when pressurizing it.

When the cell was filled to an adequate amount, either with water only or with both water and porous media, the rubber gasket was placed around the top opening of the cell and the top filter plug module was mounted without a glass filter inside. To avoid leakage, the same zigzag pattern as for the bottom filter plug module screws was applied when tightening the top filter plug module screws,

3.3.3 Specific Procedure for Filling the Cell

The first type of experiment was performed in the absence of a porous medium in the cell. The second types of experiments were performed with a porous medium of homogeneous permeability in the cell. The third types of experiments were performed with porous media of heterogeneous permeability in the cell. Experiment-specific procedures for filling the cell will be presented for these three types of experiments in the following subsections.

3.3.3.1 With Bulk Water

A syringe was used to inject approximately 75 mL of water into the cell. Since some of the water escaped the experimental environment of the cell upon pressurization, this water volume corresponded to approximately one half of the cell volume after pressurization.

3.3.3.2 With a Porous Medium of Homogeneous Permeability

First, a syringe was used to inject water into the cell. Then, the beads of interest were filled into the cell and an increase in the initial water level was observed. The ambition was to arrange the glass beads as horizontal as possible. This was obtained by extending a thin rigid stick into the cell and arrange the beads in the desired manner. To obtain comparable results between the experiments with homogeneous permeability, a small mark was set on each side of the cell to show the level height of the beads. Excess water was removed using a syringe until the water level was approximately 1 cm above the level of the beads.

3.3.3.3 With Porous Media of Heterogeneous Permeability – Horizontal Layering

Again, a syringe was used to inject water into the cell and the beads of interest were filled into the cell causing an increase of the initial water level. To obtain horizontally layered alternating permeability, three layers of porous media was implemented in this type of experiments. The lower and the upper layer had the same permeability, while the middle layer had a different permeability. To obtain comparable results between these experimental cases, three small marks were set on each side of the cell to show the ideal levels of the different beads layers. The ambition was to arrange the different layers as horizontal as possible. This was obtained by a similar method as presented in Section 3.3.3.2. Excess water was removed using a syringe until the water level was approximately 1 cm above the level of the beads.

3.3.3.4 With Porous Media of Heterogeneous Permeability – Vertical Layering

Water was injected into the cell by use of a syringe. Then, flexible plastic straws were arranged vertically inside the cell from the top opening, as shown in Figure 3.5 – A. The diameter of the straws is approximately 8 mm, whereas the spacing between the sight discs is approximately 5 mm. Therefore, the straws provided vertical barriers for the different types of porous media within the cell. To obtain vertically layered alternating permeability, three layers of porous media were implemented in this type of experiments. The layers on the sides of the cell had the same permeability, while the layer in the centre had a different permeability. First, the largest beads were filled into the cell (See Figure 3.5 – B). In Figure 3.5 the largest beads correspond to the centre vertical layer. Then the smallest beads were filled into the cell (See Figure 3.5 – C). The largest beads were filled first because the smallest beads tended to bypass the barriers provided by the straws when the barriers were not sealed by larger beads. At last, the same type of beads as in the centre vertical layer was filled into the straws from their top openings. The initial water level increased different for each vertical section bounded by the straws. To obtain comparable results between this type of experiments, small marks on each side of the cell showed the ideal levels of the beads layers. The ambition was to arrange the top of the different vertical layers as horizontal as possible. This was obtained by a similar method as presented in Section 3.3.3.2. The straws were then gently pulled vertically out from the cell. Again, excess water was removed using a syringe, until the water level was approximately 1 cm above the level of the beads.

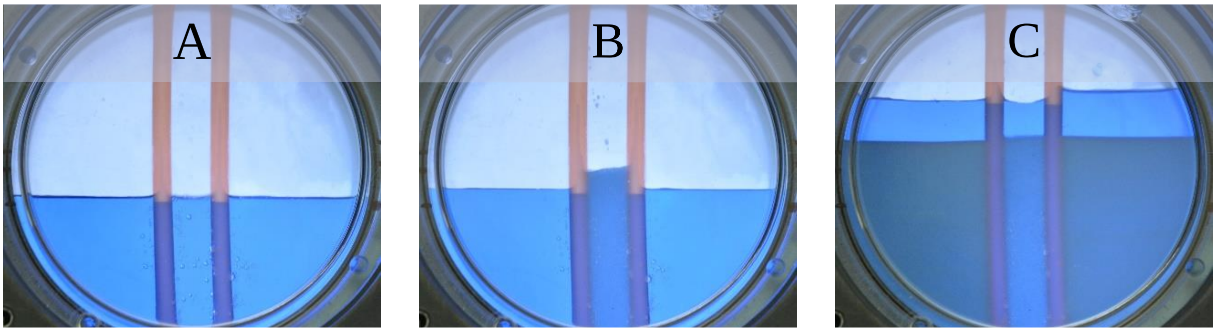

Figure 3.5: Step by step filling procedure for the vertically layered alternating permeability types of experiments.

3.3.4 Pressurizing the Cell

When pressurizing the cell, the P&ID in Figure 3.2 was followed. The cell was initially filled with water, optionally porous medium, and air at approximately 1 bar pressure. Before pressurizing the cell by injecting N_2, the gas line going from the 3-stem-2-valve manifold to the experimental environment of the cell was flushed with N_2 for a few seconds to avoid CO_2 from previous experiments being injected into the cell before initiating the new experiment. The cell was pressurized up to approximately 10 bars pressure and the air initially present in the cell was displaced by N_2. The porous media was also packed properly due to pressure exposure. In each experiment, some of the water escaped the experimental environment of the cell upon pressurization; Some entered the filter and valves belonging to the bottom filter plug module, and some flowed in between the outer shell of the cell and the lateral surfaces of the two sight discs. Injection of N_2 was terminated before initiation of CO_2 injection.

The point in time when CO_2 injection from the CO_2-containing piston cell into the headspace of the cell began, represented the initiation of an experiment. A camera was started just before this point in time. CO_2 injection displaced the N_2 present in the cell and a plume of CO_2 settled above the water surface. The pump injected CO_2 a constant flow rate of 0.1 ml/min throughout the experiments. This flow rate was enough to maintain a layer of CO_2 above the water surface, kept at an approximately constant pressure of 10 bars by the back-pressure regulator.

3.3.5 Documentation, Processing, and Analysis of the Results

A digital single-lens reflex (SLR) camera was set up at the same height as the cell and used for photographing the experiments at specific time intervals. Behind the cell, a white dropdown was mounted to provide a uniform background for the pictures.

To obtain better images for presentation in Section 4, image processing was performed using Adobe Lightroom Classic CC software. The image processing consisted of cropping the images and adjusting the yellow and blue saturation. Saturation adjustments resulted in areas of lower pH and higher CO_2 concentrations appearing yellower, while areas with higher pH and lower CO_2 concentrations appearing bluer.

For a better comparison between the various experiments presented in Section 4, the images were analysed using ImageJ software (Syed, Sobh, Ravaioli, Popescu & Mohamed, 2015). The maximum vertical thickness of the CO_2-saturated layer, relative to the known cell diameter, was measured for chosen images from each experiment and plotted against time. If fingers occurred, the vertical length of the longest finger was measured, as in the right image shown in Figure 3.6.

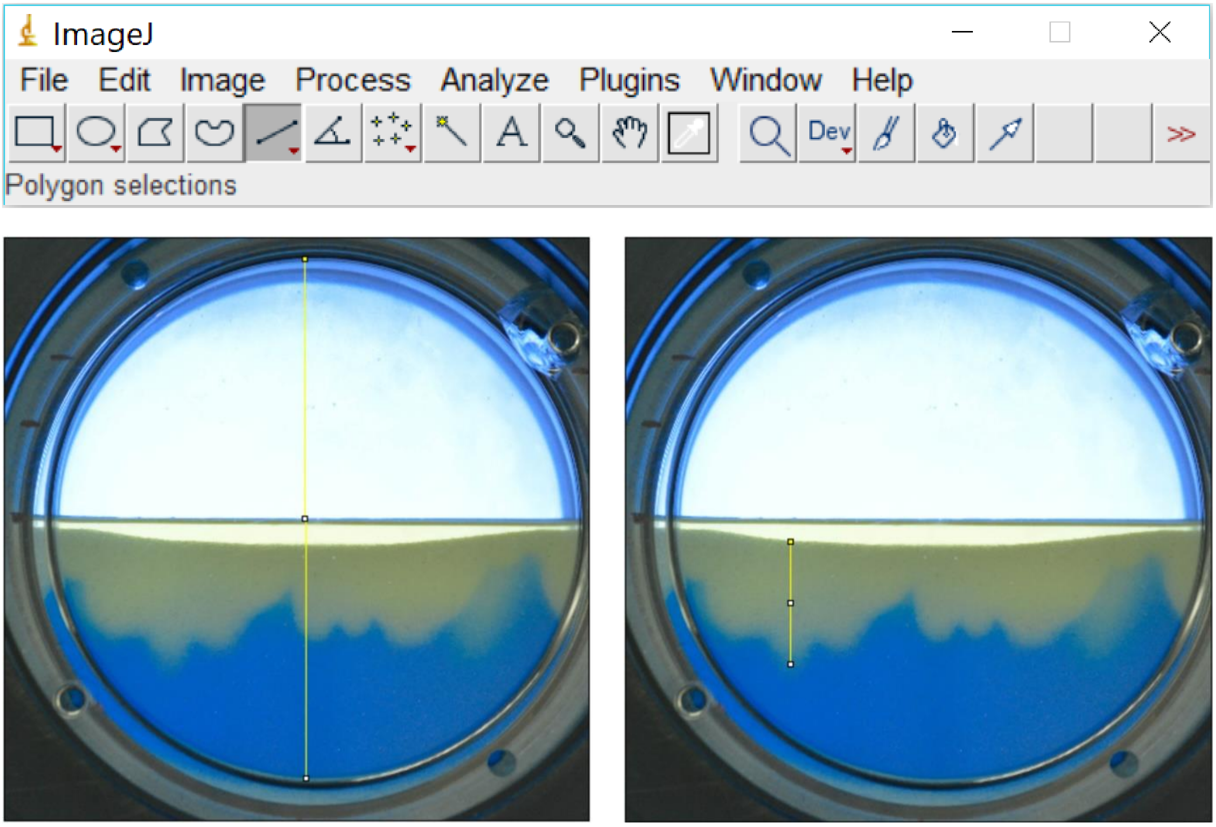

Figure 3.6: The ImageJ toolbar, how to set the global scale and how to measure the length of the longest finger.

3.3.6 Depressurizing the Cell

After an experiment, the cell was depressurized. This was performed by making sure that the pump was stopped and that all valves were closed. The dead-end cap on the top filter plug module was then opened carefully, while visually observing the pressure evolution inside the cell. A sudden rise in the water level could be observed due to CO_2 expansion and dissolution from the water phase. If the water level raised towards the top filter plug, the top dead-end cap was closed and opened carefully again after a few seconds. When the water level stagnated, the pressure inside the cell was atmospheric and the dead-end cap could be opened fully.

After depressurization, the two filter plugs were removed, and the cell was emptied through the bottom opening. The top filter plug was disassembled by removing the dead-end cap and disconnecting the gas and back-pressure regulator lines. The six screws on the top filter plug were loosened and a flat head screwdriver was applied in between the outer shell and the top filter plug to jack off the latter. The rubber gasket was removed as well. The bottom filter plug and rubber gasket were disassembled in a similar manner as the top filter plug. However, when the bottom filter plug module was removed, the cell content flowed out immediately, so a waste collector below was necessary to avoid a spill.

4 Results

The results of the bulk water experiment are first presented in Section 4.1. Subsequently, the results of experiments with homogeneous permeabilities are presented in Section 4.2. These experiments have been performed previously by Amarasinghe et al. (2018). Therefore, a basis for comparison already exists, and consequently, only one set of results is presented for each experiment. Most of the results presented in Section 4.2 serve as references, i.e. a basis of comparison for the interpretation of the experimental results presented in Section 4.3 and Section 4.4. The results presented in Section 4.3 and Section 4.4 are from experiments with heterogeneous permeabilities, arranged with horizontally and vertically alternating permeability layers, respectively. To assure that the results are reproducible to a certain degree, two sets of results are presented for each experiment. Table 2 gives an overview of how the experimental results will be presented.

For each experiment, an explanation of the results is presented, followed by the corresponding image story showing the course of the experiment. At the end of each section, graphs showing the thickness of the CO_2-saturated layer against time, are presented.

Table 2: An overview of the results that will be presented in Section 4.

Sections	**Type of Experiment**	**Porous Media Permeabilities [mD]**
Section 4.1	Bulk Water	None
Section 4.2	Homogeneous Permeabilities	76 000
		52 000
		16 000
		4 000
Section 4.3	Heterogeneous Permeabilities – Horizontal Layering	76 000, 16 000, and 76 000
		52 000, 16 000, and 52 000
		16 000, 52 000, and 16 000
Section 4.4	Heterogeneous Permeabilities – Vertical Layering	16 000, 76 000, and16 000
		16 000, 52 000, and 16 000
		52 000, 16 000, and 52 000

4.1 Bulk Water Experiments – Absence of Porous Medium

Since all the forthcoming experimental results will be presented with approximate permeabilities of the porous media used in each experiment, the absolute permeability of the cell was calculated based on the formula presented in Section 2.5.3. The spacing, b, between the two parallel sight discs is 5 mm, and the corresponding absolute permeability, k, of the cell can thus be calculated:

$$k = \frac{b^2}{12} \approx \frac{(5 \cdot 10^{-3}\ m)^2}{12} \approx 2 \cdot 10^{-6}\ m^2 \underline{\underline{\approx 2 \cdot 10^{9}\ mD}}$$

When CO_2 was injected into the cell and contacted the water, rather quick development of a thin CO_2-saturated layer in the top of the water column was observed already at 1 minute (See yellow layer in Figure 4.1). This is interpreted as CO_2 dissolution in water in terms of molecular diffusion, as described in Section 2.5. Graph 1 supports this interpretation, as the curve has a low slope during the first 1.5 minutes. However, the diffusive layer had a slightly variable thickness already after 1 minute, indicating the development of perturbations from pure diffusive flow behaviour. At 1.5 minutes, the slope of Graph 1 becomes steeper, indicating that density-driven convection initiated at this time. This is in accordance with Figure 4.1, which shows that small fingers formed below the diffusive layer at 2 minutes. At 3 minutes, several fingers were observed to migrate vertically downwards from the diffusive layer. This is interpreted as density-driven convection, as described in Section 2.5. At 4 minutes, the fingers were longer and their fronts wider than for the fingers observed after 3 minutes. They were even longer and their fronts even wider at 5 minutes than at 4 minutes. Between 4 and 5 minutes, some fingers apparently merged, as the number of fingers decreased during this period.

Another interesting feature of the convection pattern can be observed in Graph 1, in which the slope of the curve decreases after approximately 4.5 minutes. The explanation for this can be seen in Figure 4. After 5 minutes, the first finger fronts reached the edge of the cell and cell scale convection effects occurred. The fingers that had not yet migrated to the edge of the cell was apparently also influenced by the cell scale convection, as they began to migrate slightly laterally. Similar cell scale convection effects was observed after 6 minutes as well and became more dominant after 7 and 8 minutes. After 8 minutes, the typical finger pattern observed at earlier times was no longer recognizable and the pattern appeared to be fully dominated by cell scale convection effects. Note that the thickness of the diffusive layer at the top of the water column apparently did not grow much during these 8 minutes.

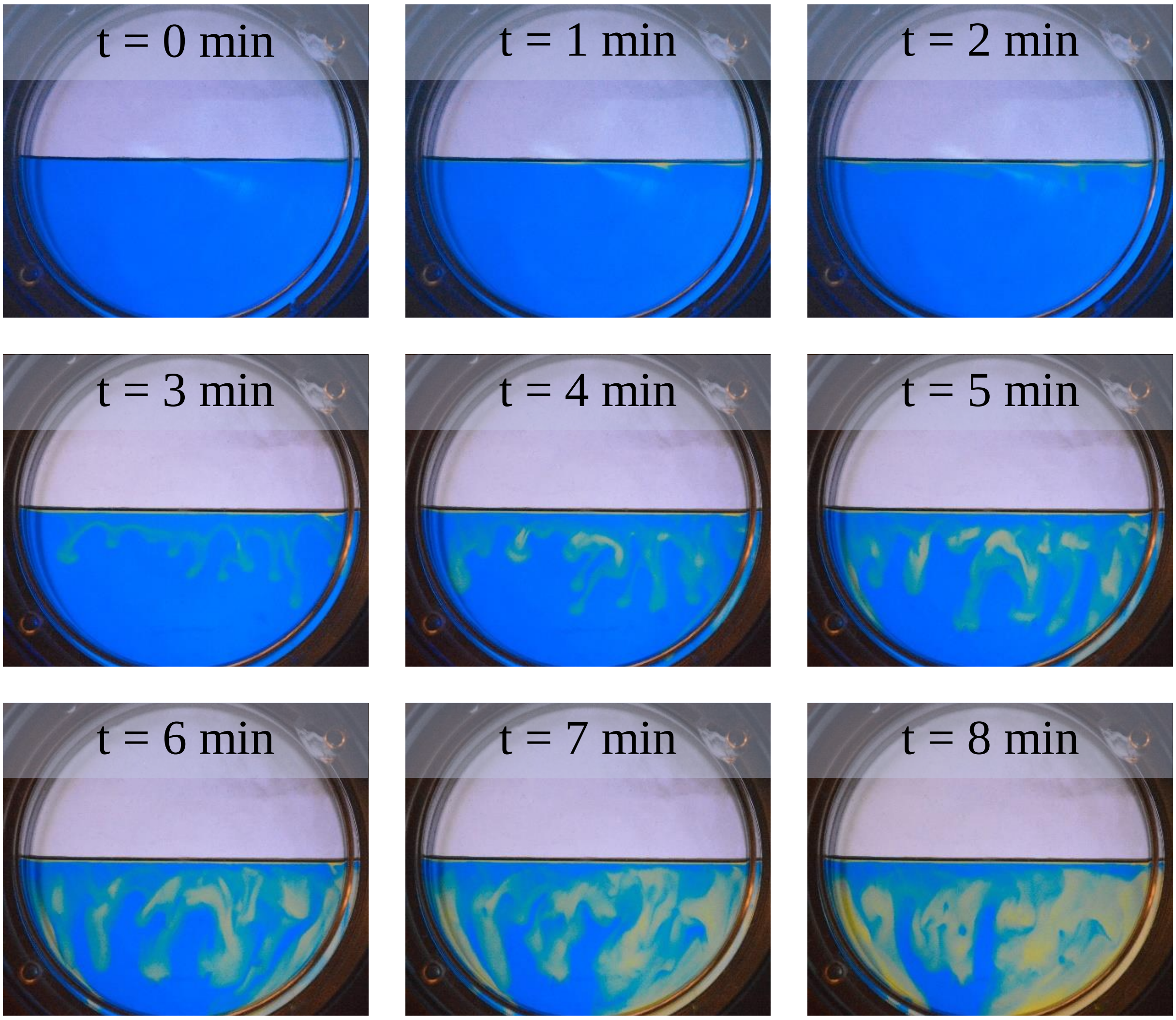

Figure 4.1: An image story showing the course of Experiment 4.1, where CO_2 dissolved in bulk water, with cell permeability of approximately $2 \cdot 10^9$ mD.

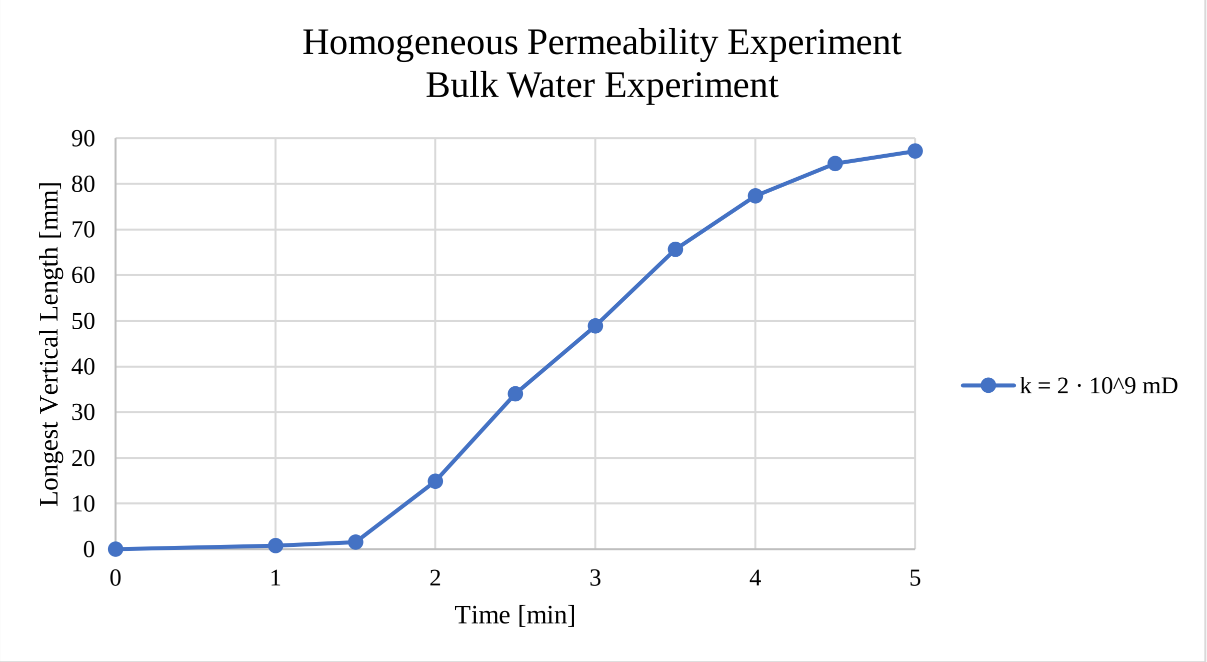

Graph 1: Length of the front of the CO_2-saturated layer vs. time for the bulk water experiment presented in Section 4.1.

4.2 Homogeneous Permeability Experiments – Reference Experiments

4.2.1 Porous Medium of ≈ 76 000 mD Permeability

When CO_2 was brought above a water-saturated porous medium of 76 000 mD permeability, a thin CO_2-saturated layer of homogeneous thickness was observed in the top of the porous medium, like for the bulk water experiment (Section 4.1). However, it appeared somewhat later for the experiment currently being presented, as a thin CO_2-saturated layer was first observed 5 minutes into the experiment (See yellow layer in Figure 4.2). As time proceeded towards 15 minutes, the front of the CO_2-saturated layer moved evenly downwards within the porous medium, causing its thickness to increase in a homogeneous manner. Based on the homogeneous thickness of the CO_2-saturated layer in Figure 4.2, molecular diffusion of CO_2 into the water within the pore space of the porous medium is assumed to have taken place at these early times. This is in accordance with Graph 2, in which the blue curve has a relatively low slope at these early times.

Irregularities were observed along the front of the CO_2-saturated layer after 30 minutes (See Figure 4.2). These irregularities caused the thickness of the CO_2-saturated layer to increase in a heterogeneous manner and indicated the development of perturbations from the pure diffusive flow regime. As time proceeded from 30 minutes, these irregularities became more pronounced and eventually developed into fingers, causing the degree of heterogeneity in the thickness of the CO_2-saturated layer to further increase. Based on Figure 4.2, it is not easy to say exactly at what time the perturbations developed into a convective flow regime. According to Graph 2 however, the slope of the blue curve starts increasing at 45 minutes, indicating the initiation of a density-driven convective flow regime.

As time went by, the finger pattern in Figure 4.2 appeared to remain quite similar to the initial finger pattern. That is, the fingers appeared to grow vertically downward in time, but were not observed to migrate significantly laterally as they grew. In Graph 2 the growth of the longest finger can be seen to decrease as its front approached the edge of the cell. According to Figure 4.2, the front of the longest finger reached the edge of the cell after 240 minutes. This can be observed from the decreased slope of the blue curve in Graph 2 for times greater than 210 minutes and indicates the initiation of cell-scale convection.

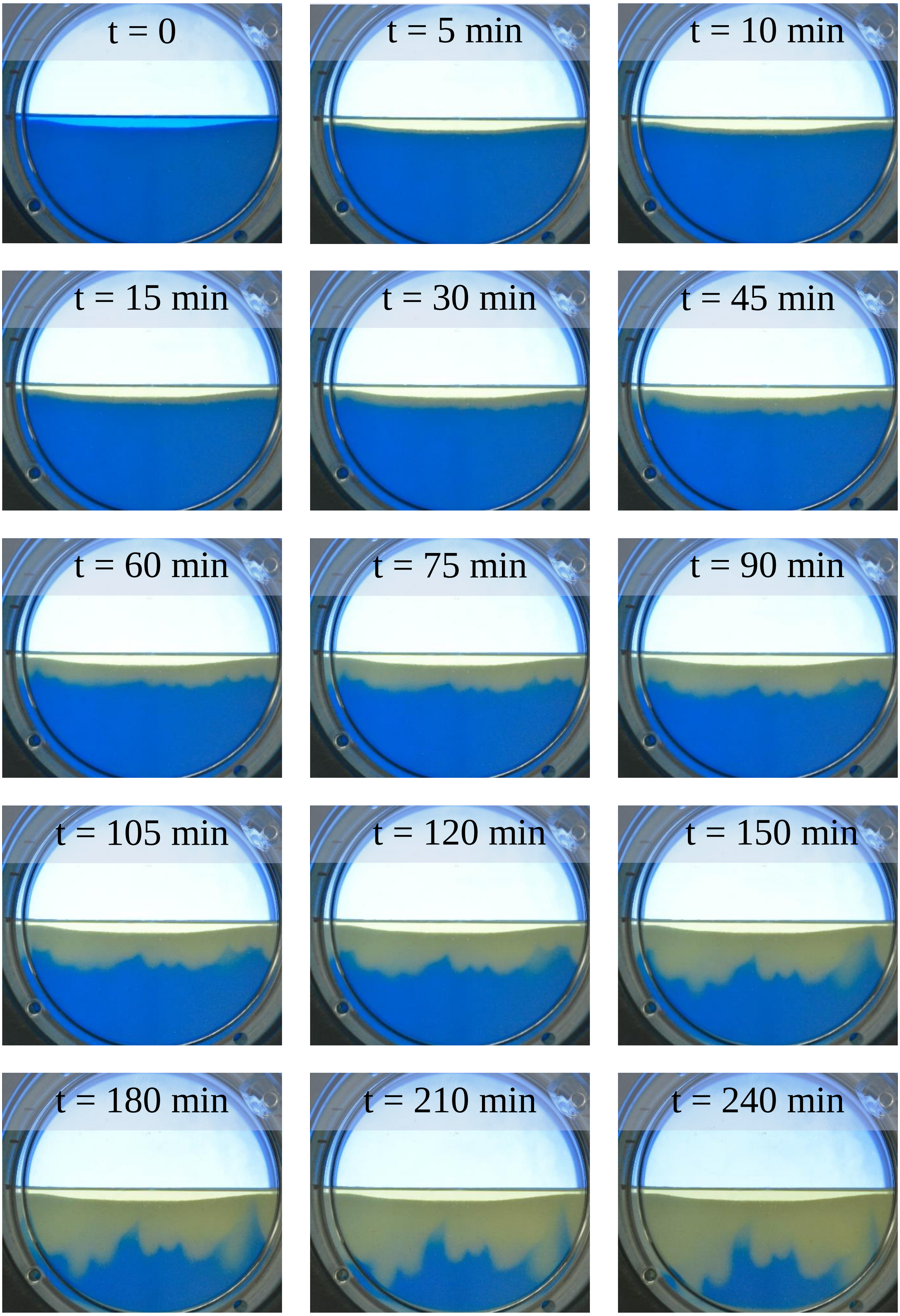

Figure 4.2: An image story showing the course of Experiment 4.2.1, where CO2 dissolved in a water-saturated porous medium of approximately 76 000 mD permeability.

4.2.2 Porous Medium of ≈ 52 000 mD Permeability

When CO_2 was brought in contact with a water-saturated porous medium of 52 000 mD permeability, a thin CO_2-saturated layer of homogeneous thickness was observed after 5 minutes (See yellow layer Figure 4.3), as for the experiment with a porous medium of 76 000 mD (Section 4.2.1). The thickness of the CO_2-saturated layer increased homogeneously as time proceeded towards 15 minutes. Again, based on its homogeneous thickness, molecular diffusion of CO_2 into the water-saturated porous medium is assumed having taken place at these early times. This is in accordance with the relatively low slope of the orange curve in Graph 2. Moreover, the orange curve coincides with the blue curve in Graph 2, which substantiates the interpretation of a diffusive flow regime at early times.

Irregularities were observed along the front of the CO_2-saturated layer after 30 minutes in Figure 4.3. This also matches the experiment with porous media of 76 000 mD permeability. Consequently, the thickness of the CO_2-saturated layer increased heterogeneously, indicating the development of perturbations from the pure diffusive flow regime. As time proceeded from 30 minutes, these irregularities became more pronounced and eventually developed into fingers, causing the degree of heterogeneity in the thickness of the CO_2-saturated layer to further increase. Based on Figure 4.3, it is difficult to say exactly at what time the perturbations developed into a convective flow regime, but according to Graph 2, and in accordance with the 76 000 mD experiment, the slope of the orange curve starts increasing 45 minutes into the experiment. This indicates the initiation of a density-driven convective flow regime. The density-driven convection that occurred in this experiment seemed weaker than the convection occurring in the experiment with a porous medium of 76 000 mD permeability. This can mainly be observed from Graph 2, in which the blue curve lies above the yellow curve at times greater than 90 minutes.

As time went on, the fingers observed in Figure 4.3 appeared to grow vertically downward in time but not to migrate significantly laterally as they grew. The front of the longest finger reached the edge of the cell after approximately 240 minutes. This can be observed from the decreased slope of the orange curve in Graph 2 for times greater than 180 minutes and indicates the initiation of cell-scale convection. The decrease in slope can also be explained by boundary effects from the edge of the cell, which was observed 150 minutes into the experiment. Such boundary effects seemed to counteract the downward movement of the CO_2-saturated layer and will be further commented on in the discussion in Section 5.2.2.

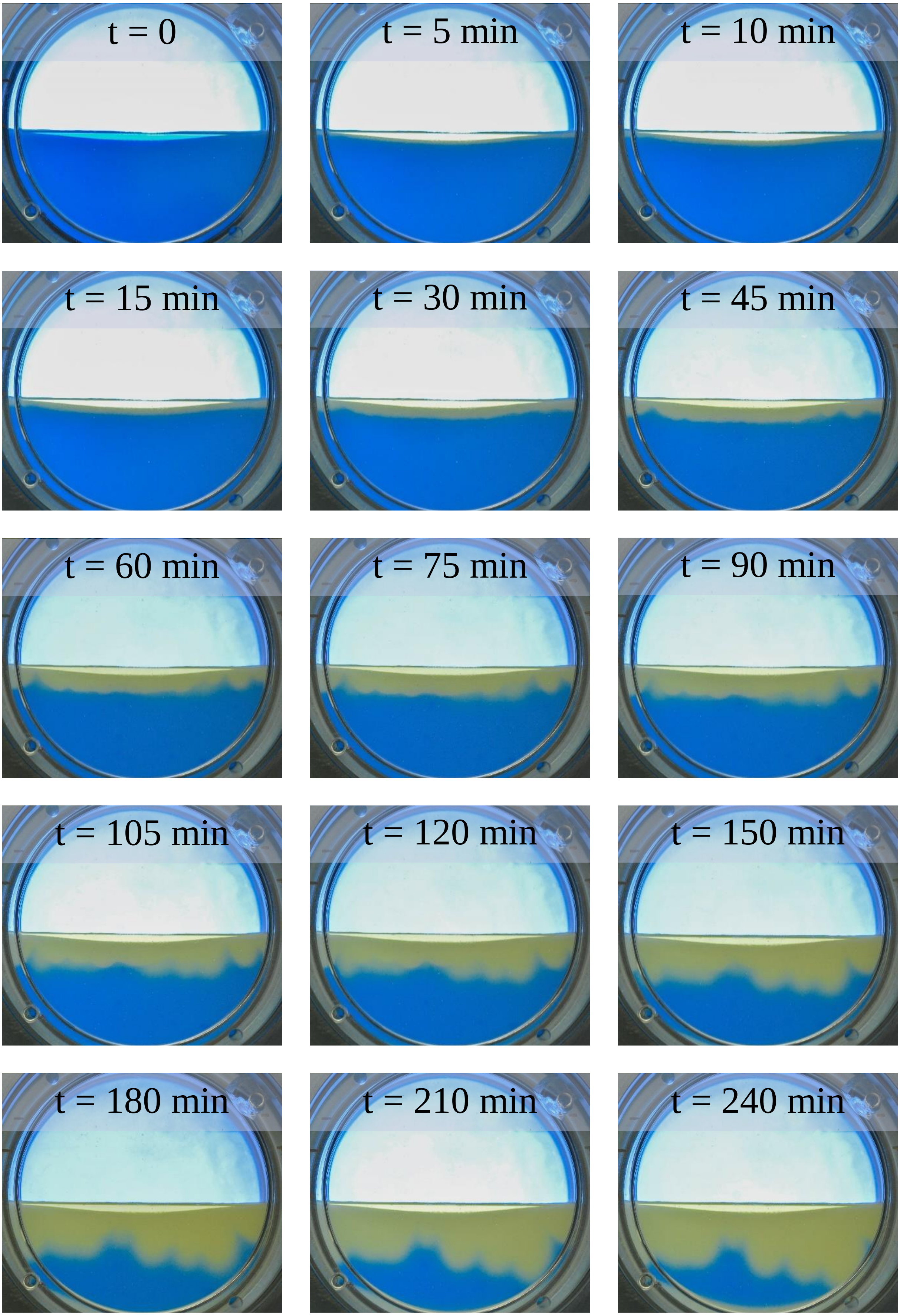

Figure 4.3: An image story showing the course of Experiment 4.2.2, where CO2 dissolved in a water-saturated porous medium of approximately 52 000 mD permeability.

4.2.3 Porous Medium of ≈ 16 000 mD Permeability

When CO_2 was injected into the cell and contacted the water-saturated porous medium of 16 000 mD permeability, a thin CO_2-saturated layer of homogeneous thickness was observed in the top of the porous medium after 15 minutes (See yellow layer in Figure 4.4). Based on the homogeneous thickness of the CO_2-saturated layer in Figure 4.4 and the low slope of the grey curve in Graph 2, this layer is interpreted as a diffusive layer caused by molecular diffusion of CO_2 into the water-saturated porous medium.

In contrast to the results of the experiments presented in the preceding sections, the front of CO_2-saturated layer moved evenly downwards within the porous medium, so that the thickness of the diffusive layer increased homogeneously. No fingers were observed throughout the experiment, nor did the downward movement of the CO_2-saturated interface appear to accelerate as time proceeded. In Graph 2, the grey curve looks almost flat at times from 105 minutes and beyond. This indicates that the diffusive flow regime dominated throughout the experiment.

Boundary effects from the edge of the cell were observed at 210 minutes, and after 240 minutes these boundary effects became very clear and seemed to counteract the downward movement of the diffusive layer. Graph 2 even shows that the yellow-blue interface becomes slightly thinner at times greater than 240 minutes.

4.2.4 Porous Medium of ≈ 4 000 mD Permeability

When CO_2 was brought above a water-saturated porous medium of 4 000 mD permeability, a thin CO_2-saturated layer in the top of the porous medium was observed 15 minutes into the experiment (See yellow layer in Figure 4.5). Again, based on the homogeneous thickness of the layer in Figure 4.5 and the low slope of the grey curve in Graph 2, this layer is interpreted as a diffusive layer caused by molecular diffusion of CO_2 into the water-saturated porous medium.

Like the experiment with a porous medium of 4 000 mD permeability (Section 4.2.3) and as opposed to the experiments with porous media of 76 000 and 52 000 mD permeability (Section 4.2.1 and Section 4.2.2), the CO_2-saturated layer in the experiment currently being presented, moved evenly downwards within the porous medium throughout the experiment, causing the thickness of the diffusive layer to increase homogeneously. No fingers were observed throughout the experiment, nor did the downward movement of the CO_2-saturated layer appear to accelerate as time proceeded. This indicates that the diffusive flow regime dominated throughout the experiment.

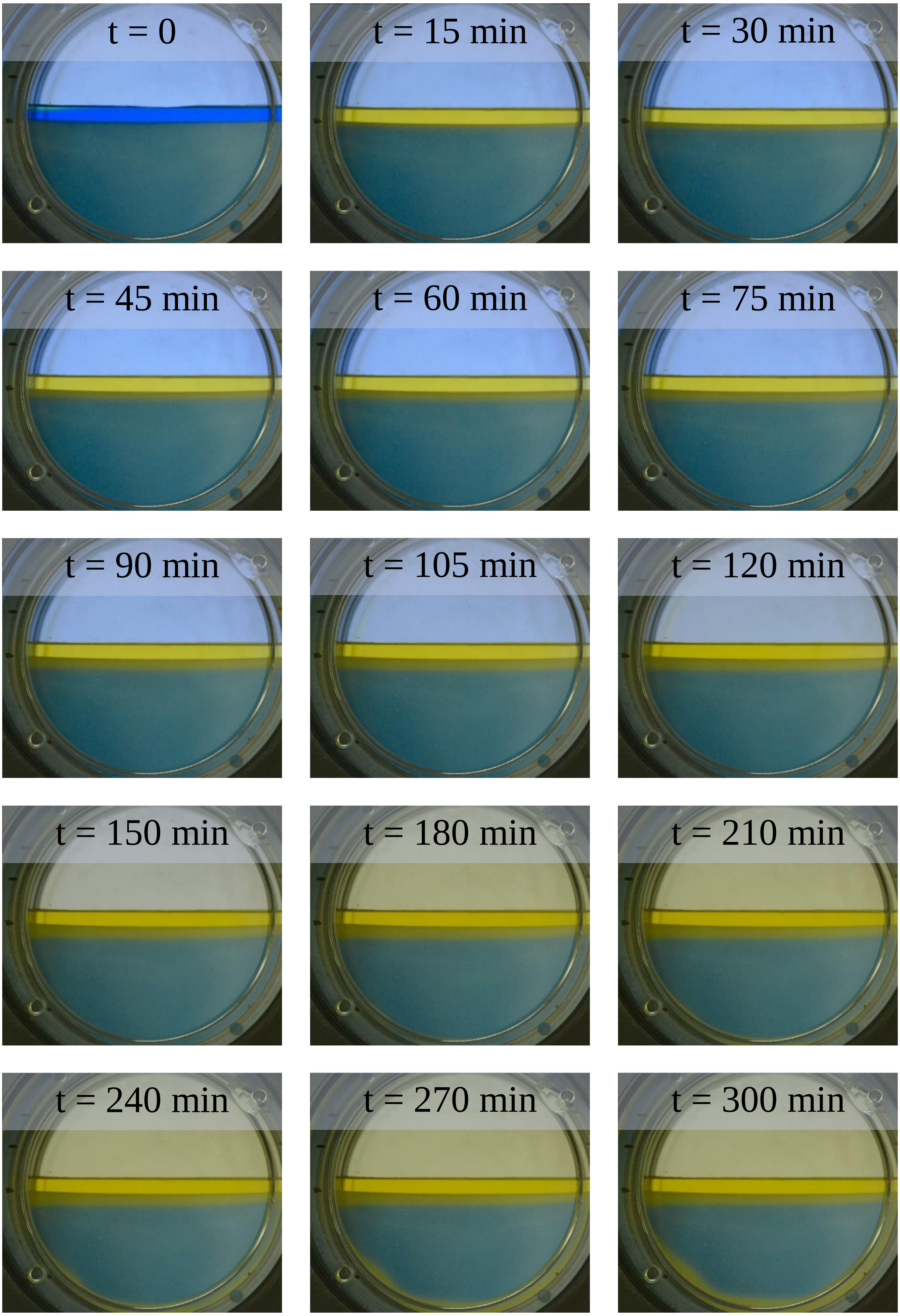

Figure 4.4: An image story showing the course of Experiment 4.2.3, where CO2 dissolved in a water-saturated porous medium of approximately 16 000 mD permeability.

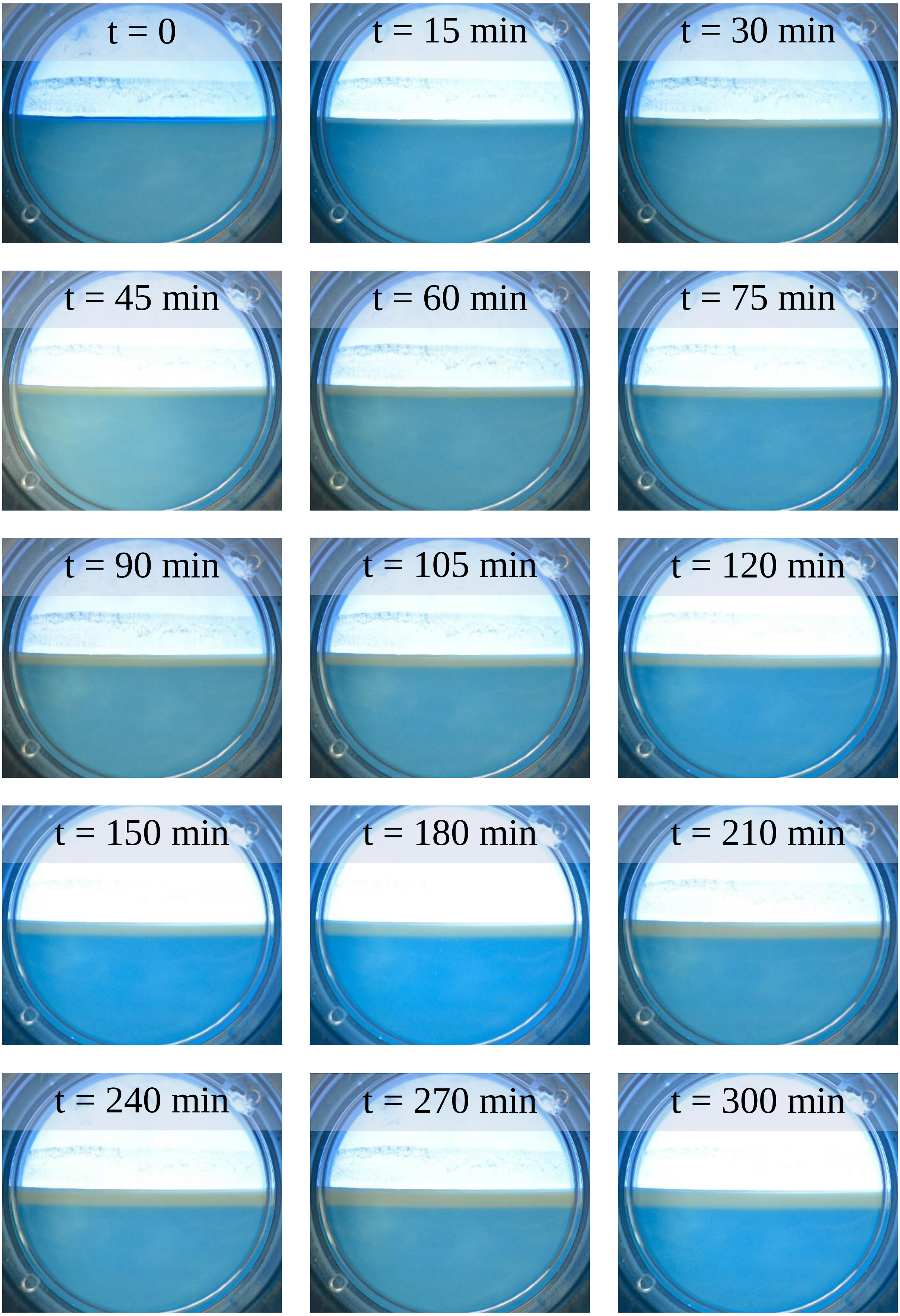

Figure 4.5: An image story showing the course of Experiment 4.2.4, where CO2 dissolved in a water-saturated porous medium of approximately 4 000 mD permeability.

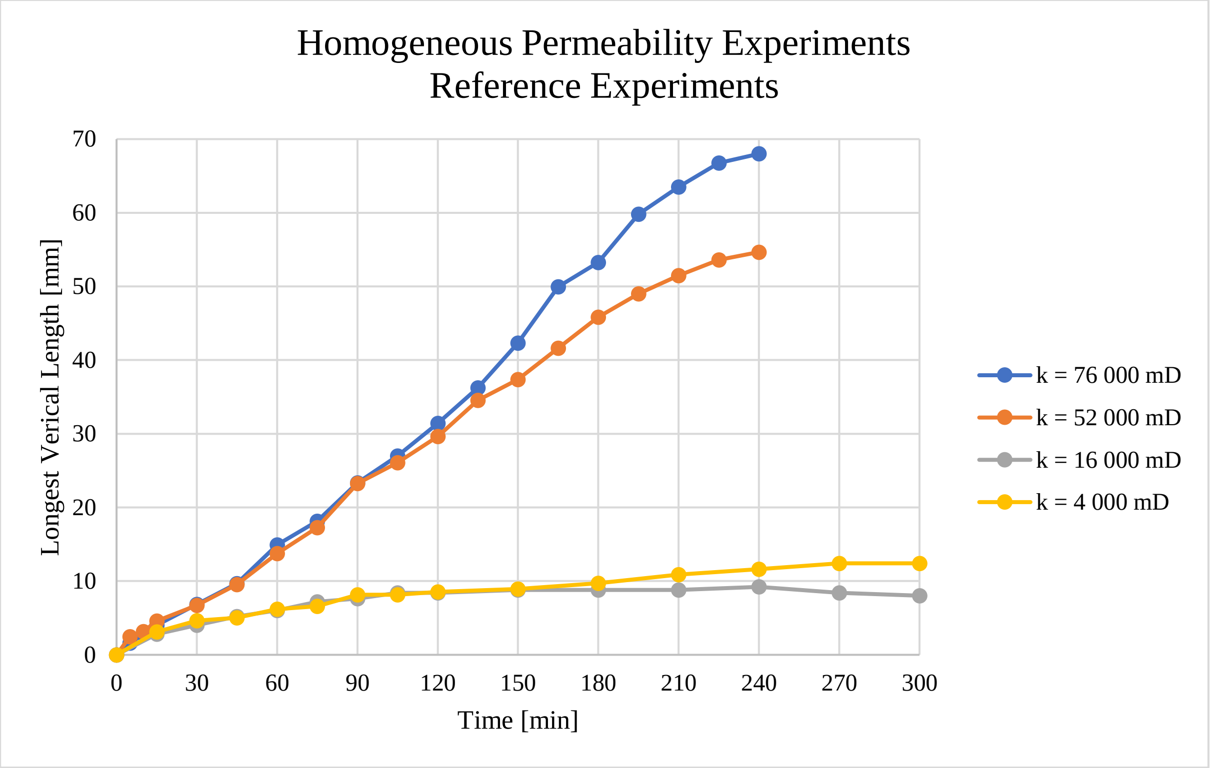

Graph 2: Length of the front of the CO_2-saturated layer vs. time for the reference experiments with homogeneous permeability presented in Section 4.2.

4.3 Heterogeneous Permeability Experiments – Horizontal Layering

4.3.1 Porous Media of ≈ 76 000, 16 000 and 76 000 mD Permeability

In the experiments with heterogeneous permeability created by horizontal layering, the cell was mainly filled with a high-permeable porous medium of approximately 76 000 mD (Dark blue in Figure 4.6 and Figure 4.7). A thin layer of a low-permeable porous medium of approximately 16 000 mD (Light blue and marked by an arrow in Figure 4.6 and Figure 4.7), was placed horizontally in between the high-permeable layers.

4.3.1.1 Set 1

When CO_2 came in contact with the water-saturated porous media, a thin CO_2-saturated layer of homogeneous thickness was observed in the top of the porous media after 5 minutes (See yellow layer in Figure 4.6). Its thickness increased homogeneously as time proceeded to 15 minutes, which agrees with the reference experiment of 76 000 mD (Section 4.2.1) and is interpreted as molecular diffusion of CO_2 into the water-saturated porous media. This is in accordance with Graph 3, in which the blue curve has a relatively low slope at these times.

As for the reference experiment of 76 000 mD permeability, irregularities were observed along the front of the CO_2-saturated layer at 30 minutes, indicating the development of perturbations from the pure diffusive flow regime. Based on Figure 4.6, it is difficult to say exactly at what time the perturbations developed into density-driven convection, but the slope of the blue curve in Graph 3 starts increasing 60 minutes into the experiment, indicating the onset of convection. This was later than for the reference experiment of 76 000 mD permeability (Grey curve in Graph 3), in which convection initiated after 45 minutes.

The longest finger fronts migrated into the low-permeable layer after approximately 90 minutes. Between 105 and 180 minutes, the thickness of the CO_2-saturated layer became more homogeneous than at 90 minutes, indicating that the fingers were attenuated when migrating through the low-permeable layer. This is in accordance with the results of the 16 000 mD permeability reference experiment (Section 4.2.3). The migration through the low-permeable layer is also observed in Graph 3, as the slope of the blue curve decreases between 105 and 180 minutes, suggesting deceleration of the fingers.

After 105 minutes, the finger fronts had mostly migrated through the low-permeable layer. The front of the CO_2-saturated layer redeveloped an irregular shape and convection eventually initiated. According to Graph 3, the slope of the blue curve increases from 180 minutes, indicating this initiation. The finger pattern appeared quite similar to the initial pattern.

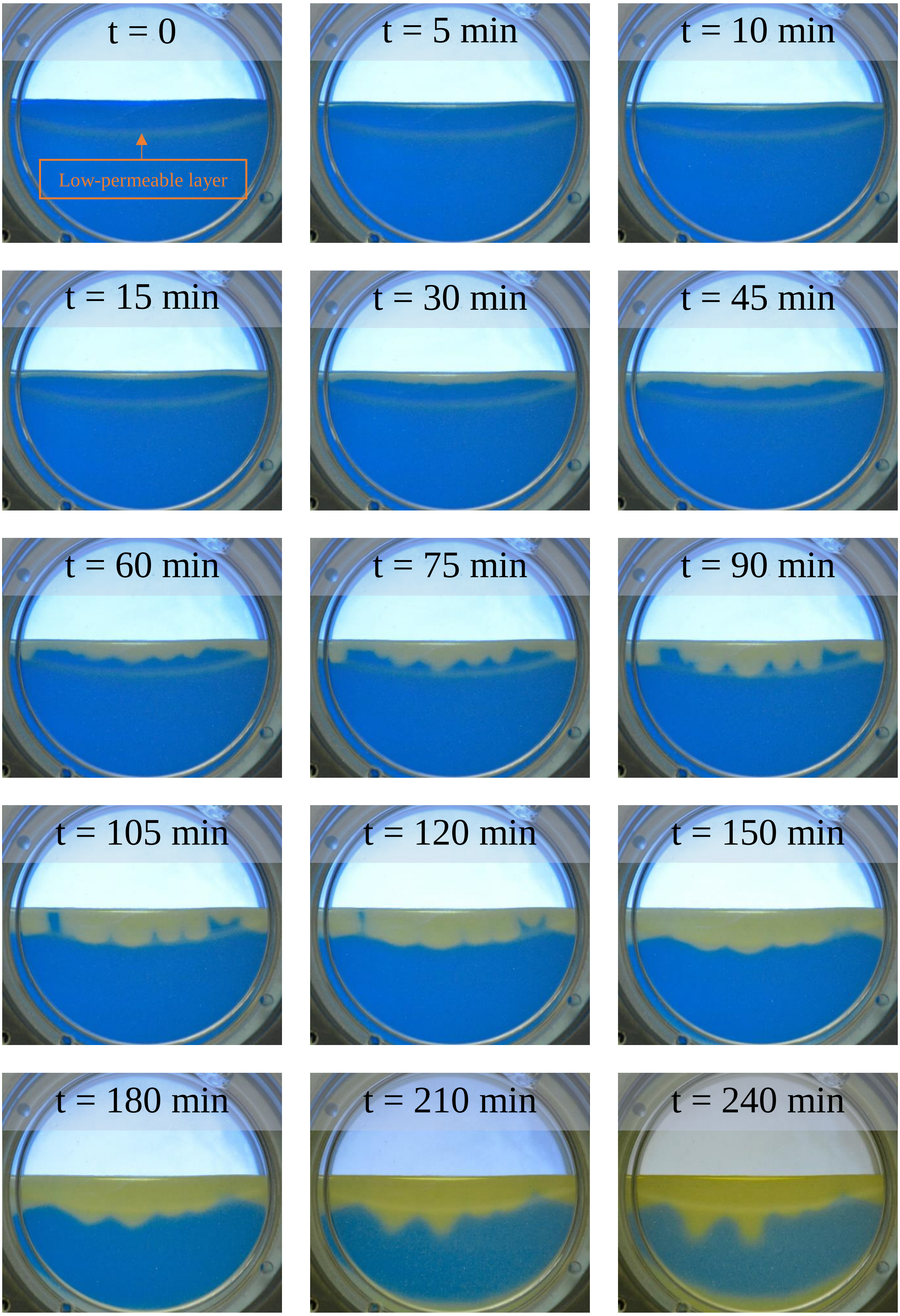

Figure 4.6: An image story showing the course of Experiment 4.3.1 – Set 1, where CO2 dissolved in water-saturated porous media of horizontally alternating permeability of approximately 76 000 mD, 16 000 mD and 76 000 mD.

4.3.1.2 Set 2

When CO_2 was injected into the cell and contacted the water-saturated porous media, a thin CO_2-saturated layer of homogeneous thickness was observed in the top of the porous media after 5 minutes (See yellow layer in Figure 4.7). Again, this is interpreted as molecular diffusion of CO_2, which is in accordance to Graph 3, in which the orange curve has a relatively low slope during the first 5 minutes, equal to that of Set 1 and the 76 000 mD permeability reference experiment (Section 4.2.1).

In contrast to the results of Set 1 and the reference experiment of 76 000 mD permeability, irregularities developed along the front of the CO_2-saturated layer already at 10 minutes, indicating the development of perturbations from the pure diffusive flow regime. It is difficult to have an idea exactly at what time the perturbations developed into a density-driven convection based on Figure 4.7, but the slope of the orange curve in Graph 3 starts increasing steeply at 10 minutes, indicating an early initiation of a convective flow regime, compared to that of Set 1 and the reference experiment of 76 000 mD permeability (Blue and grey curves in Graph 3), in which convection initiated after 60 and 45 minutes, respectively. This indicates that the density-driven convection was stronger for the experiment currently being presented.

The finger fronts had mostly migrated into the low-permeable layer after 45 minutes. From 45 to 60 minutes, the thickness of the CO_2-saturated layer became more homogeneous than at 30 minutes, meaning that the fingers were attenuated when migrating through the low-permeable layer. This was in accordance with the results of the 16 000 mD permeability reference experiment (Section 4.2.3), in which fingers were not observed. As for Set 1, the migration through the low-permeable layer is visible in Graph 3, as the slope of the orange curve decreases between 30 and 90 minutes, meaning the deceleration also applies after their fronts have migrated through the low-permeable layer.

Most of the finger fronts had migrated through the low-permeable layer 75 minutes into the experiment. The front of the CO_2-saturated layer redeveloped an irregular shape and convection eventually initiated. According to Graph 3, the slope of the orange curve starts increasing again from 90 minutes, indicating this initiation. The slope of the orange curve seems to be approximately equal to that of the grey curve, corresponding to the reference experiment of 76 000 mD permeability. The finger pattern that occurred in the lower high-permeable layer did not seem to have any connection to the pattern observed above the low-permeable layer.

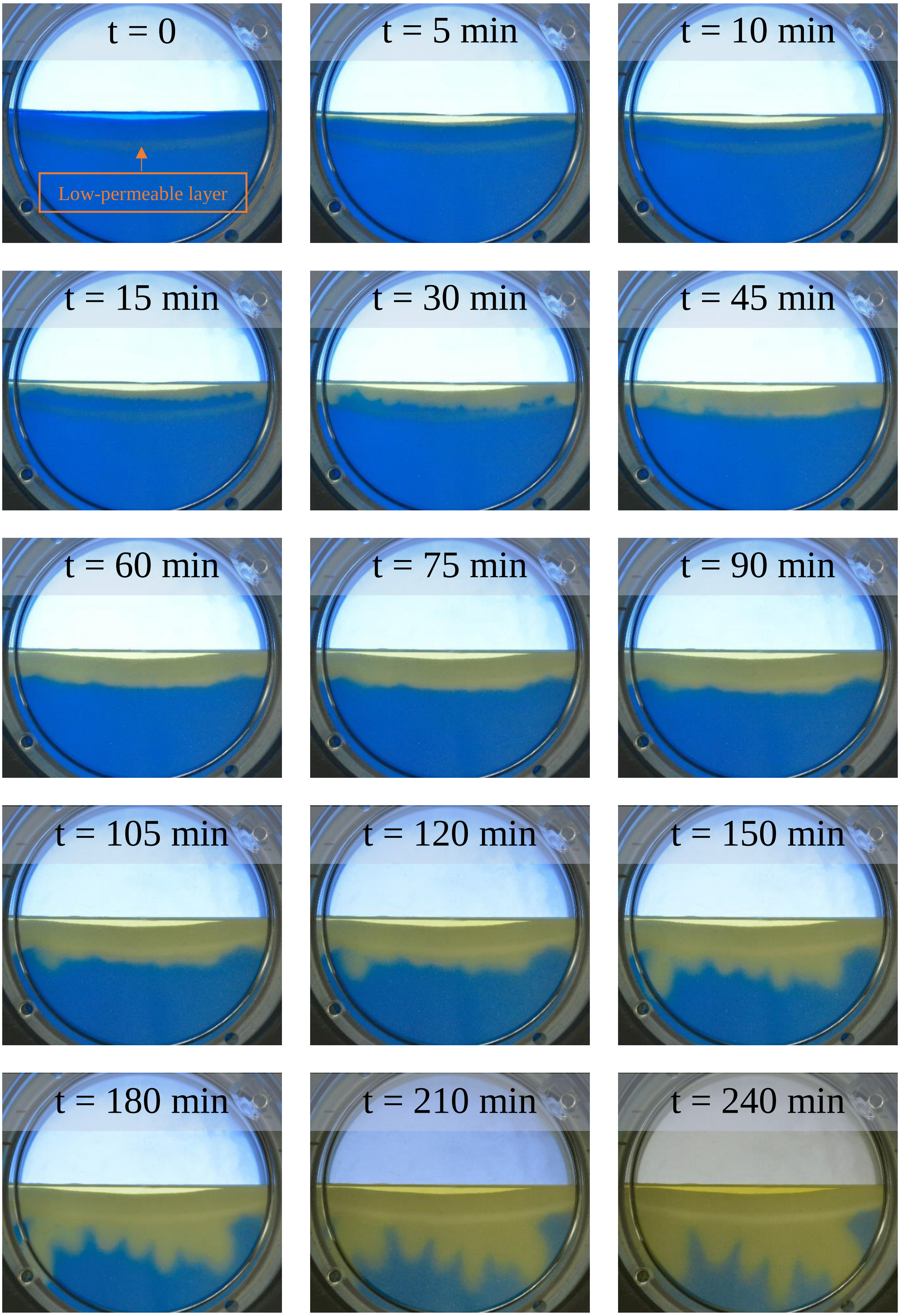

Figure 4.7: An image story showing the course of Experiment 4.3.1 – Set 2, where CO2 dissolved in water-saturated porous media of horizontally alternating permeability of approximately 76 000 mD, 16 000 mD and 76 000 mD.

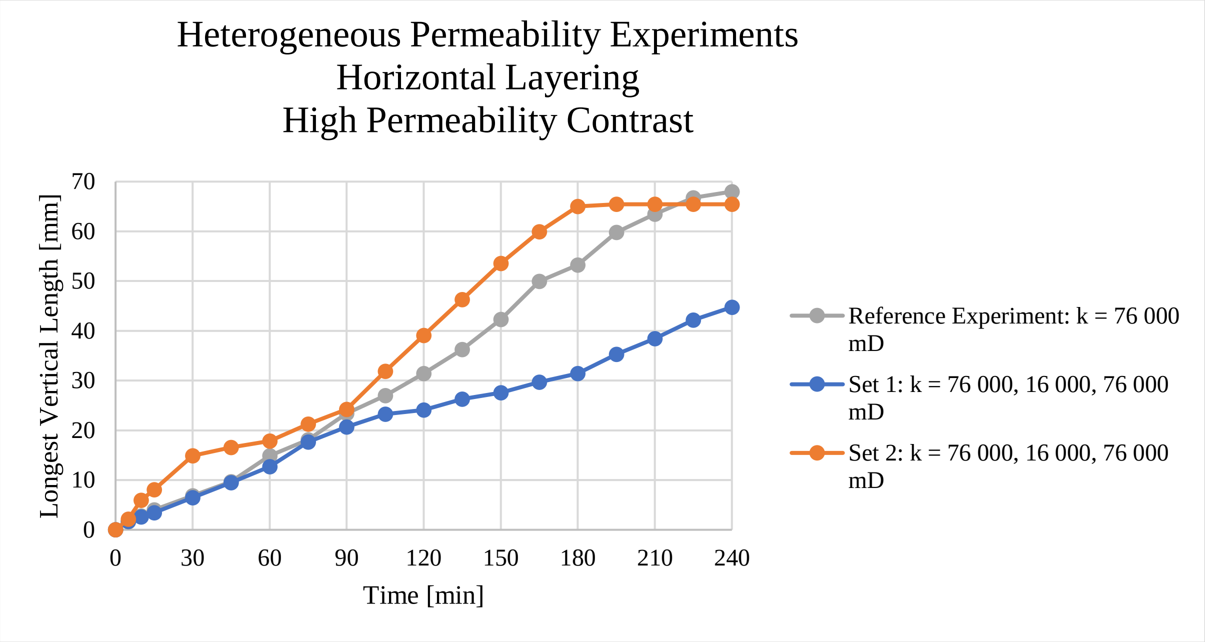

Graph 3: Length of the front of the CO_2*-saturated layer vs. time for the heterogeneous permeability experiments with horizontal layering and a high permeability contrast of 76 000, 16 000, and 76 000 mD. The reference experiment presented in Section 4.2.1 is also included for comparison.*

4.3.2 Porous Media of ≈ 52 000, 16 000 and 52 000 mD Permeability

In the experiments with heterogeneous permeability created by horizontal layering, the cell was mainly filled with a high-permeable porous medium of approximately 52 000 mD (Dark blue in Figure 4.8 and Figure 4.9). A thin layer of a low-permeable porous medium of approximately 16 000 mD (Light blue and marked by an arrow in Figure 4.8 and Figure 4.9), was placed horizontally in between the high-permeable layers.

4.3.2.1 Set 1

When CO_2 was brought in contact with water-saturated porous media a thin CO_2-saturated layer of homogeneous thickness was observed in the top of the porous media 5 minutes into the experiment (See yellow layer in Figure 4.8). Its thickness increased homogeneously as time proceeded to 240 minutes. From the blue curve in Graph 4, this can be observed to agree with the first 15 minutes of the reference experiment of 52 000 mD permeability (Section 4.2.2), in which perturbations from the pure diffusive flow regime developed after 30 minutes. The 52 000 mD reference experiment is represented by a grey curve in Graph 4. At times greater than 15 minutes, the slope of the grey curve in Graph 4 increases steeply compared to the blue curve, substantiating the pure diffusive flow regime in this experiment.

After 300 minutes, the CO_2-saturated started to migrate into the low-permeable layer. As time proceeded from 360 to 420 minutes, the downward flow of the CO_2-saturated layer was attenuated by this low-permeable layer. This can also be observed in Graph 4, in which the slope of the blue curve decreases slightly until 420 minutes into the experiment. This attenuation is in accordance with the results of the reference experiment of 16 000 mD permeability (Section 4.2.3), where no fingers were observed.

The first part of the CO_2-saturated layer had migrated through the low-permeable layer after 420 minutes. The front of this layer was observed to develop an irregular shape and caused the thickness of the CO_2-saturated layer to increase slightly heterogeneously. It is hard to say precisely at what time the perturbations developed into fingers, but finger growth indicates that a density-driven convective flow regime occurred below the low-permeable layer.

Boundary effects from the edge of the cell were observed 300 minutes into the experiment and might have counteracted the downward movement of the CO_2-saturated layer, and thus also the density-driven convection regime that developed below the low-permeable layer.

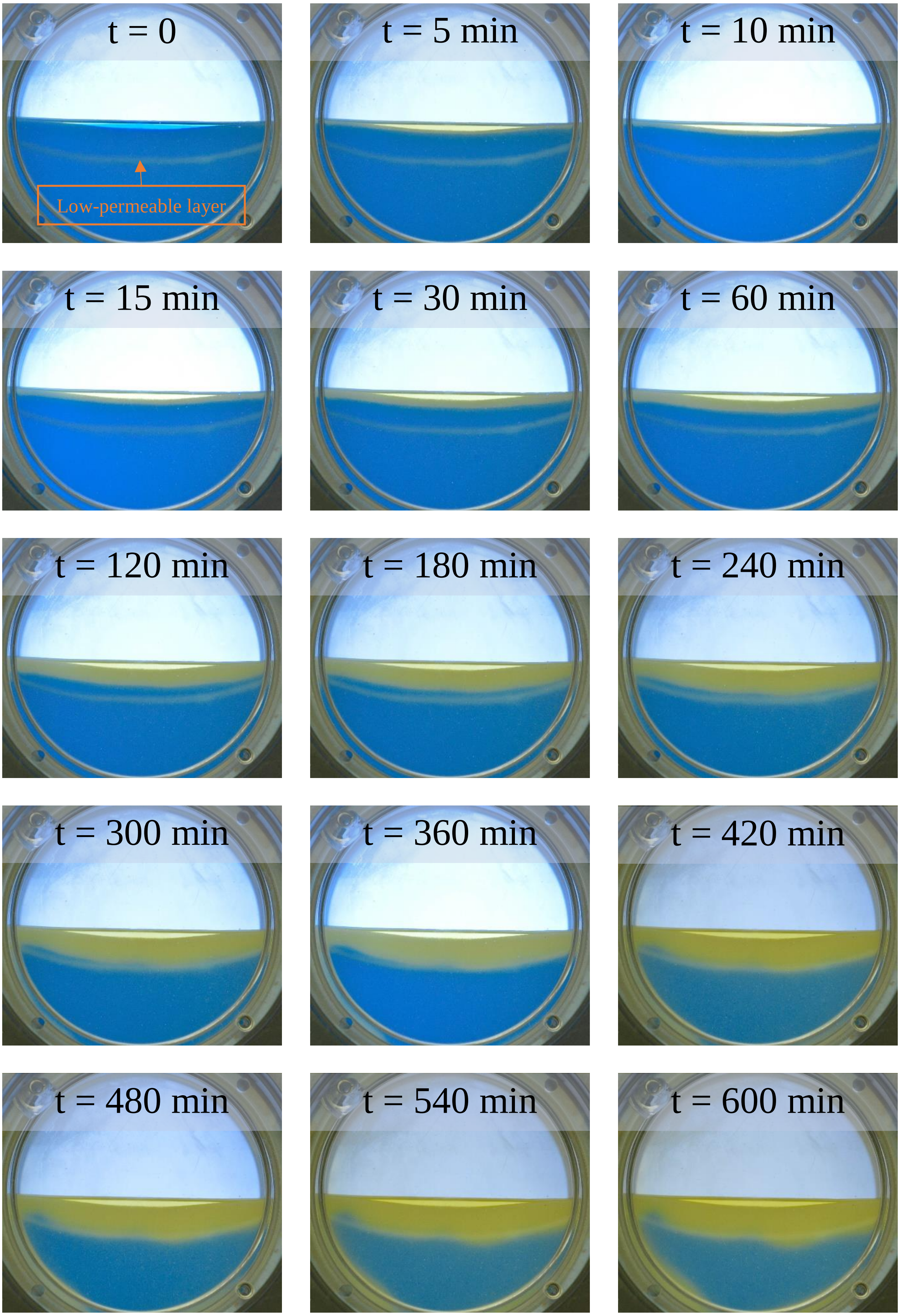

Figure 4.8: An image story showing the course of Experiment 4.3.2 – Set 1, where CO2 dissolved in water-saturated porous media of horizontally alternating permeability of approximately 52 000 mD, 16 000 mD and 52 000 mD.

4.3.2.2 Set 2

When CO_2 was brought above the water-saturated porous media, a thin CO_2-saturated layer of homogeneous thickness was observed after 5 minutes (See yellow layer in Figure 4.9). As time proceeded to 30 minutes, its thickness increased in a homogeneous manner. Based on the homogeneous thickness, molecular diffusion of CO_2 into the water-saturated porous media was assumed to take place. This is in accordance with the relatively low slope of the orange curve in Graph 4 at times smaller 30 minutes, which also coincides with the blue and grey curves, corresponding to Set 1 and the reference experiment of 52 000 mD (Section 4.2.2), respectively. The thickness of the CO_2-saturated layer increased more heterogeneously from 30 to 240 minutes, in the form of one wide finger near the centre of the cell and two narrower fingers at the sides. These fingers are believed to have occurred due to boundary effects from the edge of the cell rather than density-driven convection. This is because the slope of the grey curve in Graph 4, which corresponds to a density-driven convective flow regime at times greater than 45 minutes, increases steeply compared to the orange curve corresponding to the experiment currently being presented. Moreover, the slope of the orange curve, corresponding to Set 1, is lower than that of the blue curve. Overall, this substantiates the interpretation of a pure diffusive flow regime in this experiment, rather than a density-driven convection.

The CO_2 started to dissolve within the low-permeable layer 300 minutes into the experiment. As time proceeded from 360 to 420 minutes, the downwards movement of the CO_2-saturated layer seemed to be attenuated by this low-permeable layer. As for Set 1, this can be observed in Graph 4 in which the slope of the orange curve decreases slightly until 420 minutes. This attenuation is in accordance with the results of the reference experiment of 16 000 mD permeability (Section 4.2.3), where no fingers occurred.

After 480 minutes, CO_2 started to dissolve within the pore space below the low-permeable layer. The front of the CO_2-saturated layer became irregular and caused a heterogeneous increase in the thickness of the layer. It is hard to say precisely at what time the perturbations developed into fingers, but a density-driven convective flow regime is characterized by finger growth, indicating that density-driven convection took place below the low-permeable layer. In Graph 4, the slope of the orange curve can be observed to increase from 420 minutes into the experiment, substantiating this.

Boundary effects from the edge of the cell were observed after 360 minutes, which might have counteracted the downward movement of the CO_2-saturated layer, and thus also the density-driven convective flow regime that developed below the low-permeable layer.

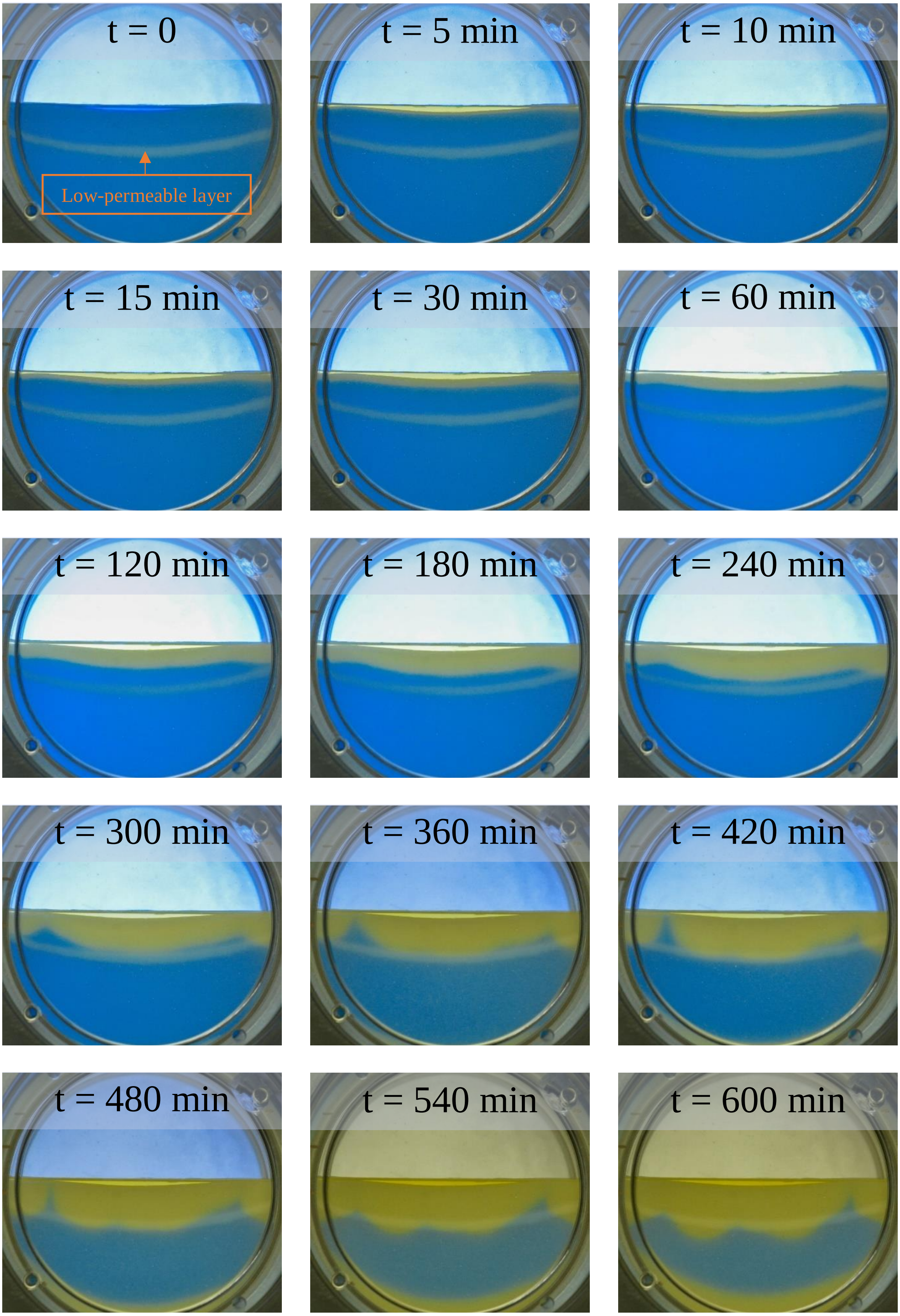

Figure 4.9: An image story showing the course of Experiment 4.3.2 – Set 2, where CO2 dissolved in water-saturated porous media of horizontally alternating permeability of approximately 52 000 mD, 16 000 mD and 52 000 mD.

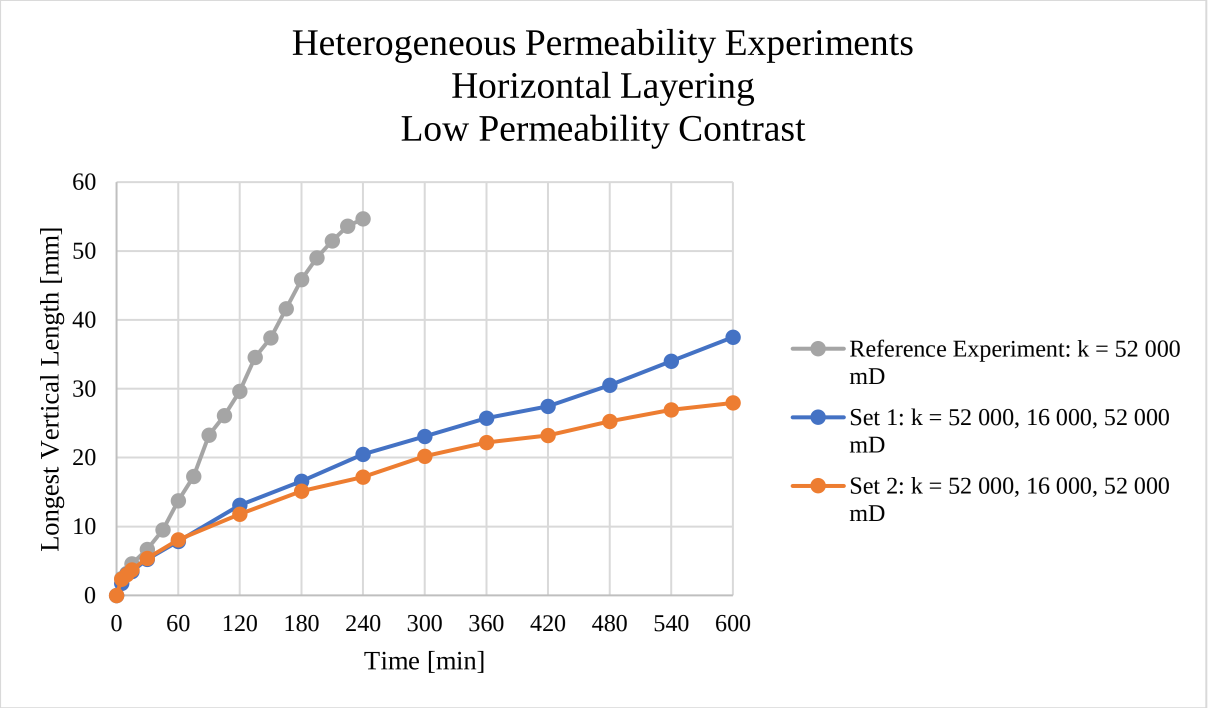

Graph 4: Length of the front of the CO_2-saturated layer vs. time for the heterogeneous permeability experiments with horizontal layering and a low permeability contrast of 52 000, 16 000, and 52 000 mD. The reference experiment presented in Section 4.2.2 is also included for comparison.

4.3.3 Porous Media of ≈ 16 000, 52 000 and 16 000 mD Permeability

In this experiment with heterogeneous permeability created by horizontal layering, the cell was mainly filled with a low-permeable porous medium of approximately 16 000 mD (Light blue in Figure 4.10). Notice that the upper low-permeable layer was very thin (Marked by an arrow in Figure 4.10) A layer of a high-permeable porous medium of approximately 52 000 mD (Dark blue in Figure 4.10), was placed horizontally in between the low-permeable layers.

When CO_2 was injected into the cell and contacted the water-saturated porous media, a thin CO_2-saturated layer of homogeneous thickness was observed in the top of the porous media after 15 minutes (See yellow layer in Figure 4.10). Its thickness increased in a homogeneous manner while CO_2 dissolved in the water within the upper low-permeable layer, approximately until 60 minutes had passed. Based on the homogeneous thickness of the CO_2-saturated layer at times lower 60 minutes, molecular diffusion of CO_2 into the water-saturated porous media was assumed to take place. This interpretation is also in accordance with Graph 5, where the blue and orange curves corresponding to this experiment and the reference experiment of 16 000 mD permeability (Section 4.2.3), respectively, almost coincide at times lower than 60 minutes.

CO_2 started to dissolve in the water within the pore space of the high-permeable layer approximately 60 minutes into the experiment. In contrast to the reference experiment of 52 000 mD permeability (Section 4.2.2), in which density-driven convection clearly occurred, a pure diffusive flow regime dominated this experiment for as long as CO_2 dissolved within the high-permeable layer. A picture was even included at 600 minutes, to clarify that the pure diffusive flow regime remained throughout the experiment. One can even observe in Graph 4, that the CO_2 dissolution slows down when it started to dissolve in the high-permeable layer after 60 minutes, and was faster in the reference experiment of 16 000 mD (Section 4.2.3), than in the high-permeable layer in the experiment currently being presented, between 60 and 210 minutes. After 210 minutes, boundary effects from the edge of the cell dominated the reference experiment of 16 000 mD permeability, while such effects were not visible in the experiment currently being presented. This is probably why the CO_2 dissolution was faster in this experiment than in the 16 000 mD reference experiment at times greater than 210 minutes.

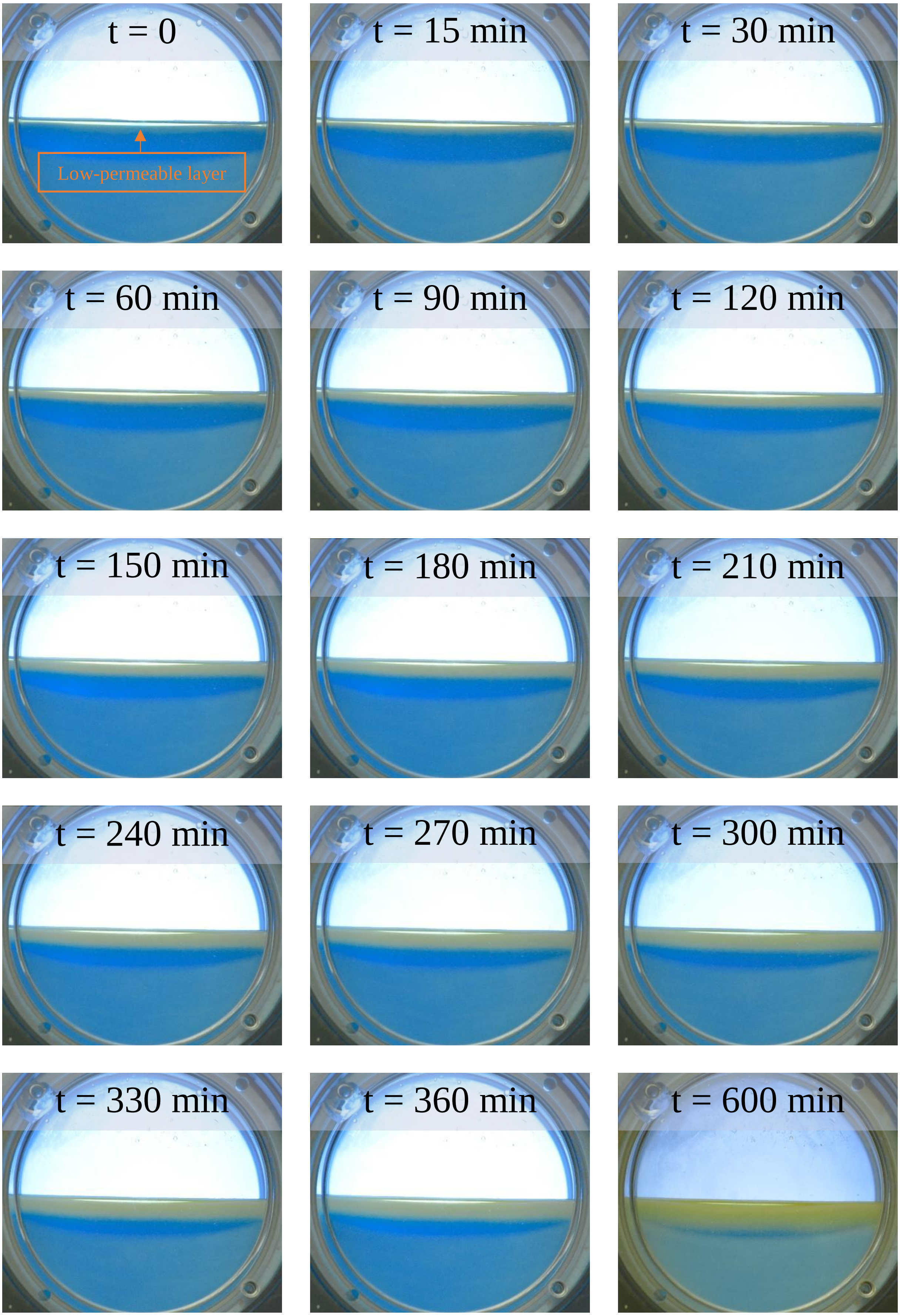

Figure 4.10: An image story showing the course of Experiment 4.3.3, where CO2 dissolved in water-saturated porous media of horizontally alternating permeability of approximately 16 000 mD, 52 000 mD and 16 000 mD.

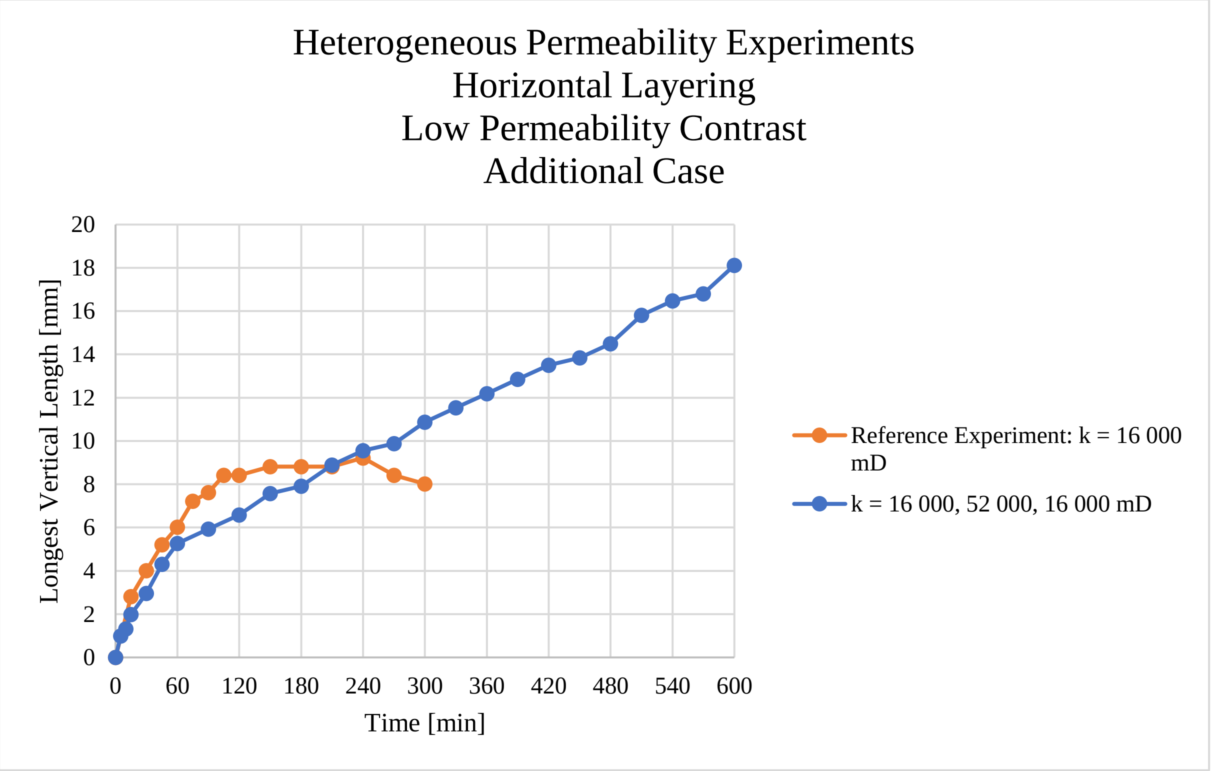

Graph 5: Length of the front of the CO2-saturated layer vs. time for the heterogeneous permeability experiments with horizontal layering and a low permeability contrast of 16 000, 52 000, and 16 000 mD. The reference experiment presented in Section 4.2.3 is also included for comparison.

4.4 Heterogeneous Permeability Experiments – Vertical Layering

4.4.1 Porous Media of ≈ 16 000, 76 000 and 16 000 mD Permeability

In the experiments with heterogeneous permeability created by vertical layering, the cell was mainly filled with a low-permeable porous medium of approximately 16 000 mD permeability (Light blue in Figure 4.11 and Figure 4.12). A layer of a high-permeable porous medium of approximately 76 000 mD permeability (Dark blue in Figure 4.11 and Figure 4.12), was placed vertically in between the low-permeable layers.

4.4.1.1 Set 1

When CO_2 was brought in contact with the water-saturated porous media, a thin CO_2-saturated layer of homogeneous thickness was observed in the top of both types of porous media at after 15 minutes (See yellow layer in Figure 4.11). Based on the homogeneous thickness of the CO_2-saturated layer, molecular diffusion of CO_2 into the water within the pore space of the porous media was assumed to take place. This is in accordance with Graph 6, in which the blue curve has a relatively low slope at these early times.

After approximately 30 minutes, the CO_2-saturated layer appeared slightly thicker in the high-permeable layer in the centre of the cell than in the low-permeable layers surrounding it. This indicated the development of perturbations from the pure diffusive flow regime. As time proceeded from 30 minutes, the thickness of the CO_2-saturated layer became more heterogeneous as it kept increasing in the high-permeable layer in the centre of the cell. It is not easy to say exactly at what time the perturbations developed into density-driven convection, but according to Graph 6, which is based on the thickest part of the CO_2-saturated layer, the slope of the blue curve starts increasing after approximately 45 minutes, indicating the initiation of a density-driven convective flow regime within the high-permeable layer. Only one finger developed. It was quite wide compared to fingers developing in the reference experiment of 76 000 mD permeability (Section 4.2.1). In Graph 6, its growth rate can be observed to be approximately equal to that of the longest finger in the 76 000 mD reference experiment, represented by the grey curve. The finger migrated through the high-permeable layer and reached the bottom of the cell after 240 minutes. During this time, the CO_2 dissolved in a pure diffusive way within the low-permeable layers at the sides. This was in accordance with the 16 000 mD reference experiment (Section 4.2.3), where fingers were not observed. Between 240 and 300 minutes, the CO_2-saturated layer in the centre of the cell was observed to be dominated by a lateral diffusive flow regime, causing the thickness of the CO_2-saturated layer in the centre of the cell to increase homogeneously in the lateral directions.

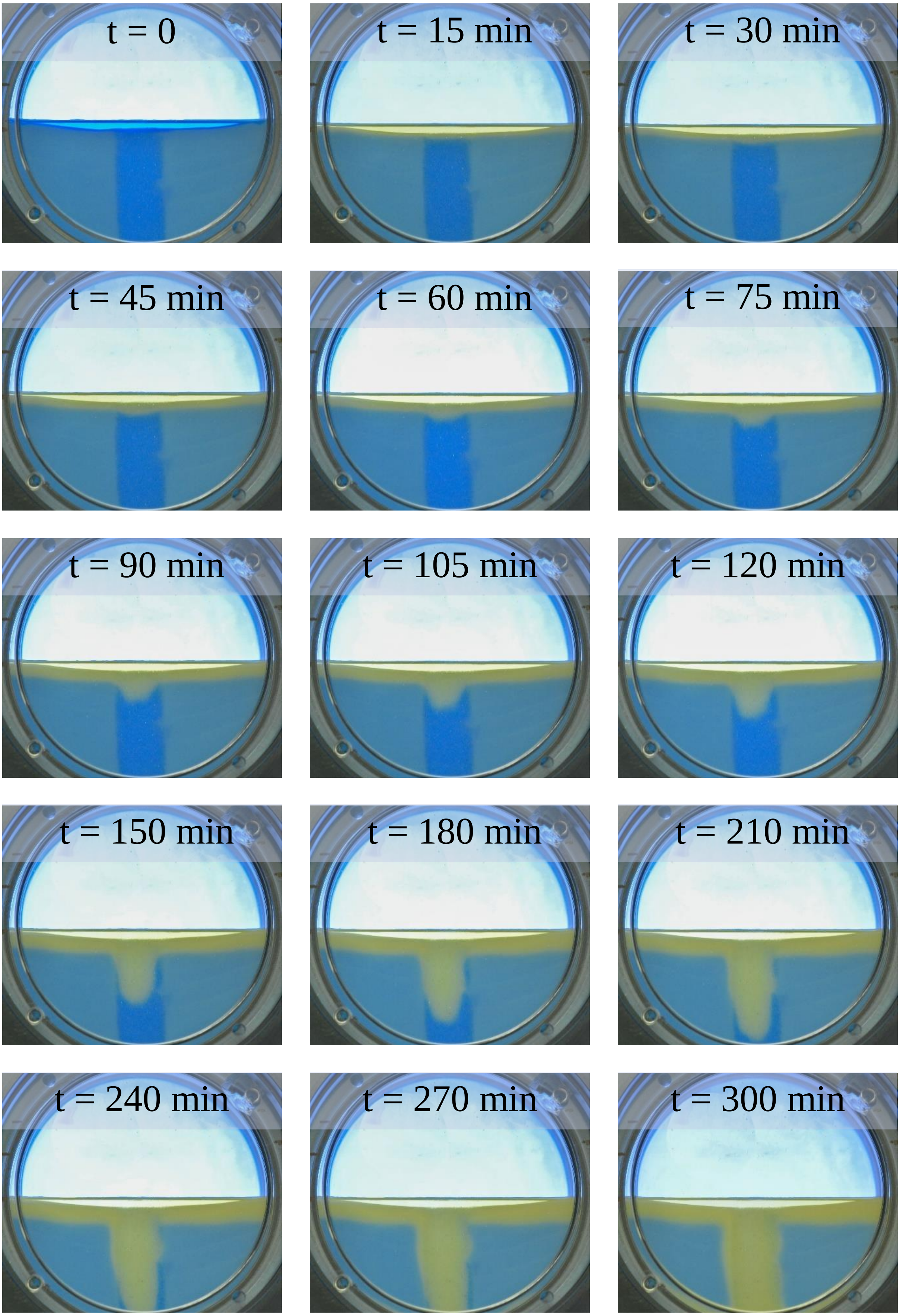

Figure 4.11: An image story showing the course of Experiment 4.4.1 – Set 1, where CO2 dissolved in water-saturated porous media of vertically alternating permeability of approximately 16 000 mD, 76 000 mD and 16 000 mD.

4.4.1.2 Set 2

When CO_2 was brought above the water-saturated porous media, a thin CO_2-saturated layer of homogeneous thickness formed in the top of both types of porous media within 15 minutes (See yellow layer in Figure 4.12). Based on the homogeneous thickness of the CO_2-saturated layer, molecular diffusion of CO_2 into the water within the pore space of the porous media is assumed to have taken place. This is in accordance with Graph 6, where the slope of the orange curve is relatively low at these early times.

After 45 minutes, the CO_2-saturated layer appeared slightly thicker in the vertical high-permeable layer in the centre of the cell, compared to the in the low-permeable layers surrounding it. This is an indication of the development of perturbations from the pure diffusive flow regime. As time proceeded from 45 minutes, the thickness of the CO_2-saturated layer became more heterogeneous as it kept increasing in thickness in the vertical high-permeable layer in the centre of the cell. It is not easy to say precisely at what time the perturbations developed into a density-driven convective flow regime based on Figure 4.12, but the slope of the orange curve in Graph 6 starts increasing after approximately 60 minutes, indicating the initiation of density-driven convection within the high-permeable layer in the centre of the cell.

As for Set 1, only one finger developed. This finger was also quite wide compared to fingers that developed in the reference experiment with porous media of 76 000 mD permeability (Section 4.2.1). In Graph 6, its growth rate can be observed to be approximately equal to that of the longest finger in the 76 000 mD reference experiment, represented by the grey curve. The finger migrated through the high-permeable layer to the bottom of the cell within 210 minutes, indicating that the density-driven convection was slightly stronger for the experiment currently being presented than for the experiment presented in Set 1. During this time, the CO_2 had dissolved in a pure diffusive way within the low-permeable layers at the sides. This was in accordance with the 16 000 mD reference experiment (Section 4.2.3), in which density-driven convection was not observed. From 210 through 300 minutes, the CO_2-saturated layer in the centre of the cell was dominated by a lateral diffusive flow regime, causing the thickness of the CO_2-saturated layer in the centre of the cell to increase homogeneously in the lateral directions.

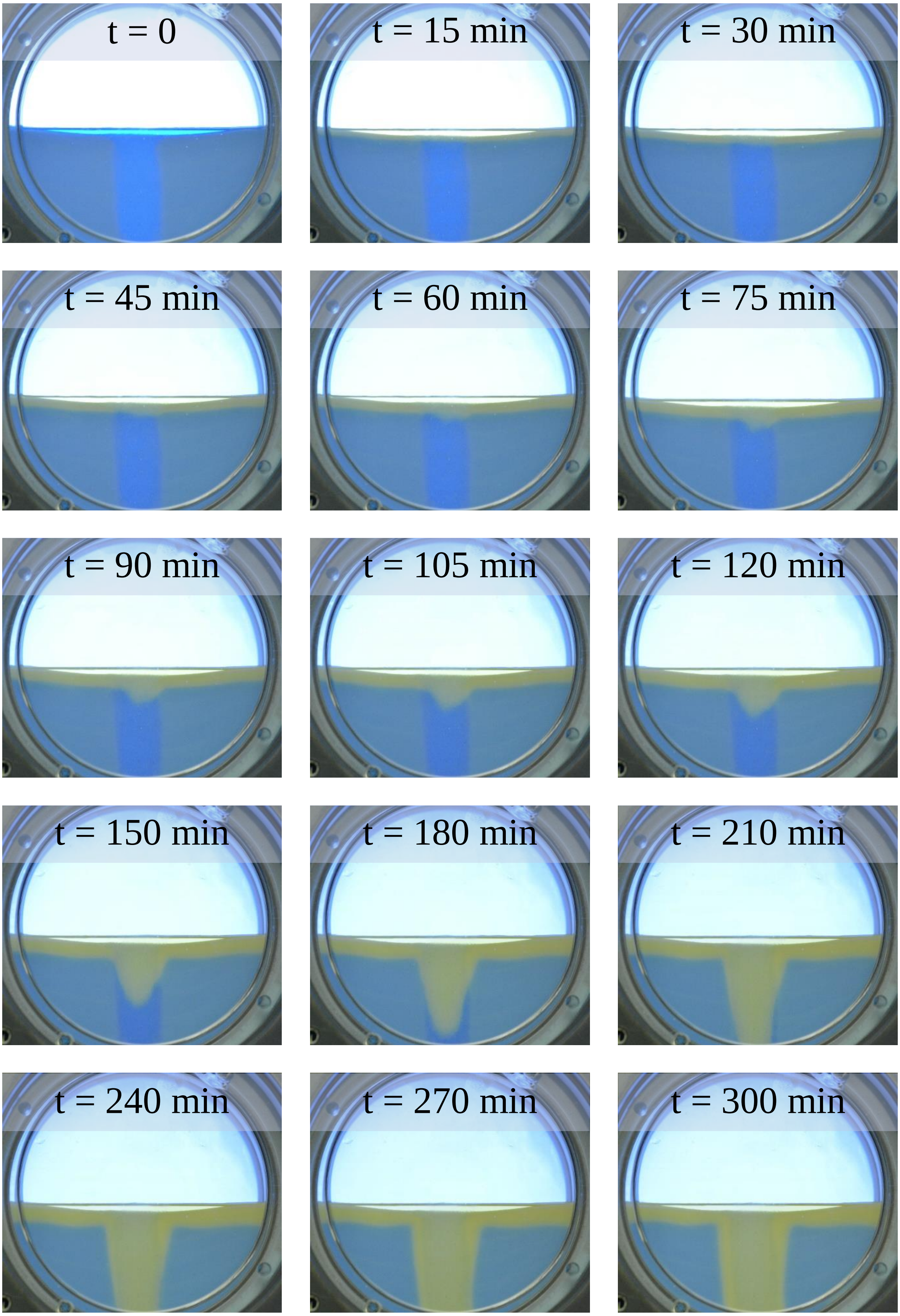

Figure 4.12: An image story showing the course of Experiment 4.4.1 – Set 2, where CO2 dissolved in water-saturated porous media of vertically alternating permeability of approximately 16 000 mD, 76 000 mD and 16 000 mD.

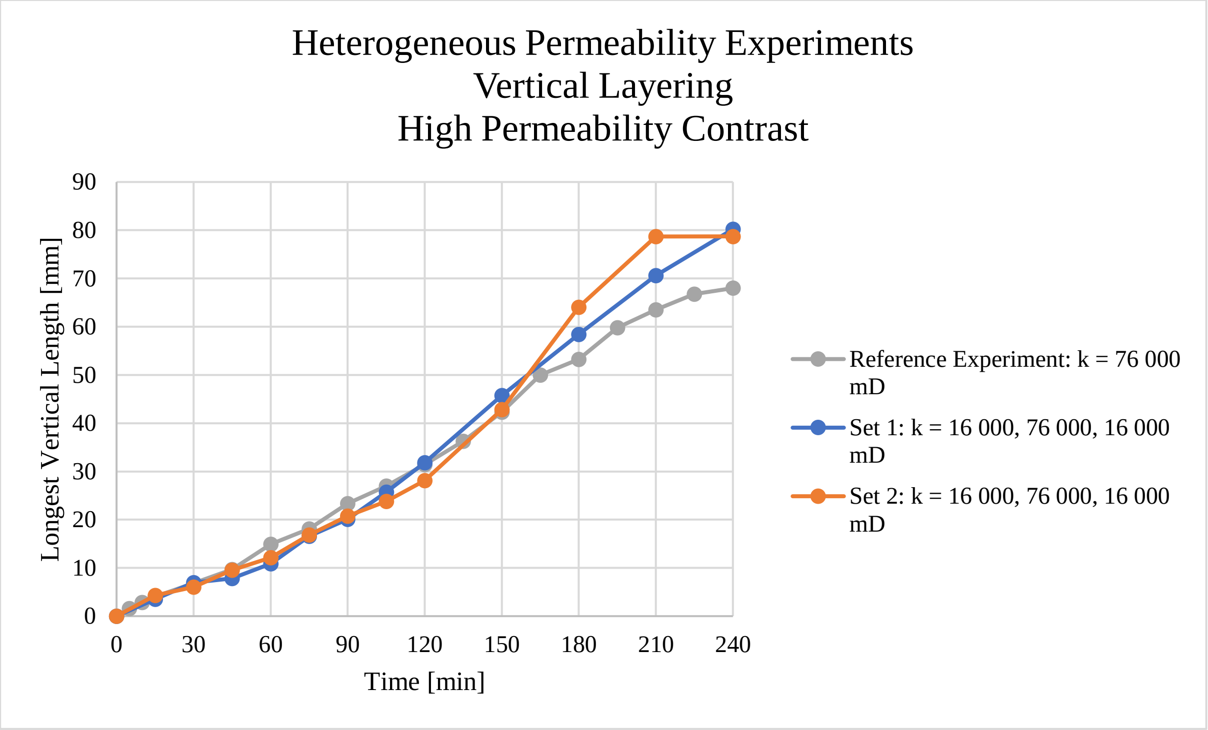

Graph 6: Length of the front of the CO_2-saturated layer vs. time for the vertically alternating permeability experiment with high permeability contrast of 16 000, 76 000, and 16 000 mD. The reference experiment presented in Section 4.2.1 is also included for comparison.

4.4.2 Porous Media of ≈ 16 000, 52 000 and 16 000 mD Permeability

In the experiments with heterogeneous permeability created by vertical layering, the cell was mainly filled with a low-permeable porous medium of approximately 16 000 mD permeability (Light blue in Figure 4.13 and Figure 4.14). A layer of a high-permeable porous medium of approximately 52 000 mD permeability (Dark blue in Figure 4.13 and Figure 4.14), was placed vertically in between the low-permeable layers.

4.4.2.1 Set 1

When CO_2 was injected into the cell and contacted the water-saturated porous media, a thin CO_2-saturated layer of homogeneous thickness formed in the top of both types of porous media after 15 minutes (See yellow layer in Figure 4.13). Molecular diffusion of CO_2 into the water-saturated porous media is assumed to having taken place, based on the homogeneous thickness of the CO_2-saturated layer. This is in accordance with Graph 7, in which the blue curve has a relatively low slope at these early times, which is approximately equal to the slope of the grey curve corresponding to the 52 000 mD reference experiment (Section 4.2.2).

After 30 minutes, the thickness of the CO_2-saturated layer appeared slightly thicker in the high-permeable layer in the centre of the cell than in the low-permeable layers surrounding it. This indicates the development of perturbations from the pure diffusive flow regime. As time proceeded from 30 minutes, the CO_2-saturated layer became more heterogeneous as its thickness kept increasing in the high-permeable layer in the centre of the cell. Based on Figure 4.13, it is hard to say exactly at what time the perturbations developed into a density-driven convective flow regime, and according to Graph 7, this regime did not develop at all, because the slope of the blue curve never starts increasing after the relatively low slope associated with a pure diffusive flow regime. This stands in contrast to the reference experiment of 52 000 mD (Section 2.2) represented by the grey curve in Graph 7, in which the slope starts increasing at approximately 45 minutes, indicating the initiation of a density-driven convective flow regime. During the experiment, the CO_2 dissolved in a pure diffusive way within the low-permeable layers at the sides. This was in accordance with the reference experiment of 16 000 mD permeability (Section 4.2.3), where fingers were not observed.

Boundary effects from the edge of the cell were observed after180 minutes. Consequently, a finger formed and migrated vertically upwards within the high-permeable layer in the centre of the cell. This seemed to counteract the downward movement of the CO_2-saturated layer, as it stagnated instead of accelerating. Thus, in this experiment, the finger did not migrate through the high-permeable layer to reach the bottom of the cell.

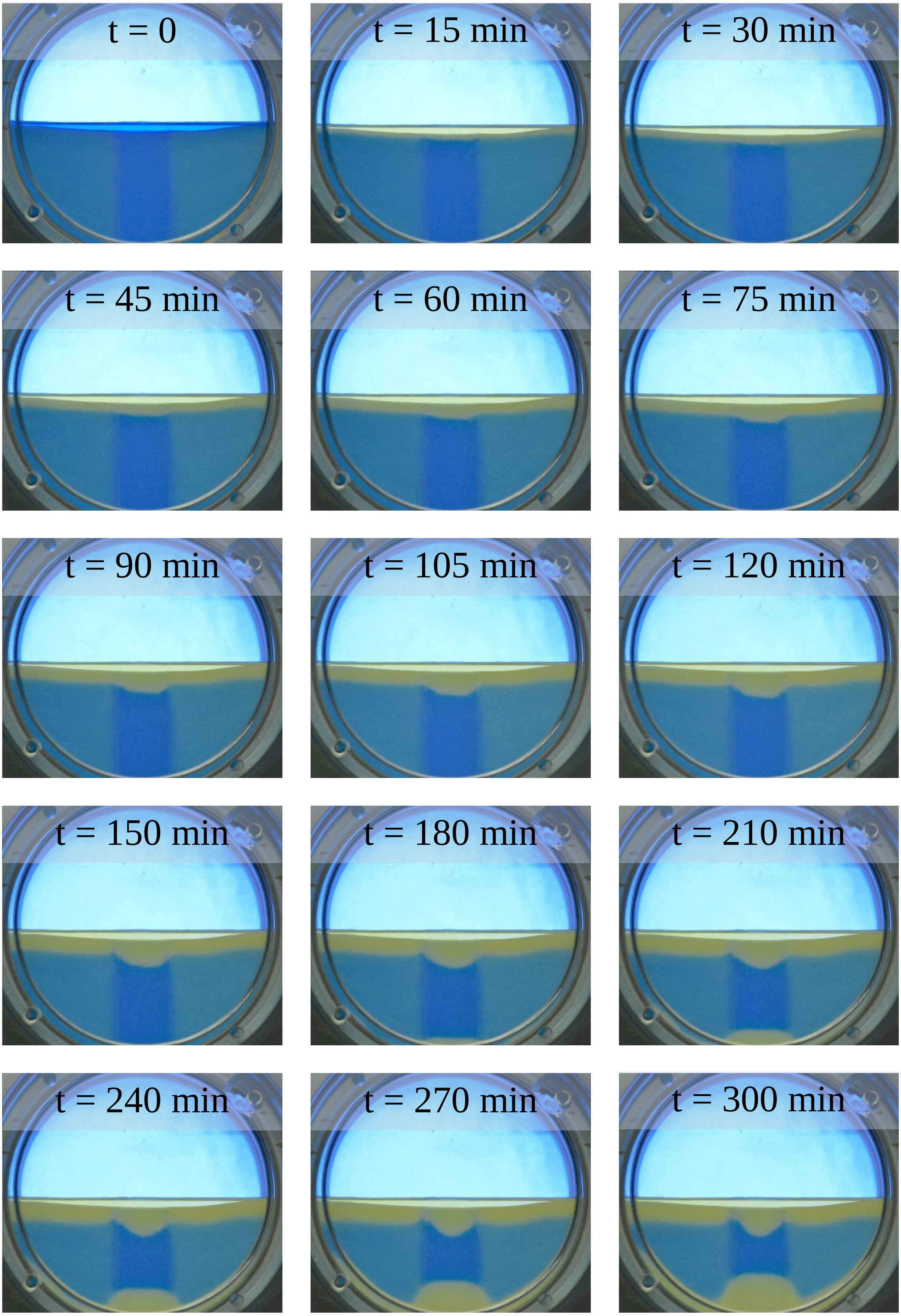

Figure 4.13: An image story showing the course of Experiment 4.4.2 – Set 1, where CO2 dissolved in water-saturated porous media of vertically alternating permeability of approximately 16 000 mD, 52 000 mD and 16 000 mD.

4.4.2.2 Set 2

When CO_2 was brought in contact with the water-saturated porous media, a thin CO_2-saturated layer of homogeneous thickness developed in the top of both types of porous media after 15 minutes (See yellow layer in Figure 4.14). Based on the homogeneous thickness of the CO_2-saturated layer, molecular diffusion of CO_2 into the water-saturated porous media is interpreted to have taken place. This is in accordance with Graph 7, in which the orange curve has a relatively low slope at these early times. Its slope is, in fact, lower than that of the reference experiment of 52 000 mD permeability (Section 4.2.2), represented by the grey curve in Graph 7.

After 90 minutes, the thickness of the CO_2-saturated layer appeared slightly thicker in the vertical high-permeable layer in the centre of the cell, than in the low-permeable layers surrounding it. This indicates the development of perturbations from the pure diffusive flow regime. This late development of perturbations was the main difference between this experiment and the experiment presented in Set 1. As time proceeded from 90 minutes, the thickness of the CO_2-saturated layer became more heterogeneous as it kept increasing in the high-permeable layer in the centre of the cell. It is difficult to say precisely at what time the perturbations developed into density-driven convection based on Figure 4.14, but the slope of the orange curve in Graph 7 starts increasing approximately at 120 minutes, indicating the initiation of density-driven convection within the high-permeable layer in the centre of the cell. The only finger that grew, was wider than the fingers occurring in the 52 000 mD reference experiment (Section 4.2.2). In accordance with the reference experiment of 16 000 mD permeability (Section 4.2.3), the CO_2-saturated layer migrated evenly downwards within the low-permeable layers on each side throughout the experiment.

When density-driven convection eventually initiated after 120 minutes, the slope of the orange curve in Graph 7 is just as steep as the grey curve representing the 52 000 mD reference experiment (Section 4.2.2). However, due to the late initiation of a density-driven convective flow regime compared to the reference experiment, the overall convection during the experiment was modest in comparison.

At 270 minutes, boundary effects from the edge of the cell were observed. These were observed much later in this experiment compared to in Set 1. Consequently, the counteraction occurred later than for the experiment presented in Set 1. However, the boundary effects occurring at times larger than 270 minutes, seemed to counteract the finger and prevent it from migrating through the high-permeable layer to reach the bottom of the cell.

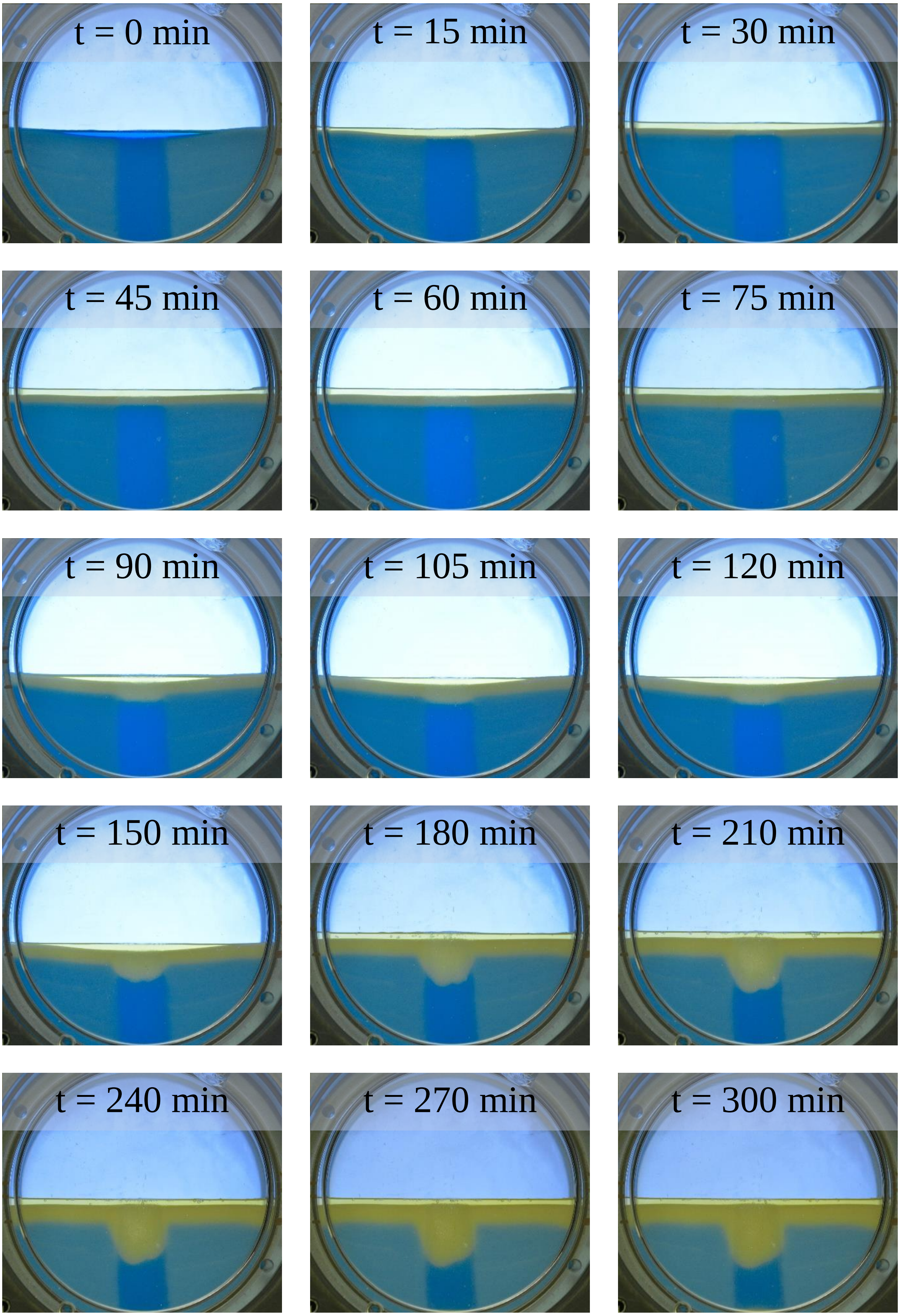

Figure 4.14: An image story showing the course of Experiment 4.4.2 – Set 2, where CO2 dissolved in water-saturated porous media of vertically alternating permeability of approximately 16 000 mD, 52 000 mD and 16 000 mD.

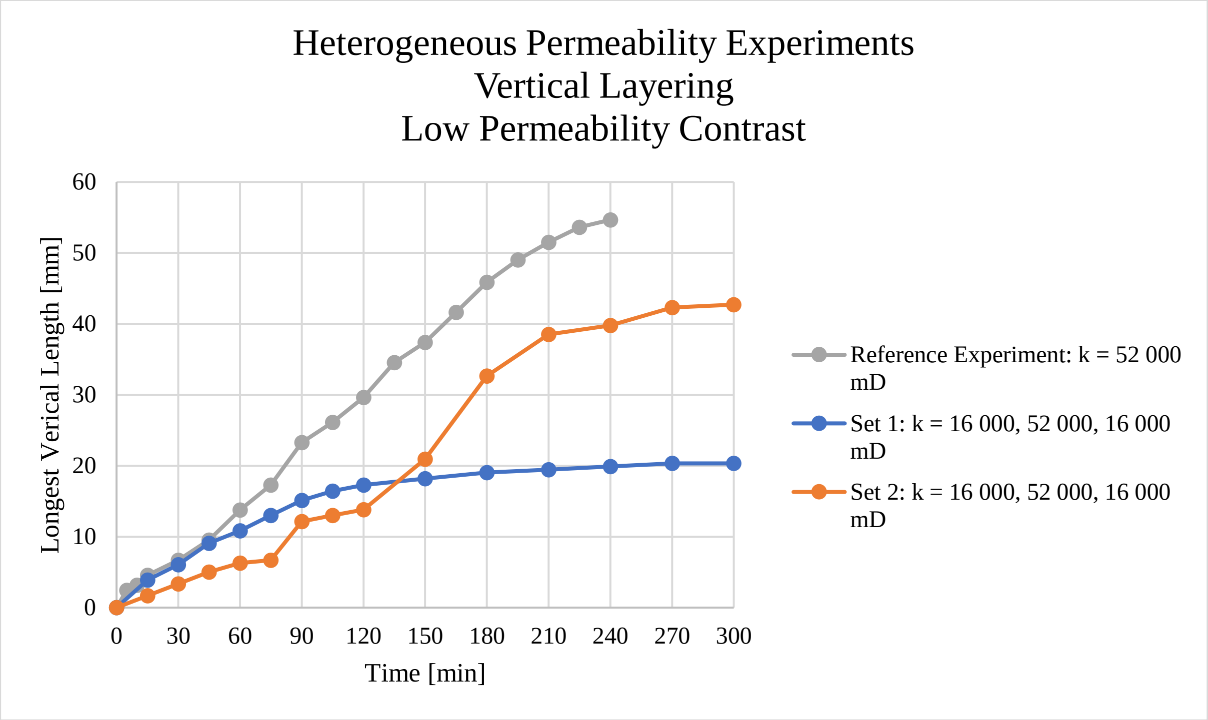

Graph 7: Length of the front of the CO_2-saturated layer vs. time for the vertically alternating permeability experiment with low permeability contrast of 16 000, 52 000, and 16 000 mD. The reference experiment presented in Section 4.2.2 is also included for comparison.

4.4.3 Porous Media of ≈ 52 000, 16 000 and 52 000 mD Permeability

In this experiment with heterogeneous permeability created by vertical layering, the cell was mainly filled with a high-permeable porous medium of approximately 52 000 mD (Dark blue in Figure 4.15). A layer of a low-permeable porous medium of approximately 16 000 mD (Light blue in Figure 4.15), was placed vertically in between the high-permeable layers.

When CO_2 was brought above the water-saturated porous media, a thin CO_2-saturated layer of homogeneous thickness was observed in the top of the porous media after 15 minutes (See yellow layer in Figure 4.15). Based on its homogeneous thickness, molecular diffusion of CO_2 into the water-saturated porous media is interpreted having taken place. This interpretation is in accordance with Graph 8, in which the curve has a relatively low slope at these early times.

Irregularities were observed along the front of the CO_2-saturated layer in the high-permeable layers at the sides of the cell after 30 minutes. At the same time, the front of the CO_2-saturated layer in the low-permeable layer in the centre of the cell looked uniform. The irregularities in the layers at the sides of the cell indicated the development of perturbations from the pure diffusive flow regime. As time proceeded from 30 minutes, the thickness of the CO_2-saturated layer became more heterogeneous in the high-permeable layers at the sides. Based on Figure 4.15, it is not easy to say exactly at what time the perturbations developed into density-driven convection, corresponding to an accelerated CO_2 dissolution. In contrast to the reference experiment of 52 000 mD permeability (Section 4.2.2), in which the slope of the blue curve in Graph 8 starts increasing at 45 minutes to indicate the initiation of a density-driven convective flow regime, the slope of the orange curve does not increase significantly compared to the initial times. Thus, the density-driven convection was stronger in the 52 000 mD reference experiment than in the study currently being presented.

The CO_2 was observed to dissolve diffusively in the low-permeable layer in the centre of the cell throughout the experiment. This is in accordance with the reference experiment of 16 000 mD permeability (Section 4.2.3), where no fingers were observed. However, the fingers in the high-permeable layers at the sides affected this diffusive flow regime within the low-permeable layer, especially at late times.

Boundary effects from the edge of the cell were observed at times greater than 270 minutes. An image was included at 600 minutes to show that a diffusive flow regime developed medially into the low-permeable layer when the fingers merged with the boundary effects from the cell. This is in accordance with the 16 000 mD reference experiment (Section 4.2.3).

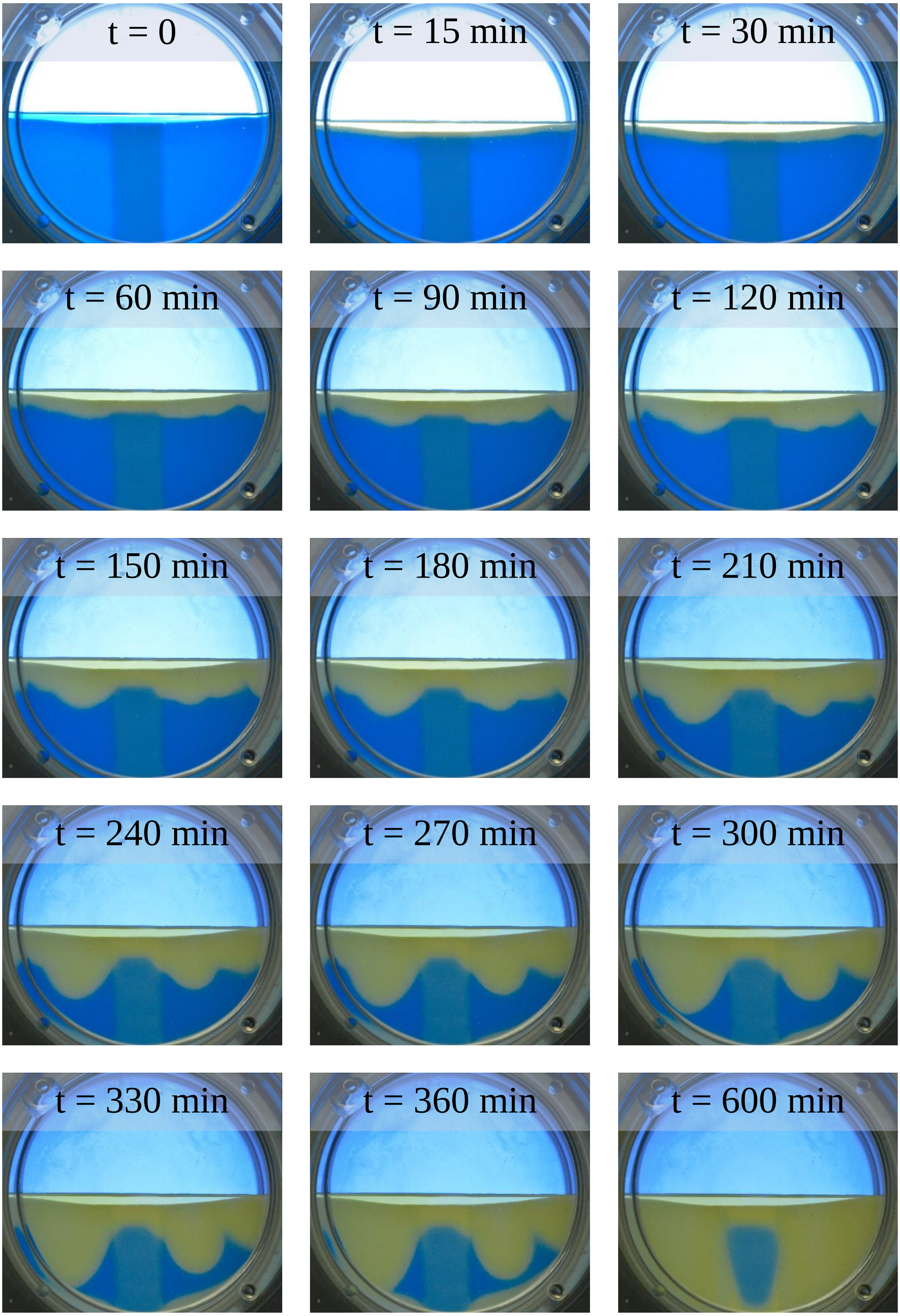

Figure 4.15: An image story showing the course of Experiment 4.4.3, where CO2 dissolved in water-saturated porous media of vertically alternating permeability of approximately 52 000 mD, 16 000 mD and 52 000 mD.

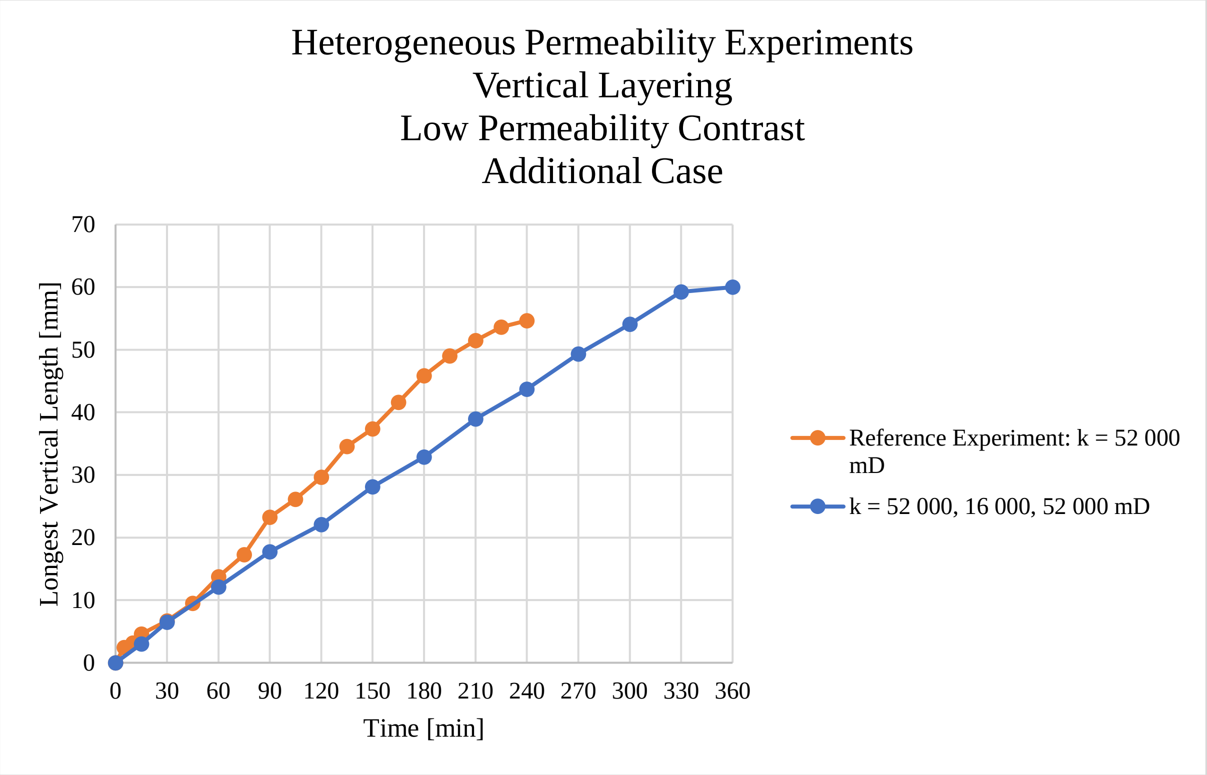

Graph 8: Length of the front of the CO_2-saturated layer vs. time for the additional vertically alternating permeability experiment with low permeability contrast of 52 000, 16 000, and 52 000 mD. The reference experiment presented in Section 4.2.2 is also included for comparison.

5 Discussion

5.1 Discussion of the Experimental Results and Comparison to Previous Work

5.1.1 Bulk Water Experiment

In the bulk water experiment, the CO_2 dissolution was dominated by a pure diffusive flow regime during the first 1.5 minutes, before density-driven convection initiated. This matches the experimental results of Amarasinghe et al. (2018), Faisal et al. (2013, 2015), Kneafsey & Pruess (2010) and Thomas et al. (2015, 2018). Immediate onset of convection without an initial diffusive flow regime was only reported by Khosrokhavar et al. (2014), and the deviations between the results of the latter study and the results of the present study was expected, since the experiments of Khosrokhavar et al. (2014) were performed at higher pressure and with larger spacing between the sight discs. This leads to higher permeability, and consequently a larger Rayleigh number than for the experiment in the present study.

When the density-driven convective flow regime dominated, the finger fronts became wider as the fingers migrated vertically downwards, resulting in finger merging and thus a reduction in the number of fingers. A similar development of the convective pattern was reported by Faisal et al. (2013, 2015), Kneafsey & Pruess (2010) and Thomas et al. (2015). At the last stage of the density-driven convective flow regime, the fingers were affected by cell-scale convection, a behaviour that was also reported by Kneafsey & Pruess (2010).

5.1.2 Homogeneous Permeability Experiments

In the experiments with homogeneous permeabilities, the main difference in results between the different permeabilities was that the front of the CO_2-saturated layer migrated significantly faster in the two high-permeable experiments, with permeabilities of 76 000 mD and 52 000 mD, than in the two low-permeable with permeabilities of 16 000 mD and 4 000 mD. This indicated a higher rate of CO_2 dissolution in the high-permeable experiments, compared to the low-permeable experiments, which can probably be explained by density-driven convection in the two high-permeable experiments, and pure molecular diffusion in the two low-permeable experiments. These observations are in accordance with the results of Amarasinghe et al. (2018), in which density-driven convection was observed in experiments with porous media of 76 000 mD permeability but not in experiments with porous media of 4000 mD permeability. The results are also in accordance with the results of a stability analysis performed by Lindeberg and Wessel-Berg (1997), in which they concluded that density-driven convection typically will initiate in high-permeable aquifers.

In the two high-permeable experiments, a pure diffusive flow regime dominated the CO_2 dissolution during the first 15 minutes. The fronts of the CO_2-saturated layers migrated at approximately the same rates during this period, indicating that the rates of CO_2 dissolution were approximately equal for the two experiments. In both experiments, a density-driven convective flow regime initiated after approximately 45 minutes. When the experiments were dominated by density-driven convection, the front of the CO_2-saturated layer migrated faster for the 76 000 mD experiment than for the 52 000 mD experiment, indicating a higher rate of CO_2 dissolution for the former experiment than for the latter. This was probably due to a higher Rayleigh number for the experiment with the highest permeability. This is in accordance with the results of Farajzadeh et al. (2011), who found the finger fronts to move faster for the larger Rayleigh numbers corresponding to higher permeabilities, in their simulations with homogeneous porous media.

In the two low-permeable experiments, the CO_2 dissolution was dominated by a pure diffusive flow regime throughout the course of the experiments. This indicates that the low permeabilities in these experiments resulted in Rayleigh numbers that were lower than the critical Rayleigh number, Ra_c, which is the lower limit for growth of perturbations and subsequent density-driven convective flow behaviour. The fronts of the CO_2-saturated layers migrated almost as fast as for the two high-permeable porous media during the first 15 minutes, when the two high-permeable experiments were dominated by a diffusive flow regime. This indicates a rate of CO_2 dissolution that was almost similar for all porous media when they were all dominated by a diffusive flow regime. After these 15 minutes, the migration of the fronts of the CO_2-saturated layers gradually started to decline for the two low-permeable experiments. This indicates that pure molecular diffusion is a self-decelerating mechanism, as the water near the CO_2-water interface becomes saturated with CO_2 and unsaturated water does not come close enough to the CO_2 plume for molecular diffusion.

After 150 minutes, the front of the CO_2-saturated layer apparently moved faster for the 4 000 mD experiment than for the 16 000 mD experiment. This is, however, believed to be due to boundary effects from the edge of the cell, which counteracted the downwards migration of CO_2-saturated water in the 16 000 mD permeability system. Boundary effects from the edge of the cell is an experimental artefact and will be discussed in more detail in Section 5.2.2.

5.1.3 Heterogeneous Permeability Experiments

As far as I know, no previous experimental work has been performed on CO_2 dissolution in porous media of alternating permeability. Nevertheless, based on the results of the reference experiments with homogeneous permeabilities presented in Section 4.2, one can intuitively expect how the CO_2 dissolution process will behave within the different layers in the alternating permeability experiments. Moreover, stability analyses concerning permeability anisotropy (Section 2.6.1) and simulations concerning permeability heterogeneity (Section 2.6.2) might serve as a basis for comparison of the experimental results.

5.1.3.1 Horizontal Layering

For the heterogeneous permeability experiments with horizontal layering, the results differed between the experiments with high and low contrast in permeability between the different layers; In the experiments with a high permeability contrast, density-driven convection took place in the upper high-permeable layer of 76 000 mD permeability, as expected based on the results of the reference experiment of 76 000 mD permeability. In the experiments with a low permeability contrast however, the upper high-permeable layer of 52 000 mD permeability was dominated by diffusion. This was not expected based on the results of the reference experiment of 52 000 mD permeability, in which density-driven convection took place.

These deviating results can probably be explained by a higher overall vertical permeability in the experiments with a high permeability contrast, than in the experiments with a low permeability contrast, although the vertical permeability was not measured. In the experiments in the present study, the overall vertical permeability of the experiments with a high permeability contrast was probably sufficiently high for the Rayleigh number to exceed the critical Rayleigh number, Ra_c. In contrast, the overall vertical permeability was probably too low to exceed Ra_c in the experiments with a low permeability contrast. This might explain the convective and diffusive flow regimes in the upper high-permeable layers for the experiments with a high and low permeability contrast, respectively.

Ennis-King & Paterson (2005) and Xu et al. (2006) both concluded in their linear stability analyses concerning permeability anisotropy, that a decrease in the vertical permeability corresponds to an increase in the critical time for instability to begin. The results of Set 1 in the experiments with a high permeability contrast coincide with these conclusions, as the onset of convection initiated approximately 15 minutes later than for the reference experiment of 76 000 mD permeability. The results of Set 2 however, did not coincide with these conclusions, as the onset of convection initiated earlier than for the 76 000 mD reference experiment. It is difficult to give an exact explanation of this discrepancy, but a possible explanation might, for instance, be natural variations in the experimental conditions. Moreover, the results of the experiments with a low permeability contrast also coincide with the conclusions of Ennis-King & Paterson (2005) and Xu et al. (2006), as the onset of convection did not occur until the front of the CO_2-saturated layer had migrated through the low-permeable layer. Thus, the onset of convection occurred significantly later than observed for the reference experiment with a permeability of 52 000 mD.

The low-permeable layer of 16 000 mD permeability in between the high-permeable layers attenuated the migration of the CO_2-saturated interface both in the experiments with a high and low permeability contrast, compared to migration in the absence of a low-permeable layer. This applies if one disregard the results of Set 2 in the experiments with a high permeability contrast, in which the CO_2-saturated layer migrated faster than in the reference experiment of 76 000 mD permeability. Anyway, the effect of attenuation due to the presence of a low-permeable layer was greater for the experiments with a low permeability contrast than for those with a high permeability contrast. This indicates that the rate of CO_2 dissolution decreased more for the experiments with a low permeability contrast than for those with a high permeability contrast. This attenuation is in accordance with the results of linear stability analyses performed by Lindeberg & Wessel-Berg (1997), in which they found the presence of horizontal low-permeable layers to decrease the likelihood of density-driven convection.

Even though the overall vertical permeability seems to be affected by the permeability contrast between the high- and low-permeable layers, it is believed to depend somewhat on the thickness of the low-permeable layer as well; In case of a relatively thin low-permeable layer, which was the case in most of the experiments with horizontal layering in the present study, the fingers that formed in the upper high-permeable layer of 76 000 mD permeability were not completely attenuated when migrating through the low-permeable layer of 16 000 mD permeability. Thus, density-driven convection reinitiated immediately after having migrated through the low-permeable layer. In the hypothetical case of a relatively thick low-permeable layer, the fingers that might form in the upper high-permeable layer is believed to be completely attenuated by the low-permeable layer, thus transforming the flow regime to a pure diffusive one. This can most likely be explained by a decreasing overall vertical permeability with increasing thickness of the low-permeable layer but will need further investigation.

Furthermore, CO_2 dissolution is most likely affected by the thicknesses of the high-permeable layers surrounding the low-permeable layer. In these experiments, the low-permeable layer was placed so that the upper high-permeable layer was roughly 3 times thinner than the lower high-permeable layer. In the experiments with a low permeability contrast, the “thin” upper high-permeable layer was dominated by a diffusive flow regime, while the “thick” lower high-permeable layer was dominated by a convective flow regime, although both layers had an equal permeability of 52 000 mD. Investigating this was not the focus of the present study and should be looked further into.

5.1.3.2 Vertical Layering

For the heterogeneous permeability experiments with vertical layering, the experiments with a high and low permeability contrast showed a similar trend; In all experiments with a high-permeable layer in between two low-permeable layers, one single finger formed within the high-permeable layer in the centre of the cell, while the low-permeable layers at each side were dominated by diffusion. In the additional experiment with a low-permeable layer in between two high-permeable layers, fingers formed in the high-permeable layers at each side, while the low-permeable layer in the centre of the cell was dominated by diffusion. These results were all expected based on their corresponding reference experiments of homogeneous permeabilities. The thickness of the high-permeable layer is thus believed to affect the number of fingers developing but must be investigated further. The results also coincide with the results of simulations performed by Lin et al. (2016), in which relatively high local permeability values just below the CO_2-water interface was found to trigger instabilities in the diffusive layer and influence the number of fingers developing initially. Similarly, Farajzadeh et al. (2011) found through their simulations that finger development correlated strongly with the permeability distribution in cases with a moderate degree of heterogeneity, that is, fingers developed in the high permeability regions.

In the two experiments with a high permeability contrast, the rates of finger growth were very similar to the rate of the reference experiment of 76 000 mD permeability. The finger that developed in the high-permeable layer of 76 000 mD permeability remained within this layer as it migrated downwards. These results also match with results found by Lin et al. (2016), who showed that the finger development was substantially controlled by the permeability below the fingers and along their paths. Even though it was not surprising that the finger migrated within the vertical high-permeable layer, which was in the gravity direction, it is believed that the finger would migrate in a slightly inclined high-permeable layer as well. This should be investigated.

In the experiments with a low permeability contrast, the development of the finger in Set 1 was similar to the of the longest finger in the reference experiment of 52 000 mD permeability initially, while the development of the finger in Set 2 deviated from these results. It is difficult to give an exact explanation of this discrepancy, but a possible explanation might, for instance, be natural variations in the experimental conditions. In both experiments with a low permeability contrast, the finger that developed in the high-permeable layer of 52 000 mD permeability, was counteracted by boundary effects from the edge of the cell after a while.

5.2 Limitations Related to the Experimental Results

5.2.1 Mixing of porous media

Filling porous media into the cell was performed manually after filling water into the cell. In the heterogeneous permeability experiments, filling a porous medium was very easy to interfere with another porous medium. Consequently, one should therefore not assume a sharp interface between different types of porous media in the heterogeneous permeability experiments, but rather a more diffuse transition between the two.

5.2.2 Boundary Effects

The cell has a cylindrical geometry. In some of the experiments performed with porous media in the cell, CO_2-saturated water from near the CO_2-water interface appears to flow faster along the curved edge of the cell than through the water-saturated porous media. Consequently, when CO_2-saturated water from both the left and right sides reaches the bottom of the cell, it is forced to flow upwards through the porous medium (Figure 5.1). This counteracts the downward migration of CO_2-saturated water. It probably occurs because the beads are not packed perfectly along the curved surface formed by the outer shell. The artefact invalidates some of the results at late times but has not been possible to remove, as it would most likely require a different cell geometry.

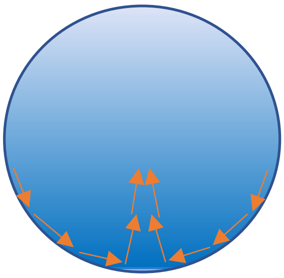

Figure 5.1: Illustration of boundary effects artefacts due to the cell geometry.

5.2.3 pH Indicator Method

As mentioned in Section 2.6.3, Thomas et al. (2015) found that pH indicators should be used with caution in experimental work on CO_2 dissolution because the pattern displayed by a pH indicator only reflects the pH values below the point of which the pH indicator changes colour. Consequently, the pH indicator does not necessarily show the full extent of the pattern developing due to CO_2 dissolution. Moreover, the initial pH of the BTB solution, which is affected by both BTB and NaOH concentration, will also affect the pattern developing due to CO_2 dissolution. This may give rise to inaccurate quantitative characterization of the patterns.

5.2.4 Subjectivity

To collect data used to construct the graphs presented as part of the results in Section 4, the ImageJ software was used for measuring the maximum vertical thickness of the CO_2-saturated layer or the maximum vertical length of the fingers, for chosen images from each experiment. Although this is an accurate tool compared to, for instance, measuring such lengths manually with a ruler, the measurements will be influenced by subjectivity. This is because the vertical lines measured by ImageJ are selected by the user. Consequently, in images where the finger front appears relatively diffuse, the actual vertical length of the finger can appear ambiguous.

5.3 Relevance to Reality

5.3.1 Small-Scale vs. Large-Scale

The short version of the aim presented in the introduction in Section 1.2, is to visualize CO_2 dissolution in porous media on an experimental scale, to improve the understanding of the permeability impact on the CO_2 dissolution process on a reservoir scale. This difference between small and large scales is one of the main constraints of the experimental results; The cell is very small compared to an actual reservoir. Thus, cell-scale convection initiates relatively early due to the short migration distance of the fingers before reaching the cell edge. In contrast, reservoir-scale convection will typically be initiated when the fingers have migrated to the bottom of a reservoir, which can correspond to migration of more than 200 m. Consequently, the long-term evolution of the density-driven convective pattern cannot be followed, as the fingers reach the bottom of the cell earlier than they would reach the bottom of a reservoir. One can, therefore, miss out on important late-stage features of the density-driven convection process that would be relevant for CO_2 storage in reservoirs.

5.3.2 Cell Geometry vs. Reservoir Geometry

The experimental environment of the cell has a cylindrical geometry, which is not a common reservoir geometry. The cell was, however, designed this way because such geometries can withstand higher pressures than other cell geometries. The geometry may have at least two implications for the experimental results: First, the cell-scale convective flow pattern was affected by the cylindrical cell geometry. Fingers migrating vertically downwards from the CO_2-water interface near the sides of the cell migrated for a shorter vertical distance before reaching the edge of the cell, compared to fingers migrating vertically downwards near the

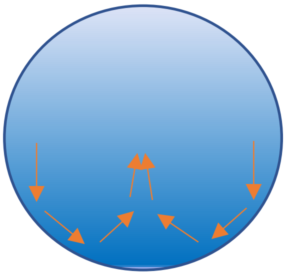

Figure 5.2: Typical cell-scale convective flow pattern due to cylindrical cell geometry.

centre of the cell. Consequently, by assuming that the finger growth is equal throughout the cell, one can expect a convective flow regime where unsaturated water with respect to CO_2 flows upwards in the centre of the cell, rather than at the sides, as shown in Figure 5.2.

Second, in the experiments, the CO_2 dissolved in the 5 mm spacing between two parallel sight disks, which provides a narrow, quasi-2D environment. The word “quasi-2D” is used because the spacing between the sight discs causes some 3D effects. However, neither 2D or quasi-2D effects probably occur in an actual reservoir, which will be fully 3D in its flow nature. Despite this, Lindeberg & Wessel-Berg (2011) stated in their simulation study that “The timing of the onset of convective mixing is independent of whether one considers the problem in 2D or 3D”. They also stated that the rate of convection most likely is slightly more efficient in a 3D than in a 2D environment, as there is more space for convective currents in 3D models. Consequently, by neglecting other differences between the cell and a real reservoir, one might expect the onset of convection to initiate at the same time in the 2D cells and 3D reservoirs. However, 2D cells may not provide a representative convection rate for 3D reservoirs.

5.3.3 Porous Media

The absence of porous media in the bulk water experiment resulted in an unrealistic high and homogeneous permeability, compared to most actual reservoirs. The only exception might be within fractures in the reservoir. Therefore, the bulk water experiment most likely did not provide the most representative conditions for mimicking the CO_2 dissolution process occurring in actual reservoirs. Bulk water experiments can, however, still help increase the basic understanding of CO_2 dissolution in porous media. This is because fluid flow between two parallel plates, as mentioned, is mathematically analogous to Darcy flow in porous media (Faisal et al., 2015; Kneafsey & Pruess, 2010, 2011; Mojtaba et al., 2014).

The presence of porous media in the cell resulted in lower permeabilities than in the bulk water experiment. Porous media were represented by glass beads, ranging in absolute permeabilities from 4 000 to 76 000 mD. The permeabilities were isotropic, while actual reservoirs are typically anisotropic. In underground reservoirs, the permeability is considered extremely good at values between 100 and 1000 mD (Bjørlykke, 2015). Consequently, the permeabilities of the porous media in which density-driven convection occurred (76 000 and 52 000 mD) were generally much higher than permeabilities occurring in most actual reservoirs, with a few exceptions such as Johan Sverdrup. Even the permeabilities of the low-permeable porous media (16 000 and 4 000 mD), where density-driven convection did not occur, were higher than the permeabilities that are considered extremely good in actual reservoirs. Thus, even though lower and more realistic permeabilities were applied for the porous media experiments than for the bulk water experiment, even lower permeabilities can be expected in actual reservoirs. Consequently, even though the Rayleigh numbers were sufficiently high for density-driven convection to occur in these experiments, convection may not occur in real reservoirs if one neglects system variables such as pressure (Section 5.3.4).

In the experiments with heterogeneous permeabilities and horizontal layering, the low-permeable layer in between two high-permeable layers can represent a thin shale layer in between two thicker layers of a reservoir rock. This applies if one considers the permeability contrast between the high- and low-permeable layers instead of permeability values. Thus, these experiments have some relevance to actual reservoirs. Although the ambition was to arrange the porous media layers as horizontal as possible, this was impossible due to the cylindrical geometry of the cell, which acquired the porous media a synclinal structure upon pressurization. This structure is not so relevant to CO_2 storage in reservoirs, which typically have an anticlinal structure to retain buoyant fluids.

In the experiments with heterogeneous permeabilities and vertical layering, the high-permeable layer in between two low-permeable layers can represent a vertical fracture of higher permeability, inside an otherwise low-permeable reservoir. Similarly, the low-permeable layer in between two high-permeable layers can represent an impermeable fault within an otherwise high-permeable reservoir. Consequently, these experiments may be relevant to CO_2 storage in actual reservoirs.

5.3.4 Experimental Conditions

Since the working conditions of the cell are approximately 10 bars pressure and room temperature, these experiments are conducted under non-realistic reservoir conditions. In the experiments, CO_2 consequently occurs in its gaseous phase, while it is usually supercritical at reservoir conditions. CO_2 can dissolve in water both in its gaseous and supercritical state (Hassanzadeh et al., 2009), but the dissolution increases with increasing pressure (Yang & Gu, 2006). Hence, by neglecting other differences, the Rayleigh-number occurring at realistic reservoir conditions will be higher than the Rayleigh numbers applying for these experiments. A high-pressure cell has, however, been designed by Amarasinghe et al. (2018) to perform experiments at supercritical CO_2 conditions.

In a reservoir, the formation water is saline. In the present study, however, distilled water represented the formation water. A small amount of the BTB salt was dissolved in the water for visualization purposes and not for giving the water saline properties. Although it is unrealistic to use distilled water to represent formation water, it was used here instead of saline water to focus on the effect of permeability only on the CO_2 dissolution.

5.4 Future Work

As a continuation of the experimental work performed in the present study, I will suggest performing experiments with porous media of heterogeneous permeability; In experiments with horizontal layering, I would suggest various thicknesses and locations of the low-permeable layer in between high-permeable layers. This is to observe the effect of attenuation as a function of low- and high-permeable layer thicknesses, respectively. In experiments with vertical layering, I would suggest varying the thickness of the high-permeable layer surrounded by low-permeable porous media. This is to observe the number of fingers forming as a function of high-permeable layer thickness. One could also include an inclined high-permeable layer surrounded by low-permeable porous media to observe whether the finger tended to migrate vertically, as expected by gravity, or whether it would rather follow the high-permeable layer and migrate obliquely. The suggestions are organized in Table 3.

As a general point of view, experiments should be performed at temperature and pressure conditions that are more relevant for actual reservoir conditions. Experiments could also include visualization of CO_2 dissolution in oil, which is relevant for CO_2 storage in reservoirs.

Table 3: Suggestions for a continuation of the experimental work performed in the present study.

Type of Experiment	**Description of Experiment**
Heterogeneous Permeabilities – Horizontal Layering	Vary the thickness of the low-permeable layer in between high-permeable layers
	Vary the thickness of the high-permeable layer in between low-permeable-layers
Heterogeneous Permeabilities – Vertical Layering	Vary the thickness of the high-permeable layer in between low-permeable layers
Heterogeneous Permeabilities – Oblique Layering	Oblique high-permeable layer in between low-permeable layers
Reservoir conditions	Higher and more realistic pressure and temperature conditions
Oil	CO_2 dissolution in oil

6 Conclusions

The work of the present study has shown that the pH indicator method can be used for visualization of density-driven convective flow in Hele-Shaw cell experiments conducted at 10 bars pressure and room temperature, with water as well as water-saturated, water-wet, porous media as cell content.

CO_2 diffused into the water at the beginning of all the experiments performed in the present study. The diffusion rate was relatively insensitive to the permeability of the porous medium. Permeability affected the CO_2 dissolution rate at later stages; Density-driven convection took place and accelerated the CO_2 dissolution beyond that of molecular diffusion in the bulk water experiment ($k = 2 \cdot 10^9$ mD), and in the high-permeable porous media ($k = 76\,000$ and $52\,000$ mD) in the experiments with homogenous permeability. The homogeneous low-permeable porous media ($k = 16\,000$ and $4\,000$ mD), stabilized perturbations occurring in the system and diffusion dominated throughout these experiments.

In the experiments with porous media of heterogeneous permeability, a horizontal low-permeable layer in between two high-permeable layers delayed the onset of density-driven convection and attenuated the fingers to some degree. This was most likely due to a decrease in the vertical permeability and a corresponding decrease in the Rayleigh number. The stabilizing effect of the low-permeable layer was greater for the experiments with low contrast in permeability between the different layers than for those with a high permeability contrast.

In the experiments with porous media of heterogeneous permeability, a high-permeable vertical layer triggered instability in the diffusive layer and developed into subsequent density-driven convection. The finger followed the high-permeable layer as it migrated. The low-permeable vertical layers were dominated by molecular diffusion, both as vertical diffusion from the CO_2-water interface above the porous media and as lateral diffusion from the CO_2-saturated high-permeable layer.

To the best of my knowledge, this is the first time that experimental work has investigated CO_2 dissolution in porous media of heterogeneous permeability. I will suggest continuing to perform experiments with porous media of heterogeneous permeability conditions.

7 References

Amarasinghe, W.S., Fjelde, I., Rydland, J, Chauhan, J.S. & Guo, Y. (2018). *Design and testing of experimental set-up for investigation of convection during CO_2-transport in porous media.* Unpublished Paper presented at the 14th International Conference on Greenhouse Gas Control Technologies (GHGT-14), Melbourne, Australia.

Amarasinghe, W.S., Fjelde, I., Rydland, J. & Guo, Y. (2019). *Effects of Permeability and Wettability on CO_2 Dissolution and Convection at Realistic Saline Reservoir Conditions: A Visualization Study.* Unpublished Paper presented at SPE Europec 2019 featured at 81st EAGE Conference and Exhibition, London, England, UK.

Bjørlykke, K. (Ed.). (2015). *Petroleum Geoscience: From Sedimentary Environments to Rock Physics.* Berlin, Heidelberg: Springer Berlin Heidelberg.

Emami-Meybodi, H., Hassanzadeh, H., Green, C.P. & Ennis-King, J. (2015). Convective dissolution of CO_2 in saline aquifers: Progress in modeling and experiments. *International Journal of Greenhouse Gas Control, 40*(2015). 238-266. doi: https://doi.org/10.1016/j.ijggc.2015.04.003

Ennis-King, J. & Paterson. L. (2005). Role of Convective Mixing in the Long-Term Storage of Carbon Dioxide in Deep Saline Formations. *Society of Petroleum Engineers, 10*(3), 349-356. doi: https://doi.org/10.2118/84344-PA

Faisal, T.F., Chevalier, S. & Sassi, M. (2013). Experimental and Numerical Studies of Density Driven Natural Convection in Saturated Porous Media with Application to CO_2 Geological Storage. *Energy Procedia, 37*(2013). 5323-5330. doi: https://doi-org /10.1016/j.egypro.2013.06.450

Faisal, T.F., Chevalier, S., Bernabe, Y., Juanes, R. & Sassi, M. (2015). Quantitative & qualitative study of density driven CO_2 mass transfer in a vertical Hele-Shaw cell. *International Journal of Heat and Mass Transfer, 81*(2015). 901-914. doi: https://doi-org /10.1016/j.ijheatmasstransfer.2014.11.017

Farajzadeh, R., Barati, A., Delil, H.A., Bruining, J. & Zitha, P.L.J. (2007). Mass Transfer of CO_2 Into Water and Surfactant Solutions. *Petroleum Science and Technology, 25*(12). 1493-1511. doi: https://doi-org /10.1080/10916460701429498

Farajzadeh, R., Zitha, P.L.J. & Bruining J. (2009). Enhanced Mass Transfer of CO_2 into Water: Experiment and Modeling. *Industrial & Engineering Chemistry Research, 48*(13). 6423-6431. doi: http://dx.doi.org/10.1021/ie801521u

Farajzadeh, R., Ranganathan, P., Zitha, P.L.J. & Bruining J. (2011). The effect of heterogeneity on the character of density-driven natural convection of CO_2 overlying a brine layer. *Advances in Water Resources, 34*(3), 327-339. doi: https://doi-org /10.1016/j.advwatres.2010.12.012

Fossen, H. (2008). *Geologi: Stein, mineraler, fossiler og olje* (1st ed.). Bergen: Fagbokforlaget Vigmostad & Bjørke AS

Garcia, J. E. (2001). *Density of Aqueous Solutions of CO_2.* (LBNL-49023). Retrieved from: https://escholarship.org/uc/item/6dn022hb

Green, C., Ennis-King, J. & Pruess K. (2009). Effect of Vertical Heterogeneity on Long-Term Migration of CO_2 in Saline Formations. *Energy Procedia, 1*(1). 1823-1830. doi: https://doi-org /10.1016/j.egypro.2009.01.238

Hassanzadeh, H., Pooladi-Darvish, M. & Keith, D.W. (2006). Stability of a fluid in a horizontal saturated porous layer: Effect of non-linear concentration profile, initial, and boundary conditions. *Transport in Porous Media, 65*(2), 193-211. doi: https://doi.org/10.1007/s11242-005-6088-1

Hassanzadeh, H., Pooladi-Darvish, M. & Keith, D.W. (2009). Accelerating CO_2 Dissolution in Saline Aquifers for Geological Storage - Mechanistic and Sensitivity Studies. *Energy Fuels, 23*(6). 3328-3336. doi: https://doi.org/10.1021/ef900125m

Hesse, M.A., Orr Jr., F.M. & Tchelepi, H.A. (2009). Gravity currents with residual trapping. *Energy Procedia, 1*(1). 3275-3281. doi: https://doi.org/10.1016/j.egypro.2009.02.113

Jensen, J.L. & Lake, L.W. (1988). The Influence of Sample Size and Permeability Distribution on Heterogeneity Measures. *Society of Petroleum Engineers, 3*(2). 629-637. doi: https://doi.org/10.2118/15434-PA

Johnsen, K., Holt, H., Helle, K. & Sollie, O.K. (2009). *Mapping of potential HSE issues related to large-scale capture, transport and storage of CO_2.* (2008-1993). Retrieved from: https://evalueringsportalen.no/evaluering/mapping-of-potential-hse-issues-related-to-large-scale-capture-transport-and-storage-of-co2

Jørstad, A., (2012). *Johan Sverdrup – Offshore Norway: The Story behind the Giant Sverdrup Discovery*. (20177). Retrieved from: http://www.searchanddiscovery.com/documents/2012/20177jorstad/ndx_jorstad.pdf

Karimaie, H. & Lindeberg, E. (2017). Experimental Verification of CO_2 Dissolution Rate Due to Diffusion Induced Convection. *Energy Procedia 114*(2017). 4917-4925. doi: https://doi-org /10.1016/j.egypro.2017.03.1633

Khosrokhavar. R., Elsinga, G., Mojaddam, A., Farajzadeh, R., & Bruining, J. (2011). *Visualization of Natural Convection Flow of Super Critical CO_2 in Water by Applying Schlieren Method*. Paper presented at the SPE EUROPEC/EAGE Annual Conference and Exhibition 23-26 May, Vienna, Austria. doi: https://doi.org/10.2118/143264-MS

Khosrokhavar, R., Elsinga, G., Farajzadeh, R. & Bruining, H. (2014). Visualization and investigation of natural convection flow of CO_2 in aqueous and oleic systems. *Journal of Petroleum Science and Engineering*, *122*(2014), 230-239. doi: https://doi.org/10.1016/j.petrol.2014.07.016

Kneafsey, T.J. & Pruess, K. (2010). Laboratory Flow Experiments for Visualizing Carbon Dioxide-Induced, Density-Driven Brine Convection. *Transport in Porous Media, 82*(1), 123-139. doi: https://doi.org/10.1007/s11242-009-9482-2

Kneafsey, T.J. & Pruess, K. (2011). Laboratory experiments and numerical simulation studies of convectively enhanced carbon dioxide dissolution. *Energy Procedia, 4*(2011), 5114-5121. doi: https://doi.org/10.1016/j.egypro.2011.02.487

Kongsjorden, H., Kårstad, O. & Torp, T.A. (1998). Saline Aquifer Storage of Carbon Dioxide in the Sleipner Project. *Waste Management*, *17*(5-6), 303-308. doi: https://doi.org/10.1016/S0956-053X(97)10037-X

Leonenko, Y. & Keith, D.W. (2008). Reservoir Engineering to Accelerate the Dissolution of CO_2 Stored in Aquifers. *Environmental science & technology, 42*(8), 2742-2747. doi: https://doi.org/10.1021/es071578c

Lin, C.P., Ni, C.F., Lee, I.H. & Li, W.C. (2016). Effects of Permeability Variations on CO_2 Convection in Anisotropic and Heterogeneous Saline Formations. *Terrestrial, Atmospheric and Oceanic Sciences, 27*(1), 121-137. doi: http://dx.doi.org/10.3319/TAO.2015.08.31.01(Hy)

Lindeberg, E. & Wessel-Berg, D. (1997). Vertical convection in an aquifer column under a gas cap of CO_2. *Energy Conversion and Management, 38*(supplement) 229-234. doi: https://doi.org/10.1016/S0196-8904(96)00274-9

Lindeberg, E. & Wessel-Berg, D. (2011). Upscaling studies of diffusion induced convection in homogeneous and heterogeneous aquifers. *Energy Procedia, 4*(2011), 3927-3934. doi: https://doi.org/10.1016/j.egypro.2011.02.331

Metz, B., (Ed.). (2005). *IPCC Special Report on Carbon Dioxide Capture and Storage.* Cambridge: Cambridge University Press.

Mojtaba, S., Behzad, R., Rasoul, N.M. & Mohammad, R. (2014). Experimental study of density-driven convection effects on CO_2 dissolution rate in formation water for geological storage. *Journal of Natural Gas Science and Engineering, 21*(2014), 600-607. doi: https://doi.org/10.1016/j.jngse.2014.09.020

Newell, D.L., Carey, J.W., Backhaus, S.N. & Lichtner, P. (2018). Experimental Study of Gravitational Mixing of Supercritical CO_2. *International Journal of Greenhouse Gas Control, 71*(2018). 62-73. doi: https://doi.org/10.1016/j.ijggc.2018.02.013

Pau, G.S.H., Bell, J.B., Pruess, K., Almgren, A.S., Lijewski, M.J. & Zhang, K. (2010). High-resolution simulation and characterization of density-driven flow in CO_2 storage in saline aquifers. *Advances in Water Resources, 33*(4). 443-455. doi: https://doi.org/10.1016/j.advwatres.2010.01.009

Absolute Permeability. Schlumberger. (n. d., a). Downloaded 05.02.2019. Retrieved from: https://www.glossary.oilfield.slb.com/Terms/a/absolute_permeability.aspx

Anisotropic Formation. Schlumberger. (n. d., b). Downloaded 13.02.2019. Retrieved from: https://www.glossary.oilfield.slb.com/Terms/a/anisotropic_formation.aspx

Directional Permeability. Schlumberger. (n. d., c). Downloaded 13.02.2019. Retrieved from: https://www.glossary.oilfield.slb.com/Terms/d/directional_permeability.aspx

Fingering. Schlumberger. (n. d., d). Downloaded 20.02.2019. Retrieved from: https://www.glossary.oilfield.slb.com/Terms/f/fingering.aspx

Singh, U. (2013). Carbon capture and storage: An effective way to mitigate global warming. *Current Science*, *105*(7), 914-922. Retrieved from: https://www.jstor.org/stable/24098511

Syed, R., Sobh, N., Ravaioli, U., Popescu, G. & Mohamed. M. (2015). ImageJ. *nanoHUB*. doi: https://doi.org /10.4231/D33B5W766

Thomas, C., Dehaeck, S. & De Wit, A. (2018). Convective dissolution of CO_2 in water and salt solutions. *International Journal of Greenhouse Gas Control, 72*(2018), 105-116. doi: https://doi.org /10.1016/j.ijggc.2018.01.019

Thomas, C., Lemaigre, L., Zalts, A., D'Onofrio, A. & De Wit, A. (2015). Experimental study of CO_2 convective dissolution: The effect of color indicators. *International Journal of Greenhouse Gas Control*, *45*(2015), 525-533. doi: https://doi.org/10.1016/j.ijggc.2015.09.002

van Bergen, F., Gale, J., Damen, K.J. & Wildenborg, A.F.B. (2004). Worldwide selection of early opportunities for CO_2-enhanced oil recovery and CO_2-enhanced coal bed methane production. *Energy, 29*(9-10), 1611-1621. doi: https://doi.org/10.1016/j.energy.2004.03.063

Weir, G.J., White, S.P. & Kissling, W.M. (1995). Reservoir Storage and Containment of Greenhouse Gases. *Energy Conversion and Management, 36*(6-9), 531-534. doi: https://doi.org/10.1016/0196-8904(95)00060-Q

Weir, G.J, White, S.P. & Kissling, W.M. (1996). Reservoir Storage and Containment of Greenhouse Gases. *Transport in Porous Media*, *23*(1), 37-60. doi: https://doi.org/10.1007/BF00145265

Xu, X., Chen, S. & Zhang, D. (2006). Convective stability analysis of the long-term storage of carbon dioxide in deep saline aquifers. *Advances in Water Resources, 29*(3), 397-407. doi: https://doi.org /10.1016/j.advwatres.2005.05.008

Yang, C. & Gu, Y. (2006). Accelerated Mass Transfer of CO_2 in Reservoir Brine Due to Density-Driven Natural Convection at High Pressures and Elevated Temperatures. *Industrial & Engineering Chemistry Research, 45*(8), 2430-2436. doi: https://doi.org/10.1021/ie050497r

Zolotukhin, A.B. & Ursin, J.R. (2000). *Introduction to petroleum reservoir engineering.* Kristiansand: Norwegian Academic Press.